Arch. Comput. Meth. Engng.
Vol. **12, 3,** 235-302 (2005)

Archives of Computational Methods in Engineering
State of the art reviews

The Application of the hp–Finite Element Method to Electromagnetic Problems

P.D. Ledger
Seminar for Applied Mathematics
ETH Zentrum
8052 Zürich, Switzerland
ledger@sam.math.ethz.ch

K. Morgan
Civil and Computational Engineering Centre
University of Wales, Swansea
Swansea SA2 8PP, Wales, UK

1 INTRODUCTION

In this paper, we consider the application of finite element methods to the solution of problems in electromagnetics. The emphasis will be placed on techniques which can be readily applied in the solution of a range of practical engineering based problems, but the applications will focus on two key areas where we have previous experience, viz electromagnetic scattering and eigenvalue computation. We will draw on an extensive literature, from both the mathematical and engineering disciplines, so it is hoped that mathematicians and engineers will find this review to be both interesting and informative.

The bulk of this article will be devoted to the subject of the approximation of Maxwell's equations by edge elements. These elements appear in the literature under a variety of different names, including vector elements and covariant projection elements, while within the mathematical community they are often referred to as $\boldsymbol{H}(\mathrm{curl})$ conforming elements. In what follows, we will mainly employ the latter term, as the edge element designation is only appropriate when talking about the lowest order case, in which each degree of freedom is associated with an element edge. For higher order elements, degrees of freedom can also be associated with the element interiors and, in three–dimensions, with the element faces so that, in this case, the edge element terminology seems inappropriate.

The mathematical and engineering literature provides extensive coverage of the use of the finite element method in electromagnetics and there are a number of text books that provide an introduction to the topic. An engineering perspective may be obtained from the text by Jin [70], which provides an introductory survey of edge elements and a description of some simple scattering and eigenvalue computations. An alternative is the work of Silvester and Ferrari [112], in which basic one dimensional Lagrangian finite elements are covered in some detail before moving on to more advanced topics, including two and three–dimensional edge elements. The book by Volakis, Chaterjeee and Kempel [120] describes the basis functions for the lowest order edge elements on triangles and tetrahedra, while the applications considered include scattering and eigenvalue computations in both two and three–dimensions. Salazar–Palma, Sarkar, Garcia–Castillo Roy and Djordjevic [110] have produced a large text that considers many aspects of edge elements and includes tables of basis functions for different element types and for a selection of low polynomial degrees. Construction details for the elements also appear along with some details of error indicators and adaptive h–refinement strategies. Application to eigenvalue and scattering problems complements the theory.

The subject is approached from a mathematical standpoint in the book by Bossavit [31],

 ISSN: 1134–3060 Received: September 2004

which covers magnetostatics, infinite domains and eddy current problems. Here the material is presented from the perspective of differential forms. An alternative perspective is the functional approach adopted in the book by Monk [92]. This provides extensive coverage of the current mathematical theory regarding the approximation capabilities of edge based finite element methods, along with details of the construction of the elements. One chapter is completely devoted to recent algorithmic developments in the subject and engineers may find this to be particularly informative.

This article is organised as follows: In Section 2, an introductory overview of Maxwell's equations is given. This is followed by a history of edge element approximation in Section 3. Section 4 is devoted to some of the recent developments concerning the *hp*–version of the finite element method. Dispersive properties of $\boldsymbol{H}(\text{curl})$ conforming approximations are discussed in Section 5. Section 6 describes specific applications of $\boldsymbol{H}(\text{curl})$ conforming approximations to scattering problems and Section 7 concentrates on eigenvalue computations. In Section 8, a short discussion of some alternative non–conforming finite element approaches is provided.

2 MAXWELL's EQUATIONS

Electromagnetic phenomena are governed by Maxwell's equations. These equations relate the electric and magnetic field intensity vectors, denoted by $\boldsymbol{E}^*$ and $\boldsymbol{H}^*$ respectively, and the material properties of the medium. The full set of equations may be written as

$$\text{div } \boldsymbol{D}^* = \gamma \tag{1}$$

$$\text{div } \boldsymbol{B}^* = 0 \tag{2}$$

$$\text{curl } \boldsymbol{H}^* = \boldsymbol{J}^* + \frac{\partial \boldsymbol{D}^*}{\partial t} \tag{3}$$

$$\text{curl } \boldsymbol{E}^* = -\frac{\partial \boldsymbol{B}^*}{\partial t} \tag{4}$$

To complete the set, the continuity equation

$$\text{div } \boldsymbol{J}^* + \frac{\partial \gamma^*}{\partial t} = 0 \tag{5}$$

and the constitutive equations

$$\boldsymbol{D}^* = \epsilon \boldsymbol{E}^* \qquad \boldsymbol{B}^* = \mu \boldsymbol{H}^* \tag{6}$$

must be added. Here $\boldsymbol{D}^*$ is the electric flux density vector, γ is the electric charge density, $\boldsymbol{B}^*$ is the magnetic flux density vector and $\boldsymbol{J}^*$ is the electric current density vector. In addition, ϵ, μ, σ denote the permittivity, permeability and conductivity respectively of the medium.

In many practical problems, we can apply simplifying assumptions to the governing equation set. For present purposes, we will assume that

1. the medium obeys Ohm's Law, so that $\boldsymbol{J}^* = \sigma \boldsymbol{E}^* + \boldsymbol{J}^*_{app}$ where $\boldsymbol{J}^*_{app}$ is the applied current density used in source type problems (we will assume that $\boldsymbol{J}^*_{app}$ is zero throughout);

2. the electric charge density $\gamma = 0$;

3. the medium is non–lossy, so that $\epsilon, \mu \in \mathbb{R}$;

4. the conductivity of the medium $\sigma = 0$, although this assumption will later be relaxed in certain circumstances;
5. the permittivity and permeability of the medium do not vary in time;
6. the fields are time harmonic.

By imposing these conditions on the governing equations, and employing the constitutive equations, it can be deduced that

$$\begin{aligned} \text{curl } \boldsymbol{H} &= \mathrm{i}\epsilon\omega\boldsymbol{E} && (7)\\ \text{curl } \boldsymbol{E} &= -\mathrm{i}\mu\omega\boldsymbol{H} && (8)\\ \text{div } \epsilon\boldsymbol{E} &= 0 && (9)\\ \text{div } \mu\boldsymbol{H} &= 0 && (10) \end{aligned}$$

where the harmonic variation $e^{\mathrm{i}\omega t}$ has been assumed. The field quantities appearing in these equations are now to be regarded as the complex amplitudes of the respective fields. It can be observed that Maxwell's equations have now reduced to a set of two curl equations and two divergence equations, involving only the electric and magnetic field intensity vectors and two material properties. It is the numerical solution of this set of four equations that is of interest in this work.

2.1 Vector Wave Equations

The two curl equations may be combined to form either the vector wave equation

$$\text{curl } \left(\mu^{-1}\text{curl } \boldsymbol{E}\right) - \epsilon\omega^2\boldsymbol{E} = \boldsymbol{0} \tag{11}$$

for the electric field or the vector wave equation

$$\text{curl } \left(\epsilon^{-1}\text{curl } \boldsymbol{H}\right) - \mu\omega^2\boldsymbol{H} = \boldsymbol{0} \tag{12}$$

for the magnetic field. These are the usual starting point for frequency domain finite element solution algorithms. We elect to solve the vector wave equation for the electric field and to recover, when required, the magnetic field from equation (8). Associated with equation (11) is the divergence condition on the electric field. When solving for only the electric field, the divergence condition on the magnetic field becomes redundant. This is because the divergence of the curl of a continuous vector field is zero.

2.2 Boundary Conditions

These equations must be supplemented by appropriate boundary conditions. At the surface of a perfect electrical conductor (PEC), the electric and magnetic fields must be such that

$$\boldsymbol{n} \times \boldsymbol{E} = \boldsymbol{0} \qquad \boldsymbol{n} \cdot \boldsymbol{H} = 0 \tag{13}$$

where $\boldsymbol{n}$ is the unit outward normal vector to the surface $\partial\Omega$, i.e. the PEC boundary condition sets the tangential component of the electric field and the normal component of the magnetic field to zero. Correspondingly, at the surface of a perfect magnetic conductor (PMC), the fields must be such that

$$\boldsymbol{n} \times \boldsymbol{H} = \boldsymbol{0} \qquad \boldsymbol{n} \cdot \boldsymbol{E} = 0 \tag{14}$$

When problems formulated in infinite domains are considered, these conditions must be supplemented by suitable radiation conditions. However, we postpone the discussion of such conditions until later.

2.3 Interface Conditions

When regions of the domain have different material properties, one should impose at an interface between sub–domains a and b, the tangential jump conditions

$$\boldsymbol{n} \times (\boldsymbol{E}^a - \boldsymbol{E}^b) = \boldsymbol{0} \qquad \boldsymbol{n} \times (\boldsymbol{H}^a - \boldsymbol{H}^b) = \boldsymbol{0} \tag{15}$$

on the electric and magnetic fields and the normal jump conditions

$$\boldsymbol{n} \cdot (\epsilon^a \boldsymbol{E}^a - \epsilon^b \boldsymbol{E}^b) = 0 \qquad \boldsymbol{n} \cdot (\mu^a \boldsymbol{H}^a - \mu^b \boldsymbol{H}^b) = 0 \tag{16}$$

on the flux densities.

2.4 Variational Formulations

For problems in which the frequency is known, and is non–zero, the correct variational statement for this equation set, formulated in a bounded domain Ω, is [78]: find $\boldsymbol{E} \in \boldsymbol{H}(\mathrm{curl})$ such that

$$(\mu^{-1}\mathrm{curl}\,\boldsymbol{E}, \mathrm{curl}\,\boldsymbol{W})_\Omega - \omega^2(\epsilon\boldsymbol{E}, \boldsymbol{W})_\Omega = \ell(\boldsymbol{W}) \qquad \forall \boldsymbol{W} \in \boldsymbol{H}(\mathrm{curl}) \tag{17}$$

where

$$(\boldsymbol{u}, \boldsymbol{v})_\Omega = \int_\Omega \boldsymbol{u} \cdot \overline{\boldsymbol{v}}\, \mathrm{d}\Omega \tag{18}$$

denotes the L^2 inner product, the overbar denotes the complex conjugate and

$$\ell(\boldsymbol{W}) = -\int_{\partial\Omega} \boldsymbol{n} \times \mathrm{curl}\,\boldsymbol{E} \cdot \overline{\boldsymbol{W}} \mathrm{d}\Gamma \tag{19}$$

is a linear form. Specifically, we define the space

$$\boldsymbol{H}^{(3)}(\mathrm{curl}) = \{\boldsymbol{u} \in (L^2(\Omega))^3, \mathrm{curl}\,\boldsymbol{u} \in (L^2(\Omega))^3\} \tag{20}$$

for three–dimensional problems and the corresponding space

$$\boldsymbol{H}^{(2)}(\mathrm{curl}) = \{\boldsymbol{u} \in (L^2(\Omega))^2, \mathrm{curl}\,\boldsymbol{u} \in L^2(\Omega)\} \tag{21}$$

for two–dimensional problems. The $\boldsymbol{H}(\mathrm{curl})$ norm associated with these spaces is defined as

$$\|\boldsymbol{u}\|_{\boldsymbol{H}(\mathrm{curl})} = \left(\int_\Omega |\boldsymbol{u}|^2 + |\mathrm{curl}\,\boldsymbol{u}|^2 \mathrm{d}\Omega\right)^{1/2} \tag{22}$$

where $|\boldsymbol{u}|$ is the magnitude of the vector $\boldsymbol{u}$.

It should be noted here that it is also possible to introduce the space $\boldsymbol{H}(\mathrm{div})$, which is closely related to the space $\boldsymbol{H}(\mathrm{curl})$, and is defined as

$$\boldsymbol{H}^{(2)}(\mathrm{div}) = \{\boldsymbol{u} \in (L^2(\Omega))^2, \mathrm{div}\,\boldsymbol{u} \in L^2(\Omega)\} \tag{23}$$

with an obvious extension in three–dimensions. The $\boldsymbol{H}(\mathrm{div})$ norm is defined as

$$\|\boldsymbol{u}\|_{\boldsymbol{H}(\mathrm{div})} = \left(\int_\Omega |\boldsymbol{u}|^2 + |\mathrm{div}\,\boldsymbol{u}|^2 \mathrm{d}\Omega\right)^{1/2} \tag{24}$$

The DeRahm complex links the continuous fields which lie in different functional spaces through vector differential operators as [92]

$$H^1(\Omega) \overset{\nabla}{\longrightarrow} \boldsymbol{H}(\mathrm{curl}) \overset{\mathrm{curl}}{\longrightarrow} \boldsymbol{H}(\mathrm{div}) \overset{\mathrm{div}}{\longrightarrow} L^2(\Omega)$$

Similar diagrams may be constructed for the discrete fields used in finite element approximations, although this is beyond the scope of this work.

For reasons of stability, a variational formulation involving a Lagrange multiplier should be used to impose the divergence condition for problems with small, or possibly, zero frequencies which may occur for example in eigenvalue problems [74]. In this case, with PEC boundary conditions, a suitable formulation is: find $\boldsymbol{E} \in \boldsymbol{H}_0(\mathrm{curl})$ and $p \in H_0^1(\Omega)$ such that

$$(\mu^{-1}\mathrm{curl}\,\boldsymbol{E}, \mathrm{curl}\,\boldsymbol{W})_\Omega - \omega^2(\epsilon(\boldsymbol{E} + \nabla p), \boldsymbol{W})_\Omega = 0 \ \forall \boldsymbol{W} \in \boldsymbol{H}_0(\mathrm{curl}) \tag{25}$$

$$-\omega^2(\epsilon(\boldsymbol{E}, \nabla q)_\Omega = 0 \ \forall q \in H_0^1(\Omega) \tag{26}$$

where the spaces used here are defined as

$$\boldsymbol{H}_0(\mathrm{curl}) = \{\boldsymbol{u} \in \boldsymbol{H}(\mathrm{curl}), \boldsymbol{n} \times \boldsymbol{u} = \boldsymbol{0} \text{ on } \partial\Omega\} \tag{27}$$

$$H_0^1(\Omega) = \{p \in H^1(\Omega), p = 0 \text{ on } \partial\Omega\} \tag{28}$$

The Galerkin finite element approximation is obtained by replacing the continuous spaces introduced in this section by conforming discrete subspaces. The manner in which the basis functions for these discrete subspaces may be constructed will be discussed in more detail shortly.

2.5 Theoretical Results

We do not intend to delve to deeply into the theoretical issues that arise when approximating the solutions of Maxwell's equations by the finite element method, as there are already many articles and books which discuss this material, such as the survey article by Hiptmair [66] and the book by Monk [92]. Instead, we will follow a more engineering approach, supplemented with occasional mathematical diversions.

3 POPULARISATION OF EDGE ELEMENT APPROXIMATIONS

The origins of $\boldsymbol{H}(\mathrm{curl})$ conforming elements can be traced back to the early work of Whitney and geometric integration theory [128]. When Whitney's book was written, the finite element method was in its infancy and there was, consequently, no thought given to how these simplicial geometric constructions could be connected with the finite element solution of Maxwell's equations. Instead, the constructions were only used for geometrical interpolation purposes. Closely allied to geometric integration theory is the concept of differential forms discussed by Whitney and Table 1 shows how these can be related to the equivalent functional spaces. For a description of the differential forms approach to electromagnetics, the reader should refer to Hiptmair [66] and to the references therein. However, in this article, we shall prefer to employ the functional spaces to distinguish the different element types.

It was many years after the appearance of Whitney's paper that the importance of $\boldsymbol{H}(\mathrm{curl})$ approximations in finite elements was first realised. In 1980, Nédélec [101] gave

Differential Form	Functional Space	Element Type
0–form	H^1	Nodal
1-form	$\boldsymbol{H}(\text{curl})$	Edge /Nédélec
2-form	$\boldsymbol{H}(\text{div})$	Face / Raviart-Thomas
3-form	L^2	Discontinuous

Table 1. The links between differential forms and continuous functional spaces

the details of a recipe for the construction of $\boldsymbol{H}(\text{curl})$ and $\boldsymbol{H}(\text{div})$ conforming elements on tetrahedra and hexahedra. He also proposed the conditions which these elements should satisfy in order for them to be regarded as conforming. In particular, for an element to be $\boldsymbol{H}(\text{curl})$ conforming, Nédélec proposed that the tangential component of the approximation in two neighbouring elements should be equal on the common face. For $\boldsymbol{H}(\text{div})$ conforming elements, he propose that the normal component of the approximations in two neighbouring elements should be equal on the common face. It was Nédélec who first recognised the importance of these elements to the solution of problems in electromagnetism. He also proposed [102] a second family of $\boldsymbol{H}(\text{curl})$ conforming elements, with basis functions requiring double the number of unknowns. The new family produced a better convergence rate for the vector, but an identical convergence rate for the curl, when compared to the original family. Although Nédélec proposed recipes for the construction of $\boldsymbol{H}(\text{curl})$ conforming elements, there are many choices which can be adopted for the basis functions and these all have their respective advantages and disadvantages. For example, certain choices may lead to matrices which are ill–conditioned and difficult to solve, while others may be difficult to implement in computer programs. Subsequently, in the 1980s and the 1990s, many different sets of basis functions have been proposed and we briefly summarise these developments here.

We start by defining the basis functions for the lowest order $\boldsymbol{H}(\text{curl})$ conforming tetrahedral element of the Nédélec first family which, for many, is the quintessential edge element. Incidently, this basis coincides with the functions proposed by Whitney in his work on differential geometry. The basis functions, for the element illustrated in Figure 1, may be expressed as

$$\boldsymbol{\phi}_0^1 = \lambda_1\nabla\lambda_2 - \lambda_2\nabla\lambda_1 \qquad \boldsymbol{\phi}_0^2 = \lambda_1\nabla\lambda_3 - \lambda_3\nabla\lambda_1 \tag{29}$$

$$\boldsymbol{\phi}_0^3 = \lambda_2\nabla\lambda_3 - \lambda_3\nabla\lambda_2 \qquad \boldsymbol{\phi}_0^4 = \lambda_2\nabla\lambda_4 - \lambda_4\nabla\lambda_2 \tag{30}$$

$$\boldsymbol{\phi}_0^5 = \lambda_4\nabla\lambda_1 - \lambda_1\nabla\lambda_4 \qquad \boldsymbol{\phi}_0^6 = \lambda_4\nabla\lambda_3 - \lambda_3\nabla\lambda_4 \tag{31}$$

Here, the λ_i are the volume, or barycentric, coordinates associated with the 6 vertices of a straight sided tetrahedron and are the natural extension of the area coordinates for the triangle [112]. The gradient operators which appear in these definitions imply that the basis functions are vectors. The variation of the electric field over a tetrahedron element may then be approximated, on a discretisation of typical size H, as

$$\boldsymbol{E}_H = \sum_{e=1}^{6} u_e \boldsymbol{\phi}_0^e \tag{32}$$

where u_e denotes the scalar coefficient associated with edge e of the tetrahedron and the summation extends over all edges of the tetrahedron. These basis functions are such that $\boldsymbol{\tau}_e \cdot \boldsymbol{\phi}_0^e|_e = 1$ on edge e, where $\boldsymbol{\tau}_e$ is a unit tangent vector to edge e. This result implies that the scalar coefficient u_e represents an approximation to the tangential component of

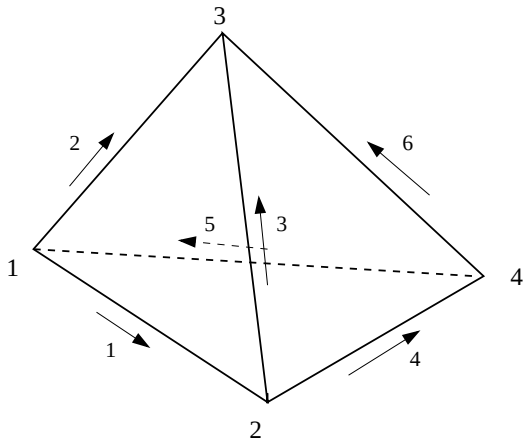

Figure 1. A typical straight–sided tetrahedron with vertex numbers and orientated edges

the electric field on edge e. The polynomial order $p = 0$ is associated with this element, because the tangential component of the field is represented by a single constant u_e on each edge. Note that, since the curl of each basis function is constant, curl $\boldsymbol{E}$ is approximated as a constant inside each element. Note also that the divergence of these basis functions is identically zero.

The lowest order $\boldsymbol{H}(\text{curl})$ conforming tetrahedral element of the Nédélec second family consists of the functions presented in equations (29-31), plus the functions

$$\boldsymbol{\phi}_1^1 = \lambda_1\nabla\lambda_2 + \lambda_2\nabla\lambda_1 \qquad \boldsymbol{\phi}_1^2 = \lambda_1\nabla\lambda_3 + \lambda_3\nabla\lambda_1 \tag{33}$$

$$\boldsymbol{\phi}_1^3 = \lambda_2\nabla\lambda_3 + \lambda_3\nabla\lambda_2 \qquad \boldsymbol{\phi}_1^4 = \lambda_2\nabla\lambda_4 + \lambda_4\nabla\lambda_2 \tag{34}$$

$$\boldsymbol{\phi}_1^5 = \lambda_4\nabla\lambda_1 + \lambda_1\nabla\lambda_4 \qquad \boldsymbol{\phi}_1^6 = \lambda_4\nabla\lambda_3 + \lambda_3\nabla\lambda_4 \tag{35}$$

The approximation to the electric field is expressed, in this case, as

$$\boldsymbol{E}_H = \sum_{e=1}^{6}\sum_{p=0}^{1} u_e^p \boldsymbol{\phi}_p^e \tag{36}$$

These basis functions are such that $\boldsymbol{\tau}_e \cdot \boldsymbol{\phi}_1^e|_e = -\xi$ on edge e, where $\xi \in [-1, 1]$ is a non–dimensional parameterization of the edge. The polynomial order $p = 1$ is associated with this element because the tangential component of the field is represented by a linear function of ξ on the edge. The curl of the basis functions (33-35) is zero, which leads to the observation made previously about the convergence of the second Nédélec family. In this case, we observe that the divergence of these basis functions is not identically zero.

The earliest reported use of $\boldsymbol{H}(\text{curl})$ conforming elements appears in the papers by Bossavit and Verite [34, 35] where the elements are employed in the solution of eddy current problems. In the second of these papers, more challenging examples are tackled. Mur and De Hoop [100] were the first to propose an example of a higher order $\boldsymbol{H}(\text{curl})$ conforming element. This was presented in the form of a $p = 1$ tetrahedron, with two degrees of freedom associated with each edge of the element. In a sequence of numerical tests, the new element performed better than the original $p = 0$ element. However, the authors felt that the computational costs of the improved element were too high for it to be of practical use. The first example of how the solution of eddy current problems might be obtained with non–tetrahedral elements appeared in the work of van Welij [118]. He developed

hexahedral elements, constructed along the lines previously suggested by Nédélec [101], but no numerical computations were reported. In 1984, Hano [60] proposed a rectangular edge element for the computation of resonant modes of waveguides. This paper is particularly interesting because it appears that this element was arrived at independently, without the prior knowledge of Nédélec's work. In addition, Hano appears to have been the first to realise that $\boldsymbol{H}(\text{curl})$ conforming elements could be applied to solve Maxwell cavity problems without the appearance of spurious modes in the solution. Barton and Cendes [21] proposed another possible recipe for generating the lowest order $\boldsymbol{H}(\text{curl})$ conforming elements on tetrahedra. Their elements are equivalent to the first family of Nédélec and they used them to solve magnetostatic problems, formulated in terms of the vector potential. This paper represents one of the first examples of the application of $\boldsymbol{H}(\text{curl})$ conforming elements to a wider class of electromagnetic problems. The relationship between Whitney elements and discrete differential forms is discussed in detail by Bossavit [30]. Further details and applications to eddy current problems can be found in another paper by Bossavit [29].

It is now that the number of applications of $\boldsymbol{H}(\text{curl})$ conforming elements begins to grow, the literature expands rapidly and edge elements are applied to a multitude of problems in electromagnetics, e.g. Bossavit and Mayergoz [33] proposed a hybrid boundary element/finite element scheme using $\boldsymbol{H}(\text{curl})$ conforming elements for the solution of electromagnetic scattering problems, while Kikuchi [74] addressed the solution of eigenvalue problems in electromagnetics. The development of higher order $\boldsymbol{H}(\text{curl})$ conforming elements on triangles and tetrahedra also begins to receive considerable attention. At the same time, there are developments in the creation of higher order quadrilateral and hexahedral elements, but these developments often appear completely separate from those on triangles and tetrahedra, so that hybrid discretisations are mostly not compatible. For this reason, we consider these two developments independently. A key development in the formation of higher order basis functions on hexahedra and quadrilaterals appears to be the introduction of the covariant projection elements of Crowley, Silvester and Hurwitz [45]. The idea is simple: first, create a set of basis functions for an element in a reference coordinate system and then map them to a general element in the domain. This approach is appealing, as it is much easier to design a higher order scheme on a reference element than on a general, possibly curved, element. The covariant projection represents the mapping which is, in turn, nothing other than the transposed (depending on definition) inverse of the Jacobian matrix. By following this approach, curved elements can also be handled without difficultly. In subsequent work, Miniowitz and Webb [89] designed a higher order quadrilateral element, notionally designated as being of degree $p = 1$, with 2 degrees freedom associated with each edge of the element and 5 associated with its interior. Shortly after the introduction of covariant projection elements, discussions began as to whether or not the use of these elements would circumvent the difficulty of spurious modes in the solution. It was already known that these parasitic modes could be avoided when the lowest order triangular/tetrahedral element was used and numerical experiments indicated that this was also true for covariant projection elements. It was initially believed, that the lowest order triangular element avoided spurious modes because the divergence of the basis functions was identically zero. The covariant projection element, like the earlier rectangular element of Hano [60], did not have this property. It was, therefore, suggested that these new elements prevented the appearance of spurious modes by satisfying the inclusion condition, which implies that the projections of the vector trial functions onto the irrotational space are contained in the space of vector trial functions. However, it was later shown that covariant projection elements, like tetrahedral elements, do not satisfy this property [36]. An alternative suggestion [36] was that the problem did not appear because the degree of polynomials of the functions in each coordinate directions is different for each component of the basis function vector on the reference element, but more theoretical justifications have

now appeared [28]. Kameari [71] proposed a higher order hexahedral element along the lines of the element of van der Welij [118]. This new element has 24 functions associated with the edges of the element and 2 associated with each face of the element. The element has a linear representation of the tangential component on the edges of the element and so is assigned the order $p = 1$. Improved numerical results were obtained for eddy current problems when the $p = 1$ hexahedral element was used in place of the previous $p = 0$ element.

Higher order basis functions have also been developed for triangular and tetrahedral elements. For example, Lee *et al.* [85] proposed a $p = 1$ triangular edge element, with two functions per edge and two interior functions. Subsequently, they applied their element to the calculation of resonant modes of waveguides with dielectric properties. They also presented an h–adaptive procedure for automatically refining the grid. A $p = 2$ triangular element, with three functions per edge and six interior functions, was proposed by Cendes [38], but no numerical investigations were reported. It is interesting to note that this element and the element proposed by Lee *et al.* [85] were designed in an ad–hoc fashion, with no attempt being made to develop a consistent procedure for designing higher order elements. A substantial breakthrough was the paper of Webb and Forghani [127], who proposed a hierarchical basis for $\boldsymbol{H}(\mathrm{curl})$ conforming tetrahedral elements with polynomial degrees ranging from $p = 0$ to $p = 3$. Accompanying basis functions for the scalar H^1 conforming elements with polynomial degrees $p = 1$ to $p = 4$ were also included. For the $p = 1$ $\boldsymbol{H}(\mathrm{curl})$ conforming element, there are two functions associated with each edge but, unlike the element of Lee *et al.* [85], there are no interior functions. Although the numerical examples in the paper are for uniform polynomial degree only, this hierarchical basis made adaptive p–refinement with $\boldsymbol{H}(\mathrm{curl})$ conforming elements feasible for the first time. However, it would be some time before the possibilities of adaptive p–refinement would be fully realised. Ideas for the possibility of developing curved higher order hexahedral and tetrahedral elements were proposed by Wang and Ida [121], following a similar approach to that adopted by Crowley *et al.* [45]. Spherical cavity problems were solved using the curvilinear elements and the advantages of using this approach, over one which uses straight sided elements, were demonstrated.

A symmetric triangular $p = 1$ element was suggested by Kameari [72], as a modification to the earlier $p = 1$ element proposed by Lee *et al.* [85]. Kameari viewed Lee's element as asymmetric as it had two interior functions, associated with normal components of the field on two of the three edges, so that the third edge was viewed as asymmetric. A $p = 2$ tetrahedral element was proposed by Ruiz-Genoveés *et al.* [109], with better conditioning properties than other available $p = 2$ tetrahedral elements.

In the late 90s, there was a resurgence of interest in the development of hierarchical $\boldsymbol{H}(\mathrm{curl})$ conforming elements and several new elements have since been suggested. Graglia *et al.* [58] proposed higher order elements which involve the multiplication of the lowest order $\boldsymbol{H}(\mathrm{curl})$ conforming basis functions by higher order interpolating polynomials. An alternative scheme was presented by Anderson and Volakis [14] and later modified [15]. Like the earlier hierarchical scheme of Webb and Forghani [127], the order of these elements was restricted to $p = 3$. The conditioning of the basis is not addressed in these papers, but the limited computational results demonstrate the improved accuracy that can be obtained with the new elements. An extension of $\boldsymbol{H}(\mathrm{curl})$ conforming tetrahedral elements to higher polynomial degree was proposed by Webb [126] and numerical experiments were presented up to $p = 4$. In addition, elements of shapes other than tetrahedra and hexahedra have also received attention. Gradinaru and Hiptmair [57] developed $\boldsymbol{H}(\mathrm{curl})$ and $\boldsymbol{H}(\mathrm{div})$ conforming elements on pyramids and the construction of an $\boldsymbol{H}(\mathrm{curl})$ conforming element on prisms is demonstrated in [120].

We remark that it was not until the work of Demkowicz and co–workers [53, 119, 47],

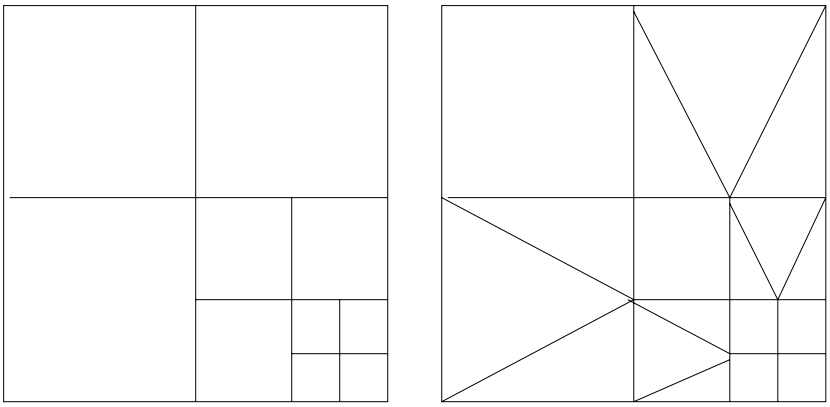

Figure 2. *h*–refinement strategies showing left, a strategy which allows hanging nodes and right a strategy which eliminates all hanging nodes

Ainsworth and Coyle [7, 9] and Ledger *et al.* [78, 83] that the possibilities offered by *hp*–refinement, using $\boldsymbol{H}(\text{curl})$ conforming elements, were fully explored. In later sections, we shall explore in more detail the construction of $\boldsymbol{H}(\text{curl})$ conforming elements for such approximations and demonstrate how these schemes may be applied to a range of problems in electromagnetism.

4 *hp* EDGE ELEMENT APPROACHES

4.1 Two–Dimensional Elements

Demkowicz and co–workers pioneered the application of *hp*–adaptive finite element techniques to electromagnetics [53, 119, 47]. In their early two–dimensional work, they proposed an arbitrary order triangular element and performed calculations with uniform polynomial order. The application to absorption problems ($\sigma > 0$) was considered [53] and a convergence analysis was presented [119]. They then described [47] a complete finite element package which allowed for the use of hybrid quadrilateral/triangular meshes with simultaneous h and p–refinement. A series of model problems were solved, without adaptivity [53, 119], to demonstrate the effectiveness of p–refinement. Computations undertaken with h–adaptivity were also reported [47], employing examples of cylinders with varying materials, waveguides and electrostatics. In this work, h–refinement was accomplished by subdividing elements and allowing hanging nodes and an illustration of two different h–refinement strategies, one which allows hanging nodes and one that does not, is given in Figure 2. We observe that the strategy which allows hanging nodes results in less elements and hence fewer degrees of freedom, although this is at the cost of a more complex implementation and data structure where, in general, the individual element edges and interiors are permitted to have different polynomial orders. The order p_i of the interior functions is always greater than, or equal to, the order p_e^j of the edge functions, where $j = 1, 2, 3$ for a triangle and $j = 1, 2, 3, 4$ for a quadrilateral. In an adaptive algorithm, one selects the elements which are to be subjected to a p–refinement and the new polynomial order is assigned to the interior, edge and face (in three–dimensions) functions of the element. The minimum rule [13] is adopted in which the degree of polynomial on an edge or on a face, is restricted to be equal to the order of the lowest polynomial employed on the elements which contain the edge, or contain the face.

Global error estimates ϖ are normally computed, by summing positive element contri-

butions, in the form

$$\varpi = \sum_{k \in \Omega} \varpi_k \tag{37}$$

where ϖ_k denotes the contribution from element k. A typical a–posteriori adaptive algorithm may then contain the steps:

1. input $\varrho \in (0,1)$ and $\varsigma > 0$;
2. set $X_0 = X_H$ and $i = 0$;
3. compute the Galerkin approximation $\boldsymbol{E}_H \in X_i$;
4. evaluate error estimators ϖ_k on each element;
5. If $\varpi \leq \varsigma$ then
   (a) stop;

   else
   (a) refine all elements k' such that $\varpi_{k'} \geq \varrho \max_k \varpi_k$;
   (b) construct a new subspace X_{i+1};
   (c) increment i and go to step 3.

In practice, an algorithm of this form may be used in an h–adaptive manner, where elements selected for refinement are subdivided, or in a p–adaptive manner, where the polynomial order of the elements selected for refinement is increased. As a further alternative, it can be used as the basis of a combined h and p–refinement algorithm but, in this case, the question of whether either h or p–refinement of an element should be performed arises. A possible approach here has been described by Ainsworth and Senior [13], in the context of linear elasticity, which depends on identification of the strength of the singularity that is being resolved. It should noted that the situation is often more complex in computational electromagnetism where, in wave propagation problems, as will be demonstrated later, one must also take careful account of dispersion. Recent computations of two–dimensional plane wave diffraction from an edge by Demkowicz [49] show, for the first time, fully adaptive combined *hp*–refinement for Maxwell's equations, with the decision of whether to perform either a h or p–refinement being based upon a comparison of the interpolation errors over two successive refinements.

Recently, Ainsworth and Coyle [7] have proposed an alternative hierarchical basis for triangles and quadrilaterals which has certain advantages over the basis proposed by Demkowicz. For example, numerical results for triangular and quadrilateral discretisations [7] show that the basis proposed by Ainsworth and Coyle has superior conditioning properties. The construction of the new basis functions is based upon the use of recursive relationships and Legendre polynomials. The recursive relationship provides a convenient method to generate the basis functions for higher order elements, while the Legendre polynomials are known to lead to well–conditioned matrices. This is an important property when considering iterative solution techniques. In Figure 3, we display the reference quadrilateral and triangular elements upon which the Ainsworth and Coyle basis functions are defined. The reference quadrilateral element is the square $[-1,1]^2$, while the reference triangle has vertices located at $(1,0)$, $(0,\sqrt{3})$ and $(-1,0)$.

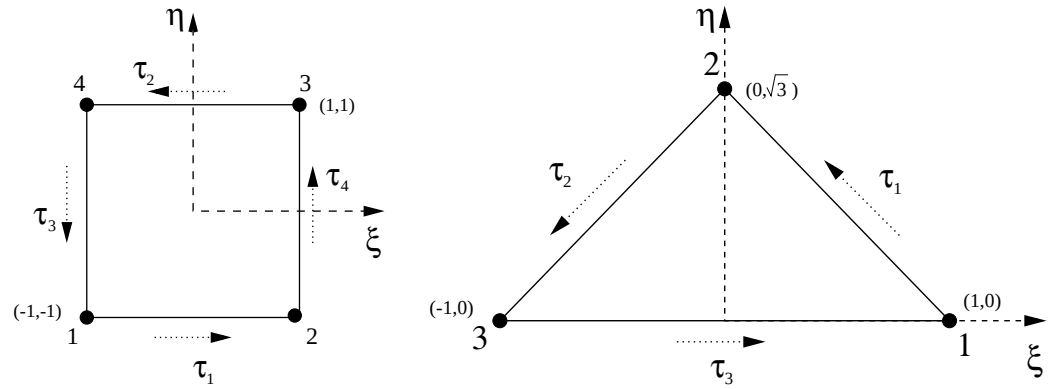

Quadilateral Reference Element Triangular Reference Element

Figure 3. Reference elements used in Ainsworth and Coyle's [7] hierarchical basis

Entity	Quadrilateral	Triangle
Vertices $p=1$	$\hat{\psi}_1 = \frac{1}{4}(1-\xi)(1-\eta)$ $\hat{\psi}_2 = \frac{1}{4}(1+\xi)(1-\eta)$ $\hat{\psi}_3 = \frac{1}{4}(1+\xi)(1+\eta)$ $\hat{\psi}_4 = \frac{1}{4}(1-\xi)(1+\eta)$	$\hat{\psi}_1 = \hat{\lambda}_1 = \frac{1}{2\sqrt{3}}(\sqrt{3}+\sqrt{3}\xi-\eta)$ $\hat{\psi}_2 = \hat{\lambda}_2 = \frac{\eta}{\sqrt{3}}$ $\hat{\psi}_3 = \hat{\lambda}_3 = \frac{1}{2\sqrt{3}}(\sqrt{3}-\sqrt{3}\xi-\eta)$
Edges $p \geq 2$	$\hat{\psi}_1^j = \frac{1}{2}\ell_j(\xi)(1-\eta)$ $\hat{\psi}_2^j = \frac{1}{2}\ell_j(-\xi)(1+\eta) \quad j=2,\cdots,p$ $\hat{\psi}_3^j = \frac{1}{2}\ell_j(-\eta)(1-\xi)$ $\hat{\psi}_4^j = \frac{1}{2}\ell_j(\eta)(1+\xi)$	$\hat{\psi}_1^j = \hat{\lambda}_1\hat{\lambda}_2\varphi_{j-2}(\hat{\lambda}_2-\hat{\lambda}_1)$ $\hat{\psi}_2^j = \hat{\lambda}_2\hat{\lambda}_3\varphi_{j-2}(\hat{\lambda}_3-\hat{\lambda}_2) \quad j=2,\cdots,p$ $\hat{\psi}_3^j = \hat{\lambda}_3\hat{\lambda}_1\varphi_{j-2}(\hat{\lambda}_1-\hat{\lambda}_3)$
Interiors $p \geq 2$	$\hat{\psi}^I_{j,k} = \ell_j(\xi)\ell_k(\eta)\ j,k=2\cdots p$	$\hat{\psi}^I_{j,k} = \hat{\lambda}_1\hat{\lambda}_2\hat{\lambda}_3 L_j(\hat{\lambda}_1-\hat{\lambda}_3)L_k(2\hat{\lambda}_2-1)$ $0 \leq j,k,j+k \leq p-3$

Table 2. Ainsworth and Coyle's [7] hierarchical H^1 conforming basis functions

We consider, initially, the H^1 conforming basis functions that are required when a mixed variational statement is employed. These may be decomposed into functions associated with the vertices, the edges and the interior of the element. The latter are also known as bubble functions as they are constructed to vanish on the edges of the elements. In Figure 3, the numbering relates to the vertices and edges. The hierarchical basis functions for the triangle and the quadrilateral are shown in Table 2, where ℓ_j denotes the integrated Legendre polynomial of degree j, L_j is the Legendre polynomial of degree j and the polynomial φ_j is defined as

$$\varphi_j(\xi) = \frac{-4}{(j+2)(j+1)} L'_{j+1}(\xi) \tag{38}$$

This polynomial is introduced to ensure compatibility of the edge basis functions on edges between neighbouring triangular and quadrilateral elements. Legendre polynomials are

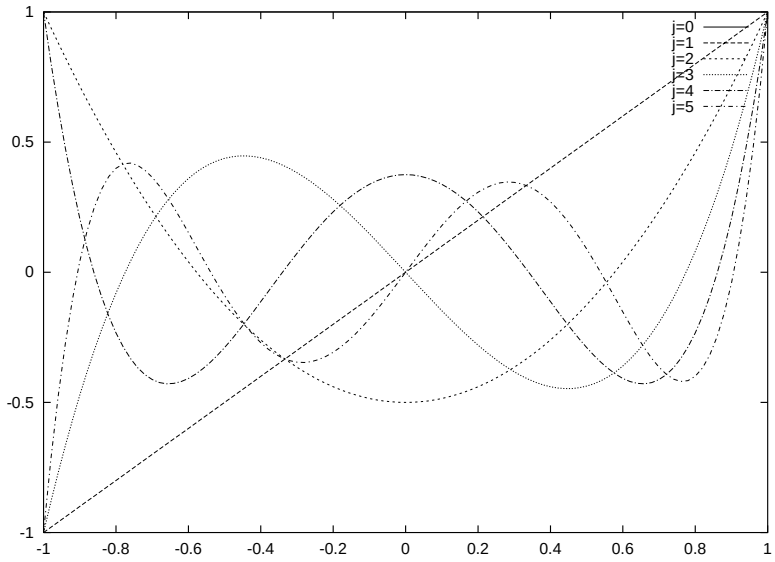

Figure 4. Legendre polynomial $L_j(\xi)$ for degrees $j = 0, 1, 2, 3, 4, 5$

defined over the interval $[-1, 1]$ and a plot of the first six such polynomials

$$L_0(\xi) = 1 \qquad L_1(\xi) = \xi \tag{39}$$

$$L_2(\xi) = (3\xi^2 - 1)/2 \qquad L_3(\xi) = (5\xi^3 - 3\xi)/2 \tag{40}$$

$$L_4(\xi) = (35\xi^4 - 30\xi^2 + 3)/8 \qquad L_5(\xi) = (63\xi^5 - 70\xi^3 + 15\xi)/8 \tag{41}$$

is shown in Figure 4. The polynomials satisfy the orthogonality property

$$\int_{-1}^{+1} L_i(\xi) L_j(\xi) \mathrm{d}\xi = \frac{2}{2i+1} \delta_{ij} \tag{42}$$

where $\delta_{ij} = 0$ is the kronecker delta. The integrated Legendre polynomial is defined as

$$\ell_i(\xi) = \int_{-1}^{\xi} L_{i-1}(s) \mathrm{d}s = \frac{L_i(\xi) - L_{i-2}(\xi)}{2i-1} \tag{43}$$

and these can be computed directly from the Legendre polynomials. The integrated Legendre polynomials have the special property that $\ell_i(\pm 1) = 0$ for each degree $i \geq 2$ and they are, therefore, particularly well suited for use in the construction of interior bubbles. In a practical implementation, the Legendre polynomials may be generated using the recursive relationship

$$(i+1) L_{i+1}(\xi) = (2i+1)\xi L_i(\xi) - i L_{i-1}(\xi) \tag{44}$$

starting with $L_0 = 1$ and $L_1 = \xi$. The derivatives of the Legendre polynomials can also be computed through the recursive relationship

$$(1 - \xi^2) L_i'(\xi) = i L_{i-1}(\xi) - i\xi L_i(\xi) \tag{45}$$

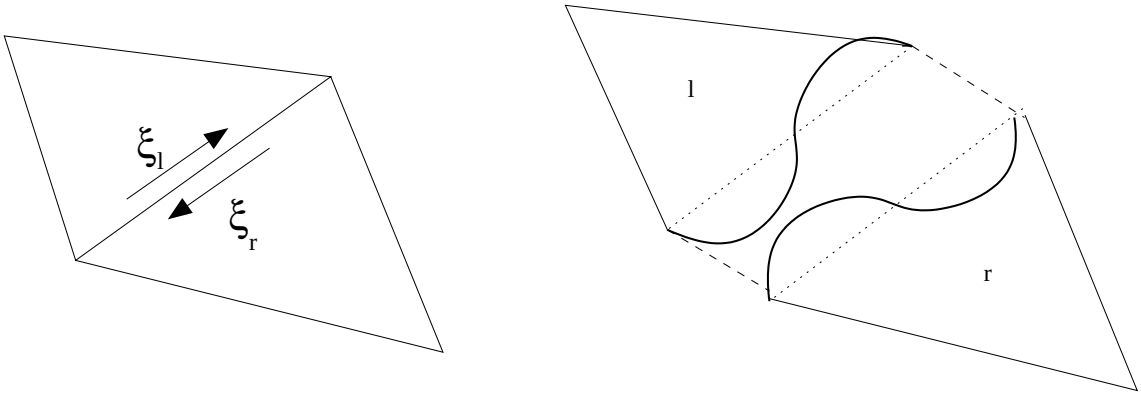

Figure 5. An example of a sign conflict problem for a cubic polynomial on an edge between two neighbouring triangular elements l and r

where the prime indicates differentiation with respect to the argument. The approximation of a scalar H^1 function u to degree $p \geq 1$ in terms of the basis functions shown in Table 2 is then given as

$$\hat{u}_H = \sum_{i=1}^{4} \hat{\psi}_i u_i + \sum_{i=1}^{4} \sum_{j=2}^{p} \hat{\psi}_i^j u_i^j + \sum_{j=2}^{p} \sum_{k=2}^{p} \hat{\psi}_{j,k}^I u_{j,k}^I \tag{46}$$

over the quadrilateral reference element and as

$$\hat{u}_H = \sum_{i=1}^{3} \hat{\psi}_i u_i + \sum_{i=1}^{4} \sum_{j=2}^{p} \hat{\psi}_i^j u_i^j + \underbrace{\sum_{j=0}^{p-3} \sum_{k=0}^{p-3}}_{j+k \leq p-3} \hat{\psi}_{j,k}^I u_{j,k}^I \tag{47}$$

over the reference triangular element.

When assembling the hierarchical H^1 conforming elements, we first impose continuity of the solution at the vertices of the elements in the standard way. Continuity is also enforced on edges between neighbouring elements and, here, care must be exercised: each edge has an associated intrinsic orientation and any sign conflict of the form

$$\ell_j(\xi_l) = (-1)^j \ell_j(\xi_r) \tag{48}$$

that arises, where ξ_l and ξ_r are the edge parameterizations of the adjacent left and right elements which are such that $\xi_l = -\xi_r$, must be resolved. An illustration of typical sign conflict problem is shown in Figure 5. This problem can be addressed by assigning a global direction to each edge in the mesh and multiplying those pth order local edge degrees of freedom whose local orientation is different to the global one by the factor $(-1)^p$. The interior bubbles remain independent in each element.

Ainsworth and Coyle's $\boldsymbol{H}^{(2)}(\mathrm{curl})$ conforming hierarchical basis functions are presented in Table 3. Using these functions, we can write an approximation to the electric field to degree $p \geq 0$ as

$$\hat{\boldsymbol{E}}_H = \sum_{i=1}^{4} \sum_{j=0}^{p} u_j^i \hat{\boldsymbol{\phi}}_j^i + \sum_{j=0}^{p} \sum_{k=1}^{p} u_{j,k}^{I_\xi} \hat{\boldsymbol{\phi}}_{j,k}^{I_\xi} + \sum_{j=0}^{p} \sum_{k=1}^{p} u_{j,k}^{I_\eta} \hat{\boldsymbol{\phi}}_{j,k}^{I_\eta} \tag{49}$$

Entity	Quadrilateral	Triangle
Edges ($p=0$)	$\hat{\boldsymbol{\phi}}_0^1 = \frac{1}{2}(1-\eta)\begin{pmatrix}1\\0\end{pmatrix}$ $\hat{\boldsymbol{\phi}}_0^2 = \frac{1}{2}(1+\eta)\begin{pmatrix}-1\\0\end{pmatrix}$ $\hat{\boldsymbol{\phi}}_0^3 = \frac{1}{2}(1-\xi)\begin{pmatrix}0\\-1\end{pmatrix}$ $\hat{\boldsymbol{\phi}}_0^4 = \frac{1}{2}(1+\xi)\begin{pmatrix}0\\1\end{pmatrix}$	$\hat{\boldsymbol{\phi}}_0^1 = \hat{\lambda}_1\hat{\nabla}\hat{\lambda}_2 - \hat{\lambda}_2\hat{\nabla}\hat{\lambda}_1$ $\hat{\boldsymbol{\phi}}_0^2 = \hat{\lambda}_2\hat{\nabla}\hat{\lambda}_3 - \hat{\lambda}_3\hat{\nabla}\hat{\lambda}_2$ $\hat{\boldsymbol{\phi}}_0^3 = \hat{\lambda}_3\hat{\nabla}\hat{\lambda}_1 - \hat{\lambda}_1\hat{\nabla}\hat{\lambda}_3$
Edges ($p=1$)	$\hat{\boldsymbol{\phi}}_1^1 = \frac{1}{2}(1-\eta)L_1(\xi)\begin{pmatrix}1\\0\end{pmatrix}$ $\hat{\boldsymbol{\phi}}_1^2 = \frac{1}{2}(1+\eta)L_1(-\xi)\begin{pmatrix}-1\\0\end{pmatrix}$ $\hat{\boldsymbol{\phi}}_1^3 = \frac{1}{2}(1-\xi)L_1(-\eta)\begin{pmatrix}0\\-1\end{pmatrix}$ $\hat{\boldsymbol{\phi}}_1^4 = \frac{1}{2}(1+\xi)L_1(\eta)\begin{pmatrix}0\\1\end{pmatrix}$	$\hat{\boldsymbol{\phi}}_1^1 = \hat{\lambda}_1\hat{\nabla}\hat{\lambda}_2 + \hat{\lambda}_2\hat{\nabla}\hat{\lambda}_1$ $\hat{\boldsymbol{\phi}}_1^2 = \hat{\lambda}_2\hat{\nabla}\hat{\lambda}_3 + \hat{\lambda}_3\hat{\nabla}\hat{\lambda}_2$ $\hat{\boldsymbol{\phi}}_1^3 = \hat{\lambda}_3\hat{\nabla}\hat{\lambda}_1 + \hat{\lambda}_1\hat{\nabla}\hat{\lambda}_3$
Edges ($p\geq 2$)	$\hat{\boldsymbol{\phi}}_j^1 = \frac{1}{2}(1-\eta)L_j(\xi)\begin{pmatrix}1\\0\end{pmatrix}$ $\hat{\boldsymbol{\phi}}_j^2 = \frac{1}{2}(1+\eta)L_j(-\xi)\begin{pmatrix}-1\\0\end{pmatrix}$ $\hat{\boldsymbol{\phi}}_j^3 = \frac{1}{2}(1-\xi)L_j(-\eta)\begin{pmatrix}0\\-1\end{pmatrix}$ $\hat{\boldsymbol{\phi}}_j^4 = \frac{1}{2}(1+\xi)L_j(\eta)\begin{pmatrix}0\\1\end{pmatrix}$ $j=2,\cdots,p$	$\hat{\boldsymbol{\phi}}_j^1 = \frac{1-2j}{j}L_{j-1}(\hat{\lambda}_2-\hat{\lambda}_1)\hat{\boldsymbol{\phi}}_1^1 - \frac{j-1}{j}L_{j-2}(\hat{\lambda}_2-\hat{\lambda}_1)\boldsymbol{\phi}_0^1$ $\hat{\boldsymbol{\phi}}_j^2 = \frac{1-2j}{j}L_{j-1}(\hat{\lambda}_3-\hat{\lambda}_2)\hat{\boldsymbol{\phi}}_1^2 - \frac{j-1}{j}L_{j-2}(\hat{\lambda}_3-\hat{\lambda}_2)\boldsymbol{\phi}_0^2$ $\hat{\boldsymbol{\phi}}_j^3 = \frac{1-2j}{j}L_{j-1}(\hat{\lambda}_1-\hat{\lambda}_3)\hat{\boldsymbol{\phi}}_1^3 - \frac{j-1}{j}L_{j-2}(\hat{\lambda}_1-\hat{\lambda}_3)\boldsymbol{\phi}_0^3$ $j=2,\cdots,p$
Interiors	$\hat{\boldsymbol{\phi}}_{j,k}^{I\xi} = L_j(\xi)\ell_k(\eta)\begin{pmatrix}1\\0\end{pmatrix}$ $\hat{\boldsymbol{\phi}}_{j,k}^{I\eta} = L_j(\eta)\ell_k(\xi)\begin{pmatrix}0\\1\end{pmatrix}$ $j=0,\cdots,p$ $k=2,\cdots,p+1$	$\hat{\boldsymbol{\phi}}_{1,j}^{PI} = \hat{\lambda}_1\hat{\lambda}_2\hat{\nabla}\hat{\lambda}_3 L_j(\hat{\lambda}_2-\hat{\lambda}_1)$ $\hat{\boldsymbol{\phi}}_{2,j}^{PI} = \hat{\lambda}_2\hat{\lambda}_3\hat{\nabla}\hat{\lambda}_1 L_j(\hat{\lambda}_3-\hat{\lambda}_2)$ $\hat{\boldsymbol{\phi}}_{3,j}^{PI} = \hat{\lambda}_3\hat{\lambda}_1\hat{\nabla}\hat{\lambda}_2 L_j(\hat{\lambda}_1-\hat{\lambda}_3)$ $j=0,\cdots,p-2$ $\hat{\boldsymbol{\phi}}_{j,k}^{GI\xi} = \hat{\lambda}_1\hat{\lambda}_2\hat{\lambda}_3(1-\hat{\lambda}_1)^j P_j^{2,2}\left(\frac{\hat{\lambda}_1-\hat{\lambda}_3}{1-\hat{\lambda}_2}\right)P_k^{2j+5,2}(2\hat{\lambda}_2-1)\boldsymbol{e}_\xi$ $\hat{\boldsymbol{\phi}}_{j,k}^{GI\eta} = \hat{\lambda}_1\hat{\lambda}_2\hat{\lambda}_3(1-\hat{\lambda}_1)^j P_j^{2,2}\left(\frac{\hat{\lambda}_1-\hat{\lambda}_3}{1-\hat{\lambda}_2}\right)P_k^{2j+5,2}(2\hat{\lambda}_2-1)\boldsymbol{e}_\eta$ $0\leq j,kj+k\leq p-3$

Table 3. Ainsworth and Coyle's [7] hierarchical $\boldsymbol{H}^{(2)}(\mathrm{curl})$ conforming basis functions

over the reference quadrilateral element and as

$$\hat{\boldsymbol{E}}_H = \sum_{i=1}^{3}\sum_{j=0}^{p} u_j^i\hat{\boldsymbol{\phi}}_j^i + \sum_{i=1}^{3}\sum_{j=0}^{p-2} u_{i,j}^{PI}\hat{\boldsymbol{\phi}}_{i,j}^{PI} + \underbrace{\sum_{j=0}^{p-3}\sum_{k=0}^{p-3}}_{j+k\leq p-3} u_{j,k}^{GI_\xi}\hat{\boldsymbol{\phi}}_{j,k}^{GI_\xi} + \underbrace{\sum_{j=0}^{p-3}\sum_{k=0}^{p-3}}_{j+k\leq p-3} u_{j,k}^{GI_\eta}\hat{\boldsymbol{\phi}}_{j,k}^{GI_\eta} \tag{50}$$

over the reference triangular element. The basis functions for $\boldsymbol{H}^{(2)}(\mathrm{curl})$ reside on the edges and the interiors of the quadrilateral and triangular elements. To construct these basis functions, we note that the Legendre polynomials are a special case of the Jacobi polynomials $P_j^{\alpha,\beta}$ with $\alpha=\beta=0$. Jacobi polynomials are defined on the interval $[-1,+1]$ and satisfy the orthogonality relationship

$$\int_{-1}^{+1} P_i^{\alpha,\beta}(\xi)P_j^{\alpha,\beta}(\xi)(1-\xi)^\alpha(1+\xi)^\beta \mathrm{d}\xi = \frac{2^{\alpha+\beta+1}\Gamma(i+\alpha+1)\Gamma(i+\beta+1)}{(2i+\alpha+\beta+1)i!\Gamma(i+\alpha+\beta+1)}\delta_{ij} \tag{51}$$

where Γ is the Gamma function. Abramowitz and Stegun [1], describe how the Jacobi polynomials can be generated recursively using the relationship

$$a_{1i}P_{i+1}^{\alpha,\beta}(\xi) = (a_{2i}+a_{3i}\xi)P_i^{\alpha,\beta}(\xi) - a_{4i}P_{i-1}^{\alpha,\beta}(\xi) \tag{52}$$

where

$$
\begin{aligned}
a_{1i} &= 2(i+1)(i+\alpha+\beta+1)(2i+\alpha+\beta) && (53)\\
a_{2i} &= (2i+\alpha+\beta+1)(\alpha^2+\beta^2) && (54)\\
a_{3i} &= (2i+\alpha+\beta)_3 && (55)\\
a_{4i} &= 2(i+\alpha)(i+\beta)(2i+\alpha+\beta+2) && (56)
\end{aligned}
$$

In the above the notation $(\cdot)_3 = \Gamma(\cdot+3)/\Gamma(\cdot)$ is employed, $P_0^{\alpha,\beta}(\xi) = 1$ and $P_1^{\alpha,\beta} = [\alpha-\beta+(\alpha+\beta+2)x]/2$. The derivatives of the Jacobi polynomials may be computed as

$$
P_i^{\alpha,\beta'}(\xi) = \frac{i(\alpha-\beta-(2i+\alpha+\beta)\xi)P_i^{\alpha,\beta}(\xi) + 2(i+\alpha)(i+\beta)P_{i-1}^{\alpha,\beta}(\xi)}{(2i+\alpha+\beta)(1-\xi^2)} \tag{57}
$$

Ainsworth and Coyle's hierarchical $\boldsymbol{H}^{(2)}(\text{curl})$ conforming basis has some interesting properties, e.g. if we evaluate the product of an edge tangent vector with a pth order edge basis function on that edge, we obtain*

$$
\boldsymbol{\tau}_e \cdot \boldsymbol{\phi}_p^e|_e = L_p(\xi_e) \tag{58}
$$

where ξ_e is the parameterization for edge e. This means that the interpolation of the tangential component of the basis is a Legendre polynomial on the edges of both the triangular and quadrilateral elements. This has important implications, as it is tangential continuity between elements that must be applied for an $\boldsymbol{H}(\text{curl})$ conforming approximation.

The application of non–zero Dirchlet boundary conditions requires the determination of the corresponding coefficients for the basis functions. For example, if we wish to apply the condition $\boldsymbol{\tau}_e \cdot \boldsymbol{E}_H = g$ on an edge e we could determine the coefficients u_e^j with $j = 0, \cdots, p$ from the linear equation system

$$
\left(\sum_{j=0}^{p} \boldsymbol{\tau}_e \cdot (u_j^e \boldsymbol{\phi}_j^e), \boldsymbol{\tau}_e \cdot \boldsymbol{\phi}_k^e \right)_e = (g, \boldsymbol{\tau}_e \cdot \boldsymbol{\phi}_k^e)_e \qquad \forall k = 0, \cdots, p \tag{59}
$$

where $(\cdot,\cdot)_e$ denotes the L^2 inner product on edge e.

A sign conflict problem also arises when considering the tangential components of edge basis functions on an edge between neighbouring elements, as

$$
L_j(\xi_l) = (-1)^j L_j(\xi_r) \tag{60}
$$

where ξ_l and ξ_r are the equal and opposite parameterizations for the edge on the neighbouring elements. This sign conflict problem can be addressed in the same manner as for the H^1 conforming functions. In this case, the local edge degrees of freedom whose local orientation is different to the global one should be multiplied by the factor $(-1)^{p+1}$. The tangential component of the interior basis functions for both the triangular and quadrilateral element vanish on the edges of their respective elements and so do not contribute to the continuity requirements.

*The $p = 1$ triangles are a special case: these have the property that $\boldsymbol{\tau}_e \cdot \boldsymbol{\phi}_1^e|_e = -L_1(\xi_e)$.

4.2 Three-Dimensional Elements

Rachowicz and Demkowicz [107] have developed a three–dimensional *hp*–finite element package for electromagnetics based upon hexahedral elements. Their approach allows for hanging nodes and for anisotropic refinement. They describe a data structure which allows such refinement, although they do not, currently, have strategy for the correct selection of the combination of h and p–refinements. Curved elements are allowed through the definition of a reference element and a geometric mapping. Numerical examples illustrate the effectiveness of the approach and these include scattering by rectangular waveguides, scattering by a radiating dipole, the absorption of electromagnetic waves by the human head and scattering of an electromagnetic wave by a generic aircraft. An alternative hexahedral $\boldsymbol{H}^{(3)}(\mathrm{curl})$ conforming element has been proposed by Ainsworth and Coyle [8], who also give theoretical estimates which bound the condition number of the mass and stiffness matrices for arbitrary order p. Hexahedral elements are an attractive choice for an *hp*–refinement strategy, as anisotropic refinement can easily be performed. However, meshing problems may be encountered when employing hexahedral elements for certain geometrical configurations. In such cases, unstructured tetrahedral meshes may need to be employed, as fully automatic generation procedures are available [125].

The sign conflict problem becomes much more complicated when considering three–dimensional $\boldsymbol{H}^{(3)}(\mathrm{curl})$ conforming tetrahedral discretisations, due to the occurrence of both edge based and face based basis functions and the requirement of tangential continuity of the basis between neighbouring tetrahedra. A solution to this problem and a consistent method for defining H^1, $\boldsymbol{H}^{(3)}(\mathrm{curl})$, $\boldsymbol{H}^{(3)}(\mathrm{div})$ and L^2 conforming tetrahedral elements has been proposed by Ainsworth and Coyle [9]. They assume that the domain Ω has already been partitioned into valid tetrahedral elements. The sets of basis functions employed for the discretised spaces of $\boldsymbol{H}^{(3)}(\mathrm{curl})$ and H^1 are suitable for non–uniform order of approximation throughout the partitioned domain and are developed to ease the task of enforcing appropriate continuity requirements of the respective spaces, while ensuring that properties of the De Rahm complex are satisfied [51]. The construction of these functions relies on a consistent orientation scheme for the edge and face interfaces that does not require any *a priori* knowledge of the adjacent elements. Each tetrahedron $\boldsymbol{t}$ is identified by its global vertex numbering $[o\,i\,j\,k]$, where it is assumed that $o < i, j < k$. The relation between i and j is either $i < j$ or $j < i$ and must be maintained during the orientation process. In an analogous manner, a face $\boldsymbol{f}$ may be denoted by $[o\,i\,j]$ and an edge $\boldsymbol{e}$ by $[o\,i]$ where, for these two entities, the assumption that $o < i < j$ is always valid. Finally, each edge $\boldsymbol{e}$ is parameterized in terms of $\xi_{\boldsymbol{e}} = \xi_{oi} = \lambda_i - \lambda_o$ and each face $\boldsymbol{f}$ is parameterized using ξ_{oi} and ξ_{oj} where λ_o, λ_i, λ_j and λ_k are the barycentric, or area, coordinates associated with the vertices. The orientation process leads to the conclusion that any physical tetrahedron $\boldsymbol{t}$ can be oriented in one of only two ways, as is illustrated in Figure 6, and this calls for the definition of two reference elements. The differential bijection relating the reference coordinate system $\boldsymbol{\xi} = [\xi, \eta, \zeta]$ and the physical coordinate system $\boldsymbol{x} = [x, y, z]$ is denoted by

$$\boldsymbol{F}_{\boldsymbol{t},i} : \hat{\boldsymbol{t}}_i \rightarrow \boldsymbol{t}$$

for $i = 1, 2$. Note that, in each case, the determination of $i = 1$ or 2 for each $\boldsymbol{t}$ amounts to a simple boolean check, as the correct association can easily be assigned by a mesh post–processing procedure. Explicit formulae for the reference element basis functions are given in Table 4. The reader should refer to the original paper [9] for the detailed construction and discussion of the underlying difficulties. An approximation of $\boldsymbol{E}$ to a degree $p \geq 0$ over

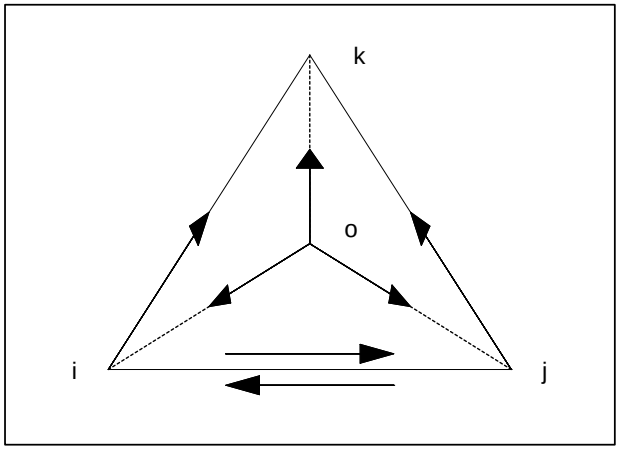

Figure 6. Tetrahedron with global vertex ordering $o < i, j < k$. The arrows indicate the possible orientations of each edge

the reference element using these basis functions is then given by

$$\begin{aligned}\hat{\boldsymbol{E}}_H = &\sum_{e=1}^{6}\sum_{\ell=0}^{p}\hat{\boldsymbol{\phi}}^e_\ell u^e_\ell + \sum_{f=1}^{4}\sum_{e\subset\partial f}\sum_{\ell=0}^{p-2}\hat{\boldsymbol{\phi}}^f_{e,\ell}u^f_{e,\ell} + \sum_{f=1}^{4}\underbrace{\sum_{\ell=0}^{p-3}\sum_{m=0}^{p-3}}_{\ell+m\le p-3}(\hat{\boldsymbol{\phi}}^f_{i,\ell m}u^f_{i,\ell m} + \hat{\boldsymbol{\phi}}^f_{j,\ell m}u^f_{j,\ell m})\\ &+\sum_{f=1}^{4}\underbrace{\sum_{\ell=0}^{p-3}\sum_{m=0}^{p-3}}_{\ell+m\le p-3}\hat{\boldsymbol{\phi}}^t_{f,\ell m}u^t_{f,\ell m} + \sum_{d=1}^{3}\underbrace{\sum_{\ell=0}^{p-4}\sum_{m=0}^{p-4}\sum_{n=0}^{p-4}}_{\ell+m+n\le p-4}\hat{\boldsymbol{\phi}}^t_{d,\ell mn}u^t_{d,\ell mn}\end{aligned} \tag{61}$$

To apply the Dirchlet boundary condition $\boldsymbol{n}\times\boldsymbol{E}_H = \boldsymbol{n}\times\boldsymbol{g}$ on a boundary face $\boldsymbol{f}$, the coefficients associated with the edge–based basis functions can be determined from the requirement that

$$\left(\sum_{j=0}^{p}\boldsymbol{\tau}_e\cdot(u^e_j\boldsymbol{\phi}^e_j), \boldsymbol{\tau}_e\cdot\boldsymbol{\phi}^e_k\right)_{\boldsymbol{e}} = (\boldsymbol{\tau}_e\cdot\boldsymbol{g}, \boldsymbol{\tau}_e\cdot\boldsymbol{\phi}^e_k)_{\boldsymbol{e}} \qquad \forall k = 0,\cdots,p \tag{62}$$

where $(\cdot,\cdot)_{\boldsymbol{e}}$ denotes an L^2 inner product on edge $\boldsymbol{e}$, and those associated with the edge–based face functions are determined from

$$\left(\boldsymbol{n}\times\boldsymbol{\phi}^f_{e,i}, \sum_{e\in\partial f}\sum_{j=0}^{p-2}u^f_{ej}\boldsymbol{n}\times\boldsymbol{\phi}^f_{ej}\right)_{\boldsymbol{f}} = \left(\boldsymbol{n}\times\boldsymbol{\phi}^f_{e,i}, \boldsymbol{n}\times\left\{\boldsymbol{g} - \sum_{e\in\partial f}\sum_{j=0}^{p}u^e_j\boldsymbol{\phi}^e_j\right\}\right)_{\boldsymbol{f}} \tag{63}$$

for $i = 0,\cdots p-2$, where $\boldsymbol{e}\in\partial\boldsymbol{f}$ and the notation $(\cdot,\cdot)_{\boldsymbol{f}}$ denotes an L^2 inner product associated with a face $\boldsymbol{f}$. The coefficients associated with the genuine face functions may

Associated DOF Entity	$H^1(\Omega)$–conforming	$\boldsymbol{H}(\mathrm{curl})$–conforming
Vertex	$\hat{\psi}^{\boldsymbol{v}} = \hat{\lambda}_{\boldsymbol{v}}$	$--$
Edge	$\hat{\psi}^{\boldsymbol{e}}_{\ell} = \hat{\beta}_{\boldsymbol{e}} L_\ell(\hat{\xi}_{oi})$	$\hat{\boldsymbol{\phi}}^{\boldsymbol{e}}_0 = \hat{\lambda}_i\hat{\nabla}\hat{\lambda}_o - \hat{\lambda}_o\hat{\nabla}\hat{\lambda}_i, \quad \hat{\boldsymbol{\phi}}^{\boldsymbol{e}}_1 = \hat{\lambda}_i\hat{\nabla}\hat{\lambda}_o + \hat{\lambda}_o\hat{\nabla}\hat{\lambda}_i$
$\boldsymbol{e} = [o\,i]$	$0 \le \ell \le p-2$	$\hat{\boldsymbol{\phi}}^{\boldsymbol{e}}_{\ell+1} = \frac{2\ell+1}{\ell+1} L_\ell(\hat{\xi}_{oi})\hat{\boldsymbol{\phi}}^{\boldsymbol{e}}_1 - \frac{\ell}{\ell+1} L_{\ell-1}(\hat{\xi}_{oi})\hat{\boldsymbol{\phi}}^{\boldsymbol{e}}_0$
		$1 \le \ell \le p-1$
Face	$\hat{\psi}^{\boldsymbol{f}}_{\ell m} = \hat{\beta}_{\boldsymbol{f}} L_\ell(\hat{\xi}_{oi}) L_m(\hat{\xi}_{oj})$	$\hat{\boldsymbol{\phi}}^{\boldsymbol{f}}_{\boldsymbol{e},\ell} = \hat{\beta}_{\boldsymbol{e}} L_\ell(\hat{\xi}_{oi})\hat{\nabla}\hat{\lambda}_{\boldsymbol{f}\backslash\boldsymbol{e}}$
$\boldsymbol{f} = [o\,i\,j]$	$0 \le \ell, m, \ell+m \le p-3$	$0 \le \ell \le p-2$
		$\hat{\boldsymbol{\phi}}^{\boldsymbol{f}}_{i,\ell m} = \hat{\beta}_{\boldsymbol{f}} L_\ell(\hat{\xi}_{oi}) L_m(\hat{\xi}_{oj})\hat{\boldsymbol{\tau}}^{[oi]}$
		$0 \le \ell, m, \ell+m \le p-3$
Interior	$\hat{\psi}^{\boldsymbol{t}}_{\ell mn} = \hat{\beta}_{\boldsymbol{t}} L_\ell(\hat{\xi}_{oi}) L_m(\hat{\xi}_{oj}) L_n(\hat{\xi}_{ok})$	$\hat{\boldsymbol{\phi}}^{\boldsymbol{t}}_{\boldsymbol{f},\ell m} = \hat{\beta}_{\boldsymbol{f}} L_\ell(\hat{\xi}_{oi}) L_m(\hat{\xi}_{oj})\hat{\nabla}\hat{\lambda}_{\boldsymbol{t}\backslash\boldsymbol{f}}$
$\hat{\boldsymbol{t}} = [o\,i\,j\,k]$	$0 \le \ell, m, n, \ell+m+n \le p-4$	$0 \le \ell, m, \ell+m \le p-3$
		$\hat{\boldsymbol{\phi}}^{\boldsymbol{t}}_{d,\ell mn} = \hat{\beta}_{\boldsymbol{t}} L_\ell(\hat{\xi}_{oi}) L_m(\hat{\xi}_{oj}) L_n(\hat{\xi}_{ok})\hat{\boldsymbol{e}}_d$
		$d \in \{1,2,3\}; \quad 0 \le \ell, m, n, \ell+m+n \le p-4$

Table 4. Reference element basis functions for discrete subspaces $Z^H \subset H^1(\Omega)$ and $X^H \subset \boldsymbol{H}^{(3)}(\mathrm{curl})$. The functions are grouped by the tetrahedral entity with which they are associated. In the above formulas $\boldsymbol{f}\backslash\boldsymbol{e}$ represents the vertex in the face $\boldsymbol{f}$ not on edge $\boldsymbol{e}$ and $\boldsymbol{t}\backslash\boldsymbol{f}$ represents the vertex in the tetrahedron $\boldsymbol{t}$ not in the face $\boldsymbol{f}$. The functions L_p are the Legendre polynomials of degree p and $\hat{\beta}_{\boldsymbol{e}} = \hat{\lambda}_o\hat{\lambda}_i, \hat{\beta}_{\boldsymbol{f}} = \hat{\lambda}_o\hat{\lambda}_i\hat{\lambda}_j$ and $\hat{\beta}_{\boldsymbol{t}} = \hat{\lambda}_o\hat{\lambda}_i\hat{\lambda}_j\hat{\lambda}_k$ are the so–called bubble functions associated with an edge, face and tetrahedron respectively. The vector $\hat{\boldsymbol{\tau}}^{[o\,i]}$ denotes the unit tangent to the edge $[o\,i]$ and $\hat{\boldsymbol{e}}_d$ denotes the unit vector in the d direction

be determined from

$$\left(\boldsymbol{n}\times\boldsymbol{\phi}^f_{i,j\ell}, \sum_{m=0}^{p-3}\sum_{n=0}^{p-3} u^f_{i,mn}\boldsymbol{n}\times\boldsymbol{\phi}^f_{i,mn}\right)_{\boldsymbol{f}} = \left(\boldsymbol{n}\times\boldsymbol{\phi}^f_{i,j\ell}, \boldsymbol{n}\times\left\{\boldsymbol{g} - \sum_{e\in\partial f}\left[\sum_{j=0}^{p} u^e_j\boldsymbol{\phi}^e_j - \sum_{j=0}^{p-2} u^f_{ej}\boldsymbol{\phi}^f_{ej}\right]\right\}\right)_{\boldsymbol{f}} \tag{64}$$

for $0 \le j+\ell, j, \ell \le p-3$ and $m+n \le p-3$.

Before concluding this section we note that a new *hp*–finite element package is currently under development by the group headed by Schöberl at Johannes Kepler University in Linz, Austria. This work aims to incorporate many of the ideas for *hp*–finite element technology that have been developed by Demkowicz and Ainsworth and their coworkers together with high order basis functions and efficient solution techniques. More details on these developments can be found at http://www.hpfem.jku.at/.

4.3 Geometry Representation and Covariant Projection

4.3.1 Affine mappings

When the mesh is composed only of straight–sided elements, a mapping of the coordinates from the reference element to a general element can be achieved through an affine mapping. For the affine mapping, we only use the vertex functions associated with a H^1 conforming discretisation of the element. For two–dimensional computations this mapping is

$$\begin{pmatrix} x \\ y \end{pmatrix} = \sum_{i=1}^{N^v} \hat{\psi}_i \begin{pmatrix} x_i \\ y_i \end{pmatrix} \tag{65}$$

where N^v is the number of vertices in the element and $(x_i, y_i)^T$ are the nodal coordinates of the vertices. For three–dimensional computations based on tetrahedra, the mapping becomes

$$\begin{pmatrix} x \\ y \\ z \end{pmatrix} = \sum_{i=1}^{4} \hat{\psi}_i \begin{pmatrix} x_i \\ y_i \\ z_i \end{pmatrix} \tag{66}$$

where $\hat{\psi}_i = \hat{\lambda}_i$ are the area coordinates associated with the vertices of the tetrahedral element.

4.3.2 Curved elements

The terms *sub–parametric*, *iso–parametric* and *super–parametric* [129] are associated with geometry representation and higher order elements. Recall that *sub–parametric* is used to describe a mapping in which the geometry is approximated to a lower degree than the field variable. *Iso–parametric* represent a mapping in which both the geometry and the field variable are approximated to the same degree, while *super–parametric* refers to a mapping in which the geometry is approximated to a higher degree than the field variable. When following an *hp*–finite element approach, the resolution of the geometry is generally achieved independently of the polynomial order. An approach which allows the use of large elements close to domain boundaries, in two dimensional problems, is the blending function approach and full details are given by Szabo and Babuska [116]. Further details regarding the implementation with edge elements can be found in [78]. Providing an accurate representation of curved boundaries with tetrahedral elements is more complicated and a number of possible approaches are discussed by Karniadakis and Sherwin [73]. A specific implementation, which uses the H^1 conforming basis on tetrahedra to provide bubble corrections on edges and faces is described by Coyle and Ledger [44] and demonstrated in the computation of Maxwell eigenvalues of curved cavities. An alternative approach to curved boundary representation is presented by Demkowicz and Oden [52] in the context of elastic wave scattering.

4.3.3 Covariant mappings

We now consider the mapping of the reference basis functions to a general (curvilinear) element and present formulas for the tetrahedral element. The corresponding two–dimensional case follows by simplification of these results [78]. In mixed variational formulations, gradients of H^1 conforming basis functions need to be computed and this may be achieved by employing a covariant transformation [114]. On a physical element $\boldsymbol{t}$, a global $H^1(\Omega)$–conforming basis function $\psi \in Z^H$ is then defined as

$$\psi(\boldsymbol{x})|_{\boldsymbol{t}} = \hat{\psi}(\boldsymbol{\xi}) \tag{67}$$

and the gradient of this function is defined as

$$\operatorname{grad}\psi(\boldsymbol{x})|_{\boldsymbol{t}} = \begin{pmatrix} \boldsymbol{a}_\xi & \boldsymbol{a}_\eta & \boldsymbol{a}_\zeta \end{pmatrix} \hat{\operatorname{grad}}\,\hat{\psi}(\boldsymbol{\xi}) \tag{68}$$

Here the columns $\boldsymbol{a}_\xi$, $\boldsymbol{a}_\eta$ and $\boldsymbol{a}_\zeta$ are the covariant vectors [114] given by

$$\begin{aligned} \boldsymbol{a}_\xi &= \begin{pmatrix} \frac{\partial x}{\partial \xi} & \frac{\partial y}{\partial \xi} & \frac{\partial z}{\partial \xi} \end{pmatrix}^T \\ \boldsymbol{a}_\eta &= \begin{pmatrix} \frac{\partial x}{\partial \eta} & \frac{\partial y}{\partial \eta} & \frac{\partial z}{\partial \eta} \end{pmatrix}^T \\ \boldsymbol{a}_\zeta &= \begin{pmatrix} \frac{\partial x}{\partial \zeta} & \frac{\partial y}{\partial \zeta} & \frac{\partial z}{\partial \zeta} \end{pmatrix}^T \end{aligned} \tag{69}$$

A global $\boldsymbol{H}(\mathrm{curl})$–conforming basis function $\boldsymbol{\phi} \in X^H$, defined on a physical element $\boldsymbol{t}$, is related to the corresponding reference element basis function $\hat{\boldsymbol{\phi}}$ as

$$\boldsymbol{\phi}(\boldsymbol{x})|_{\boldsymbol{t}} = \begin{pmatrix} \boldsymbol{a}^\xi & \boldsymbol{a}^\eta & \boldsymbol{a}^\zeta \end{pmatrix} \hat{\boldsymbol{\phi}}(\boldsymbol{\xi}) \tag{70}$$

where the columns $\boldsymbol{a}^\xi$, $\boldsymbol{a}^\eta$ and $\boldsymbol{a}^\zeta$ are the contravariant vectors given by

$$\begin{aligned} \boldsymbol{a}^\xi &= \frac{\boldsymbol{a}_\eta \wedge \boldsymbol{a}_\zeta}{\boldsymbol{a}_\xi \cdot \boldsymbol{a}_\eta \wedge \boldsymbol{a}_\zeta} \\ \boldsymbol{a}^\eta &= \frac{\boldsymbol{a}_\zeta \wedge \boldsymbol{a}_\xi}{\boldsymbol{a}_\xi \cdot \boldsymbol{a}_\eta \wedge \boldsymbol{a}_\zeta} \\ \boldsymbol{a}^\zeta &= \frac{\boldsymbol{a}_\xi \wedge \boldsymbol{a}_\eta}{\boldsymbol{a}_\xi \cdot \boldsymbol{a}_\eta \wedge \boldsymbol{a}_\zeta} \end{aligned} \tag{71}$$

The curl of $\boldsymbol{\phi}$ with respect to the physical coordinates $\boldsymbol{x}$ may then determined as

$$\begin{aligned} \operatorname{curl}\boldsymbol{\phi}(\boldsymbol{x})|_{\boldsymbol{t}} = \frac{1}{\boldsymbol{a}_\xi \cdot \boldsymbol{a}_\eta \wedge \boldsymbol{a}_\zeta} \Bigg[& \left(\frac{\partial \hat{\phi}_\zeta}{\partial \eta} - \frac{\partial \hat{\phi}_\eta}{\partial \zeta} \right) \boldsymbol{a}_\xi \\ & + \left(\frac{\partial \hat{\phi}_\xi}{\partial \zeta} - \frac{\partial \hat{\phi}_\zeta}{\partial \xi} \right) \boldsymbol{a}_\eta + \left(\frac{\partial \hat{\phi}_\eta}{\partial \xi} - \frac{\partial \hat{\phi}_\xi}{\partial \eta} \right) \boldsymbol{a}_\zeta \Bigg] \end{aligned} \tag{72}$$

where $\hat{\boldsymbol{\phi}}(\boldsymbol{\xi}) = (\hat{\phi}_\xi, \hat{\phi}_\eta, \hat{\phi}_\zeta)^T$.

To illustrate the covariant mapping process, consider an affine mapping of the edge basis functions $\boldsymbol{\phi}_1^0$ and $\boldsymbol{\phi}_4^0$ associated with the lowest order quadrilateral element, when the master element is mapped first to a rotated square and then to a deformed quadrilateral. The coordinates of the vertices of the square are $(1,0)^T$, $(0,1)^T$, $(-1,0)^T$ and $(0,-1)^T$ whilst those of the deformed quadrilateral are $(1,0)^T$, $(0.5,1)^T$, $(-0.5,0)^T$ and $(0.5,-1)^T$. The results of the mapping are shown in Figure 7, where we observe that the vector basis functions are only aligned with the respective edges in the case of the reference element and the rotated square. For the deformed quadrilateral, the basis functions are no longer aligned with the edges of the element and this is necessary if we are to ensure that the tangential component of the basis functions vanish on the other three edges of the element. This is the property that is required in order to preserve the tangential continuity of the approximation between elements, and for the element to be $\boldsymbol{H}(\mathrm{curl})$ conforming, as first noted by Nédélec.

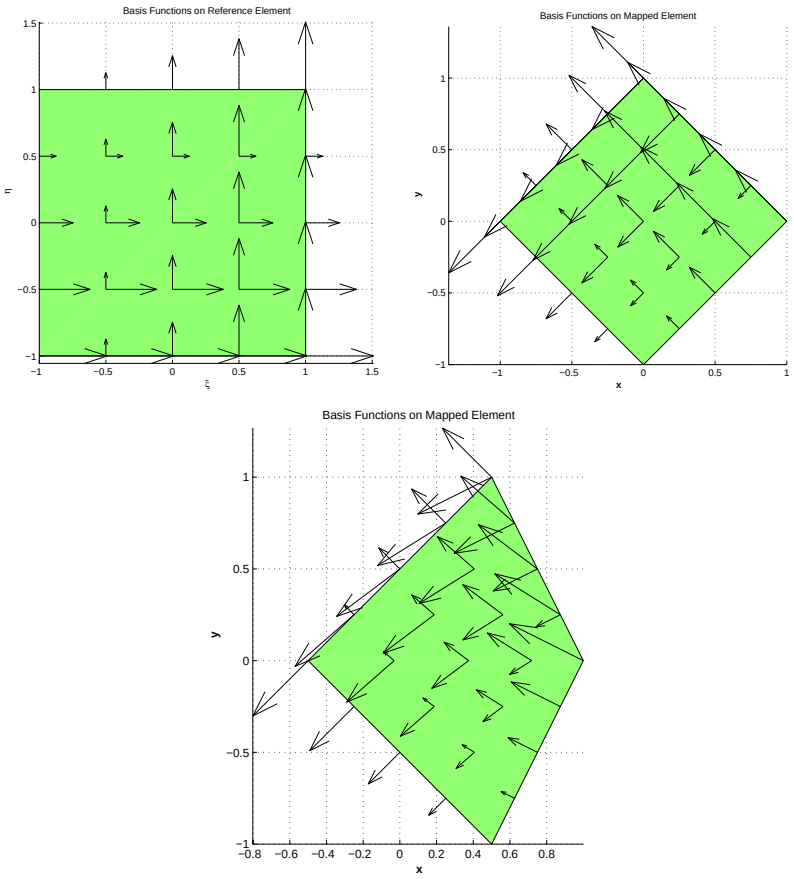

Figure 7. Covariant mapping of vector valued $\boldsymbol{H}(\mathrm{curl})$ conforming basis function showing vector plots of, (a), the functions on the reference element, (b), the functions on a rotated square and (c) on a deformed quadrilateral. Plots courtesy of K. Schmidt, Seminar for Applied Mathematics ETH Zürich

4.4 Numerical Integration

The element integrals are evaluated by using numerical integration techniques. The first step in this process is to express the integral in terms of an integral over the master element, by using the mapping process, in the form

$$\int_{\Omega^e} f(\xi,\eta,\zeta)\mathrm{d}\Omega = \int_{\hat{\Omega}^e} f(\xi,\eta,\zeta)(\boldsymbol{a}_\xi \cdot \boldsymbol{a}_\eta \wedge \boldsymbol{a}_\zeta)\,\mathrm{d}\hat{\Omega}^e \tag{73}$$

For quadrilateral elements, to approximate the integrals to sufficient accuracy, in the context of an *hp*–finite element scheme, Gauss–Legendre quadrature is applied in the tensor product form

$$\int_{\hat{\Omega}^e} f(\xi,\eta)(\boldsymbol{a}_\xi \cdot \boldsymbol{a}_\eta \wedge \boldsymbol{a}_\zeta)\,\mathrm{d}\Omega^e = \int_{-1}^{1}\int_{-1}^{1} f(\xi,\eta)(\boldsymbol{a}_\xi \cdot \boldsymbol{a}_\eta \wedge \boldsymbol{a}_\zeta)\,\mathrm{d}\xi\mathrm{d}\eta \tag{74}$$

$$\approx \sum_{i=1}^{N_{ip}}\sum_{j=1}^{N_{ip}} w_i w_j f(\xi_i,\eta_j)(\boldsymbol{a}_\xi \cdot \boldsymbol{a}_\eta \wedge \boldsymbol{a}_\zeta) \tag{75}$$

Here, w_i is the weight associated with the ith quadrature point of a N_{ip} point integration scheme. The situation is not so straightforward when the elements are triangles or tetrahedra. In this case, the approaches suggested by Stroud and Sescrest [115] or by Solin *et. al.* [113] may be followed, which results in a set of integration points capable of integrating high degree polynomials for computing the area and volume integrals.

4.5 Static Condensation

We now turn attention to issues relating to the equation solver. For simplicity, we assume that we wish to discretise the free space Maxwell wave propagation problem ($\epsilon = \mu = \boldsymbol{I}$), find $\boldsymbol{E} \in \boldsymbol{H}(\mathrm{curl})$ such that

$$(\mathrm{curl}\,\boldsymbol{E}, \mathrm{curl}\,\boldsymbol{W})_\Omega - \omega^2(\boldsymbol{E}, \boldsymbol{W})_\Omega = \ell(\boldsymbol{W}) \qquad \forall \boldsymbol{W} \in \boldsymbol{H}(\mathrm{curl}) \tag{76}$$

Furthermore we assume that the *hp*–edge element discretisation presented previously is employed. Then, typically, one wishes to evaluate elemental contributions for a element e

$$A^e_{ij} = \int_{\Omega^e} \mathrm{curl}\,\boldsymbol{\phi}_i \cdot \mathrm{curl}\,\boldsymbol{\phi}_j - \omega^2 \boldsymbol{\phi}_i \cdot \boldsymbol{\phi}_j \mathrm{d}\Omega \tag{77}$$

$$L^e_i = -\int_{\partial\Omega^e} \boldsymbol{n} \times \mathrm{curl}\,\boldsymbol{g} \cdot \boldsymbol{\phi}_i \mathrm{d}s \tag{78}$$

to the global matrix problem

$$\boldsymbol{A}\boldsymbol{u} = \boldsymbol{L} \tag{79}$$

As p increases, the dimension of this system may become large due to the fact that the number of interior basis functions increases as $O(p^2)$ in two–dimensions ($O(p^3)$ in three–dimensions). A remedy which keeps the system size manageable, is to employ the procedure of static condensation. In this context, this eliminates the degrees of freedom associated with the interior basis functions. First we partition the elemental matrices as

$$\boldsymbol{A}^e = \left(\begin{array}{c|c} \boldsymbol{A}^e_{cc} & \boldsymbol{A}^e_{ci} \\ \hline \boldsymbol{A}^e_{ic} & \boldsymbol{A}^e_{ii} \end{array} \right) \qquad \boldsymbol{L}^e = \left(\begin{array}{c} \boldsymbol{L}^e_c \\ \hline \boldsymbol{L}^e_i \end{array} \right) \tag{80}$$

where the subscript i refers to the those functions associated with the interior and the subscript c refers to the tangentially continuous component made up of edge (and face) functions. Eliminating the interior unknowns in each element means that we can, instead, solve the reduced global matrix problem

$$\boldsymbol{A}_r \boldsymbol{u}_r = \boldsymbol{L}_r \tag{81}$$

where the vector $\boldsymbol{u}_r$ just contains the degrees of freedom associated with edges (and faces). We assemble elemental contributions to this system as

$$\boldsymbol{A}^e_r = \boldsymbol{A}^e_{cc} - \boldsymbol{A}^e_{ci}(\boldsymbol{A}^e_{ii})^{-1}\boldsymbol{A}^e_{ic} \tag{82}$$

$$\boldsymbol{L}^e_r = \boldsymbol{L}^e_c - \boldsymbol{A}^e_{ci}(\boldsymbol{A}^e_{ii})^{-1}\boldsymbol{L}^e_i \tag{83}$$

Once the solution to equation (81) has been obtained one can determine the interior degrees of freedom using

$$\boldsymbol{u}^e_i = (\boldsymbol{A}^e_{ii})^{-1}(\boldsymbol{L}^e_i - \boldsymbol{A}^e_{ic}\boldsymbol{u}^e_c) \tag{84}$$

where $\boldsymbol{u}^e_i$ and $\boldsymbol{u}^e_c$ are respectively, the interior and continuous degrees of freedom associated with element e. In two–dimensions, we note that the numbering of the unknowns may be optimised so that the matrix $\mathbf{A}_r$ in the equation system (81) becomes banded [78].

5 IS 12pts PER WAVELENGTH ENOUGH? A QUESTION OF DISPERSION

The numerical errors in finite element solutions of wave propagation problems may be regarded as being due to two sources. The first source is the error due to interpolation of the continuous solution by discrete functions and the second is the pollution effect due to the phase lag between the computed and exact solution [54]. The pollution effect is often attributed to the difference between the computational and exact wave numbers and is also referred to as dispersion. Considerable success with reducing dispersion may be obtained by using an *hp*–version $\boldsymbol{H}(\text{curl})$ conforming finite elements to discretise Maxwell's equations [79, 78] where, for meshes of square elements, one can directly quantify the dispersion for a given mesh spacing h and polynomial order p [124, 7]. Here, we derive the well known dispersion relationship for the lowest order square elements and show how the underlying edge finite element stencil can be modified to give improved dispersive behaviour. Comments on dispersion on meshes of triangles and tetrahedra will also be given.

5.1 Two–Dimensional Square Edge Elements

For the purposes of this section, we restrict ourselves to square elements, where the basis functions may be readily obtained from the lowest order quadrilateral edge element basis functions of Section 4. Figure 8 shows a square element, with sides of length h, and the basis functions associated with edges of this element can be written as

$$\boldsymbol{\phi}_1 = \begin{pmatrix} (n+1) - y/h \\ \\ 0 \end{pmatrix} \qquad \boldsymbol{\phi}_2 = \begin{pmatrix} y/h - n \\ \\ 0 \end{pmatrix} \tag{85}$$

$$\boldsymbol{\phi}_3 = \begin{pmatrix} 0 \\ \\ (m+1) - x/h \end{pmatrix} \qquad \boldsymbol{\phi}_4 = \begin{pmatrix} 0 \\ \\ x/h - m \end{pmatrix} \tag{86}$$

We assume that the material parameters of the elements have value unity and we consider only interior elements in the mesh. To form the typical equations which occur in the global stiffness matrix for the vertical and horizontal edges, we need only consider the elements adjacent to the particular edge in question. Figure 9 shows two typical edges, labelled 1 and 3 and displayed in bold, together with their respective neighbouring elements, L and K for the vertical edge and K and M for the horizontal edge. Introducing the notation

$$a(\boldsymbol{E}_H, \boldsymbol{W}_H)_\Omega = (\text{curl}\, \boldsymbol{E}_H, \text{curl}\, \boldsymbol{W}_H)_\Omega - \omega^2 (\boldsymbol{E}_H, \boldsymbol{W}_H)_\Omega = 0 \tag{87}$$

and choosing $\boldsymbol{W}_H = \boldsymbol{\phi}_3$, with integration performed over K and L, gives

$$\begin{aligned} &a(\boldsymbol{\phi}_3, \boldsymbol{\phi}_3)_{K\cup L}\alpha_3 + a(\boldsymbol{\phi}_8, \boldsymbol{\phi}_3)_L\alpha_8 + a(\boldsymbol{\phi}_9, \boldsymbol{\phi}_3)_L\alpha_9 + a(\boldsymbol{\phi}_{10}, \boldsymbol{\phi}_3)_L\alpha_{10} \\ &+a(\boldsymbol{\phi}_2, \boldsymbol{\phi}_3)_K\alpha_2 + a(\boldsymbol{\phi}_4, \boldsymbol{\phi}_3)_K\alpha_4 + a(\boldsymbol{\phi}_1, \boldsymbol{\phi}_3)_K\alpha_1 = 0 \end{aligned} \tag{88}$$

where the basis functions for edges $5, 6, 7, 8, 9$ and 10 may be derived in a similar fashion to those presented in equations (85) and (86). The parameters $\alpha_1, \alpha_2, \alpha_3, \alpha_4, \alpha_8, \alpha_9$ and α_{10} represent the degrees of freedom associated with the tangential moments of the field $\boldsymbol{E}_H$ on the element edges. The choice of $\boldsymbol{W}_H = \boldsymbol{\phi}_1$ in equation (87), and integration over K and M, yields

$$\begin{aligned} &a(\boldsymbol{\phi}_1, \boldsymbol{\phi}_1)_{K\cup M}\alpha_1 + a(\boldsymbol{\phi}_3, \boldsymbol{\phi}_1)_K\alpha_3 + a(\boldsymbol{\phi}_2, \boldsymbol{\phi}_1)_K\alpha_2 + a(\boldsymbol{\phi}_4, \boldsymbol{\phi}_1)_K\alpha_4 \\ &+a(\boldsymbol{\phi}_6, \boldsymbol{\phi}_1)_M\alpha_6 + a(\boldsymbol{\phi}_5, \boldsymbol{\phi}_1)_M\alpha_5 + a(\boldsymbol{\phi}_7, \boldsymbol{\phi}_1)_M\alpha_7 = 0 \end{aligned} \tag{89}$$

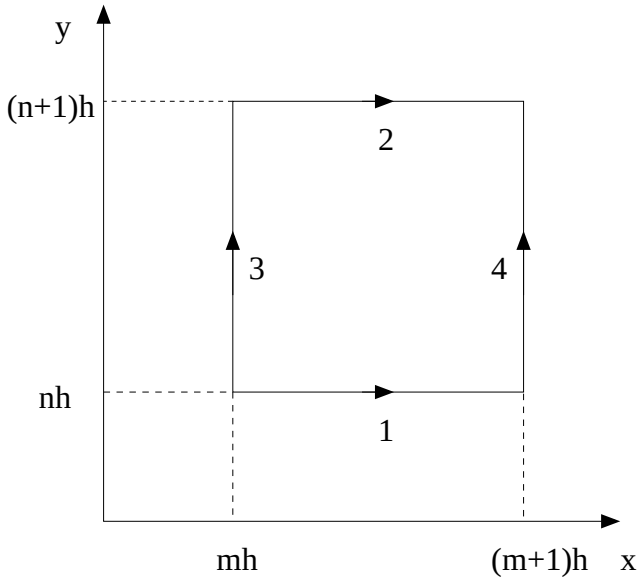

Figure 8. Square edge element with sides of length h

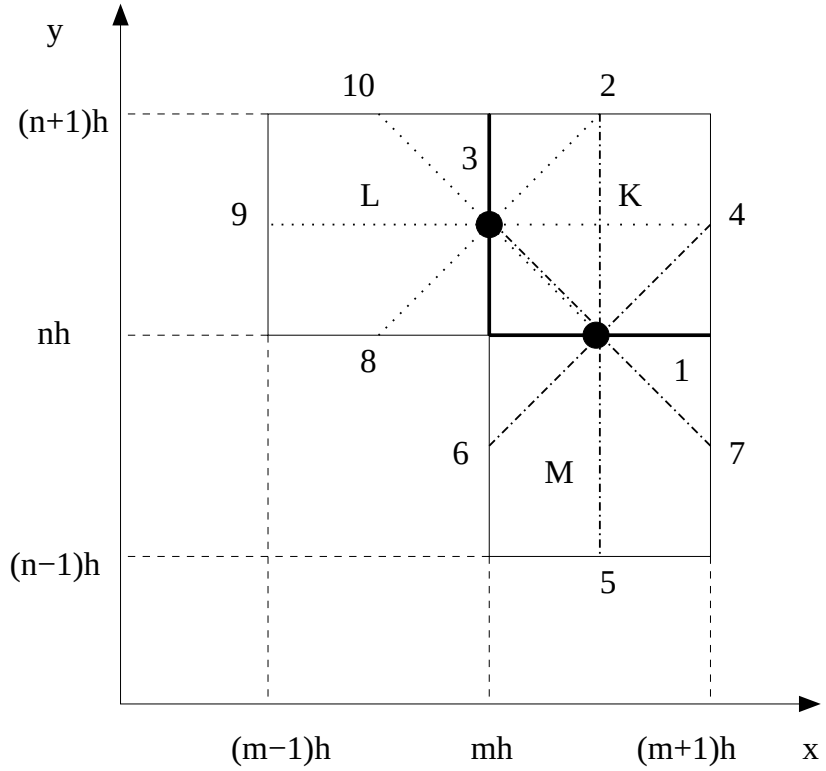

Figure 9. 3 Typical square elements, with edges considered for horizontal and vertical stencils shown in bold. The dotted lines show the linkages for a vertical stencil whereas the dashed–dotted lines show the linkages for a horizontal stencil

From equations (88) and (89), the vertical and horizontal stencils which represent the coefficients of the discretisation together with the associated continuity pattern of the square edge elements may be determined, leading to

$$\begin{bmatrix} & -1 & & & & 1 & \\ & & \ddots & & \iddots & & \\ -1 & \cdots & \cdots & 2 & \cdots & \cdots & -1 \\ & & \iddots & & \ddots & & \\ & 1 & & & & -1 & \end{bmatrix} - \omega^2 h \begin{bmatrix} & 0 & & & & 0 & \\ & & \ddots & & \iddots & & \\ \frac{1}{6} & \cdots & \cdots & \frac{2}{3} & \cdots & \cdots & \frac{1}{6} \\ & & \iddots & & \ddots & & \\ & 0 & & & & 0 & \end{bmatrix} \tag{90}$$

for the vertical stencil and

$$\begin{bmatrix} & & -1 & & & \\ & & \vdots & & & \\ -1 & & \vdots & & & 1 \\ & \ddots & \vdots & \iddots & & \\ & & 2 & & & \\ & \iddots & \vdots & \ddots & & \\ 1 & & \vdots & & & -1 \\ & & -1 & & & \end{bmatrix} - \omega^2 h \begin{bmatrix} & & \frac{1}{6} & & & \\ & & \vdots & & & \\ 0 & & \vdots & & & 0 \\ & \ddots & \vdots & \iddots & & \\ & & \frac{2}{3} & & & \\ & \iddots & \vdots & \ddots & & \\ 0 & & \vdots & & & 0 \\ & & \frac{1}{6} & & & \end{bmatrix} \tag{91}$$

for the horizontal stencil. The patterns given in these equations follow the shape of the lines depicted in Figure 9. If we assume that the discrete solution is the interpolant of the plane wave

$$\boldsymbol{E}_H = \boldsymbol{E}_0 \exp\{\mathrm{i}(\xi_x x + \xi_y y)\} \tag{92}$$

then the solution coefficients can be written, in terms of either α_1 or α_3, as

$$\begin{aligned} \alpha_2 &= \alpha_1 \exp\{\mathrm{i}\xi_y h\} & \alpha_4 &= \alpha_3 \exp\{\mathrm{i}\xi_x h\} \\ \alpha_5 &= \alpha_1 \exp\{-\mathrm{i}\xi_y h\} & \alpha_6 &= \alpha_3 \exp\{-\mathrm{i}\xi_x h\} \\ \alpha_8 &= \alpha_1 \exp\{-\mathrm{i}\xi_x h\} & \alpha_7 &= \alpha_3 \exp\{\mathrm{i}h(\xi_x - \xi_y)\} \\ \alpha_{10} &= \alpha_1 \exp\{\mathrm{i}h(\xi_y - \xi_x)\} & \alpha_9 &= \alpha_3 \exp\{-\mathrm{i}\xi_x h\} \end{aligned} \tag{93}$$

Following the approach of Ainsworth and Coyle [7], we first consider the horizontal edge, and insert the relevant solution coefficients, to obtain the condition

$$P\alpha_1 + Q\alpha_3 = 0 \tag{94}$$

where

$$\begin{aligned} P &= 2(1 - \cos(h\xi_y) - \left(\omega^2 h^2/3\right)(2 + \cos(h\xi_y)) \\ Q &= -1 + \exp\{\mathrm{i}\xi_x h\} + \exp\{-\mathrm{i}\xi_y h\} - \exp\{\mathrm{i}h(\xi_x - \xi_y)\} \end{aligned} \tag{95}$$

Following a similar procedure for the vertical edge produces the requirement

$$Q^*\alpha_1 + R\alpha_3 = 0 \tag{96}$$

where $*$ denotes the complex conjugate and

$$R = 2(1 - \cos(h\xi_x) - \left(\omega^2 h^2/3\right)(2 + \cos(h\xi_x)) \tag{97}$$

Equations (94) and (96) admit a non–trivial solution α_1, α_3 only if $PR = QQ^*$ and this leads to the discrete dispersion relation

$$\omega^2 - \frac{6}{h^2}\frac{1 - \cos(h\xi_x)}{2 + \cos(h\xi_x)} - \frac{6}{h^2}\frac{1 - \cos(h\xi_y)}{2 + \cos(h\xi_y)} = 0 \tag{98}$$

If $h\xi_x$ and $h\xi_y$ are assumed small, it follows that

$$\omega^2 - \left(\xi_x^2 + \xi_y^2 + \frac{1}{12}h^2(\xi_x^4 + \xi_y^4)\right) = O(h^4|\boldsymbol{\xi}|^6) \tag{99}$$

where $\boldsymbol{\xi} = (\xi_x, \xi_y)^T$, and this allows a quantification of the magnitude of the dispersion. From this equation, we can observe that the rule of thumb which implies using a fixed number of elements per wavelength is not appropriate for all cases, as the the dispersion increases with ω.

A generalisation of this dispersion relationship to the case of arbitrary order quadrilateral edge elements was obtained by Ainsworth [5]. In this case, the corresponding result is

$$\begin{aligned}\omega^2 - \left(\xi_x^2 + \xi_y^2 + \frac{h^{2(p+1)}}{2(p+1)+1}\left(\frac{(p+1)!}{(2(p+1))!}\right)\left(\xi_x^{2(p+1)+2} + \xi_y^{2(p+1)+2}\right)\right) \\ = O(h^{2(p+1)+2})\end{aligned} \tag{100}$$

and again it is apparent that the use of a fixed polynomial degree, p, for each wave frequency is inappropriate.

An insight into the effects of dispersion is revealed if one examines the propagation of a plane wave across the unit square [78]. We consider discretisations consisting of 1, 4, 16, 64, 256 and 1024 square $p = 0$ edge elements and compare the quality of the solution with that of a single square element of order $p = 0, 1, 2, 3, 4, 5$. In Figure 10, we show the results of the finite element computations for the x component of the electric field when the uniformly refined meshes are employed. We observe that, as the spacing is reduced, the solution initially lags behind the true wave and eventually tends towards the true wave. We consider the case of p–refinement in Figure 11. Here, we observe that the initial p–refinement does not improve the solution. However further increases in p lead to a very rapid convergence of the solution. Tables 5 and 6 give the number of unknowns required to compute the different solutions. Comparing these statistics and the solutions, it is clear that, based on number of unknowns alone, the p–refinement approach is a much more computationally effective approach.

In general, one may use the expressions given in equations (99) and (100) to generate initial discretisations in which the dispersion is already under control. This enables the rapid computation of accurate solutions without performing many refinement levels.

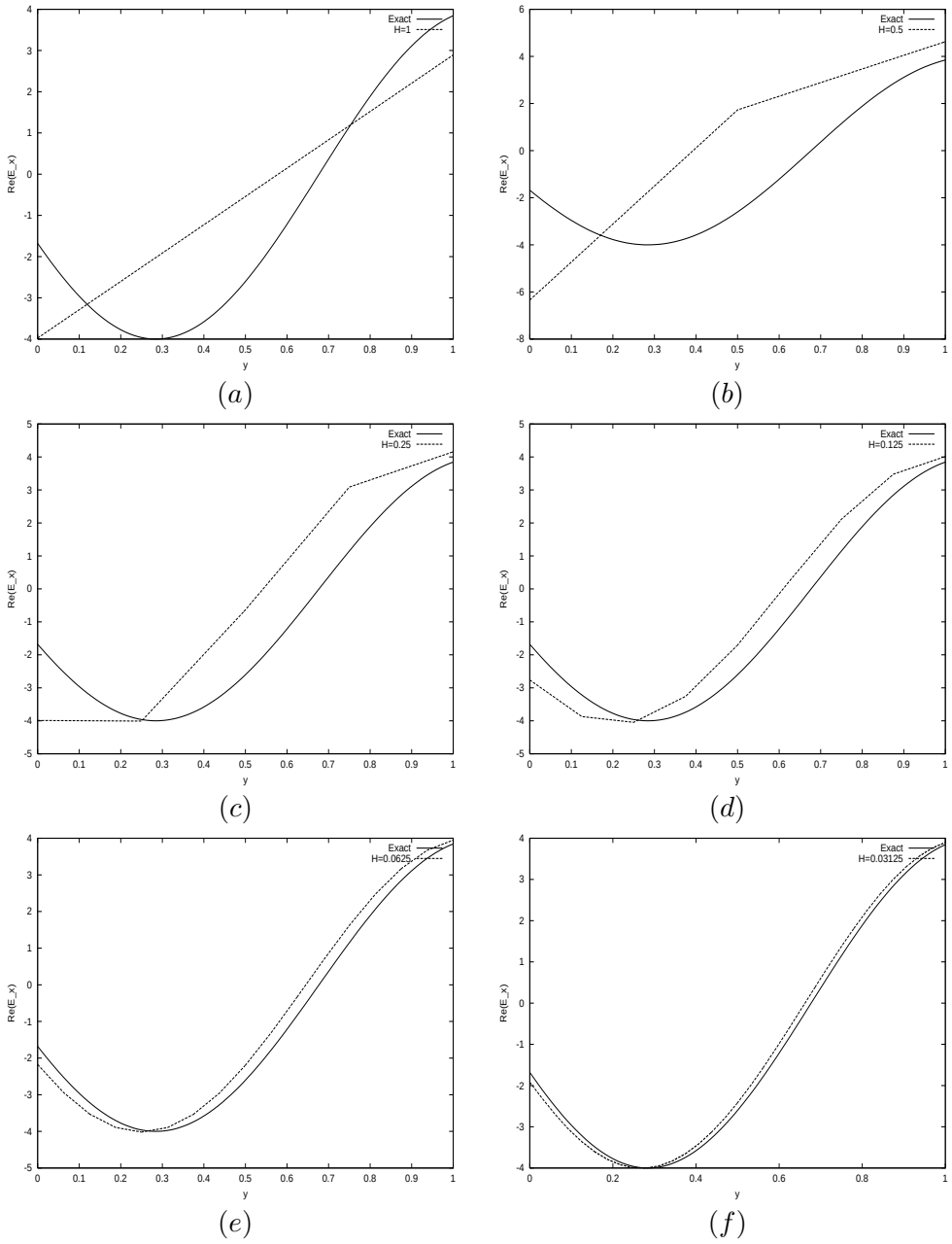

Figure 10. Dispersion in the wave propagation problem for meshes of quadrilaterals with uniform $p = 0$ and mesh spacings: (a) $h = 1$, (b) $h = 0.5$, (c) $h = 0.25$, (d) $h = 0.125$, (e) $h = 0.0625$ and (f) $h = 0.03125$

5.1.1 Modification to the stencil

An approach which attempts to modify the underlying finite element stencil has been proposed [68] along the lines of the generalised finite element method of Babuska, Sauter and coworkers [20, 19] for the Helmholtz equation. In this approach, the dispersion was eliminated for one–dimensional problems and minimised for two–dimensional simulations.

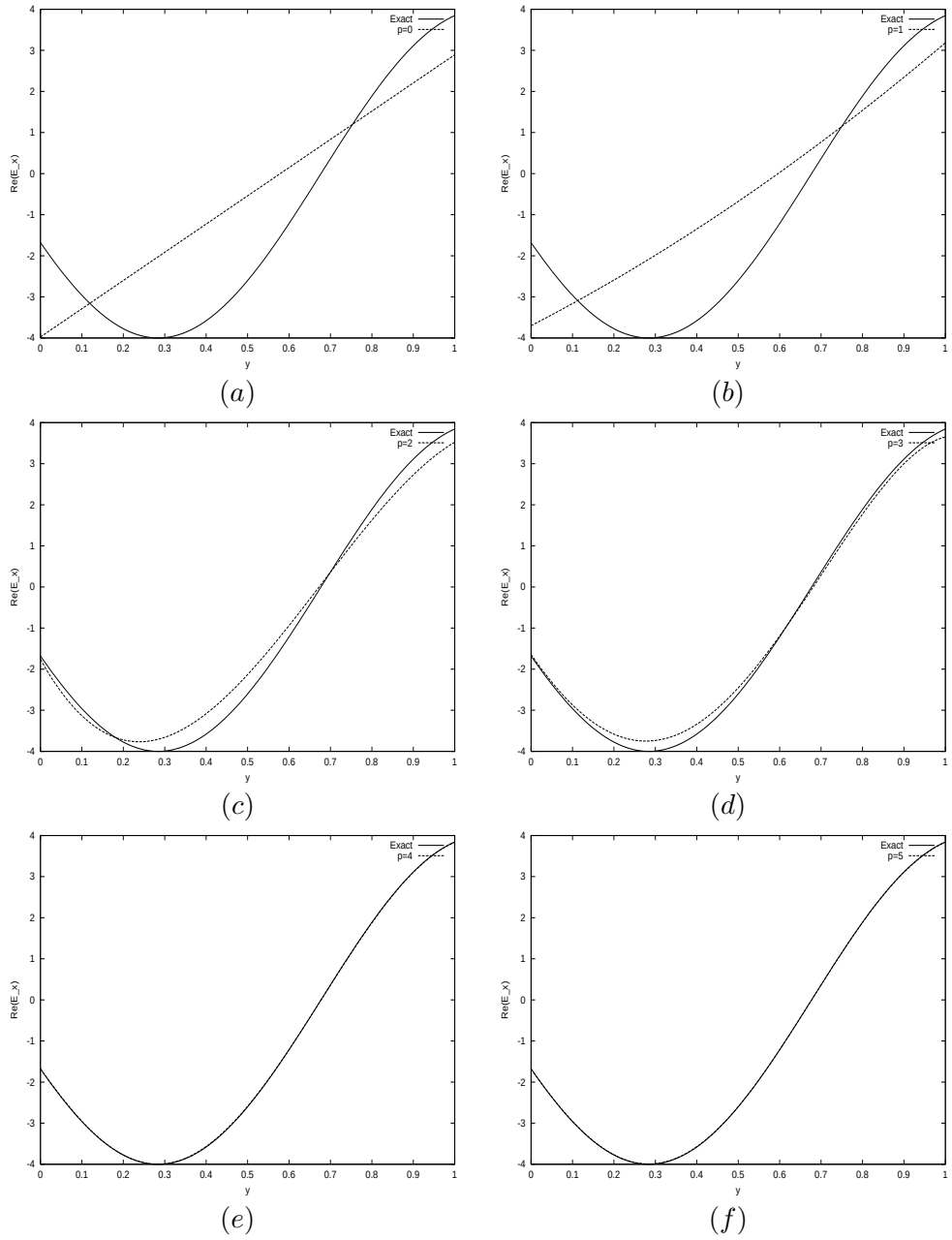

Figure 11. Dispersion in the wave propagation problem for meshes of quadrilaterals with spacing $h = 1$ and polynomial orders: (a) $p = 0$, (b) $p = 1$, (c) $p = 2$, (d) $p = 3$, (e) $p = 4$ and (f) $p = 5$

This was achieved by modifying the finite element stencil which arises when a uniform mesh of standard H^1 conforming 4–noded square elements is used. Adopting a similar approach, the finite element stencil for the lowest order quadrilateral edge element on a mesh of uniformly sized squares is modified to form a new stencil, with modification translated into a variation in the material coefficients for Maxwell's equations. This allows the natural

h	1	0.5	0.25	0.125	0.0625	0.03125
Number of Unknowns	4	12	40	144	544	2112

Table 5. Number of unknowns employed for the propagation of a plane wave with wavenumber $\xi_x = \xi_y = 4$ on a mesh of quadrilaterals with varying mesh spacing and uniform $p = 0$ elements

p	0	1	2	3	4	5
Number of Unknowns	4	12	24	40	60	80

Table 6. Number of unknowns employed for the propagation of a plane wave with wavenumber $\xi_x = \xi_y = 4$ on a mesh of quadrilaterals with spacing $h = 1$ and varying uniform order elements

incorporation of both Dirchlet and Neumann boundary conditions, something that was not possible without modification of the approach of Babuska and Sauter. The modified stencil is chosen to be of the form

$$\begin{bmatrix} & -b & & & & b & \\ & & \ddots & & \iddots & & \\ -b & \cdots & \cdots & 2b & \cdots & \cdots & -b \\ & & \iddots & & \ddots & & \\ & b & & & & -b & \end{bmatrix} - \omega^2 h \begin{bmatrix} & 0 & & & & 0 & \\ & & \ddots & & \iddots & & \\ c & \cdots & \cdots & 4c & \cdots & \cdots & c \\ & & \iddots & & \ddots & & \\ & 0 & & & & 0 & \end{bmatrix} \tag{101}$$

for the vertical stencil and

$$\begin{bmatrix} & & -b & & \\ -b & & \vdots & & b \\ & \ddots & \vdots & \iddots & \\ & & 2b & & \\ & \iddots & \vdots & \ddots & \\ b & & \vdots & & -b \\ & & -b & & \end{bmatrix} - \omega^2 h \begin{bmatrix} & & c & & \\ 0 & & \vdots & & 0 \\ & \ddots & \vdots & \iddots & \\ & & 4c & & \\ & \iddots & \vdots & \ddots & \\ 0 & & \vdots & & 0 \\ & & c & & \end{bmatrix} \tag{102}$$

for the horizontal stencil. Here, b and c are chosen as power series expansions of the form

$$b = \sum_{i=0}^{N} b_i \omega^{4i} h^{4i} \qquad c = \sum_{i=0}^{N} c_i \omega^{2i} h^{2i} \tag{103}$$

and the strategy for computing the coefficients is

1. Set $i = 0$, $b_0 = 1$, $c_0 = 1/6$ and $N = 4$;
2. $i = i + 1$;

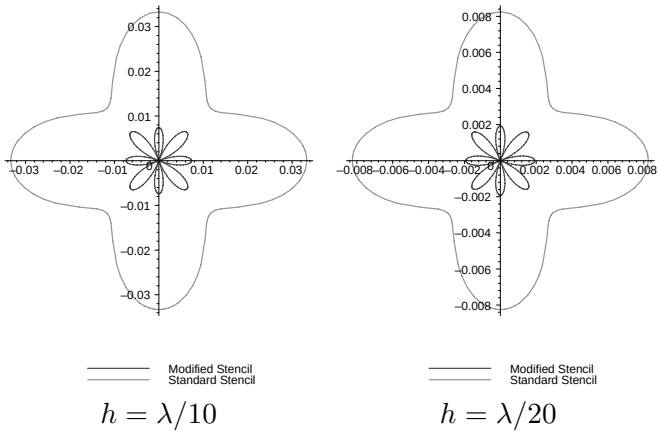

$h = \lambda/10$ $h = \lambda/20$

Figure 12. Polar graphs which compare the dispersive behaviour of the modified and standard edge finite element stencils as a function of angle for the case $\omega = 1$ and mesh spacings $h = \lambda/10$ and $h = \lambda/20$

3. Let

$$\tilde{b} = \sum_{j=0}^{i} b_j \omega^{4j} h^{4j} \qquad \tilde{c} = \sum_{j=0}^{i} c_j \omega^{4j} h^{4j}$$

where b_i and c_i are unknown coefficients;

4. Determine b_i and c_i such that

$$\min \left(\omega^2 - \frac{\tilde{b}}{h^2} \frac{2 - 2\cos(h\omega \cos\phi_j)}{4\tilde{c} + 2\tilde{c}\cos(h\omega\cos\phi_j)} - \frac{\tilde{b}}{h^2} \frac{2 - 2\cos(h\omega \sin\phi_j)}{4\tilde{c} + 2\tilde{c}\cos(h\omega\sin\phi_j)} \right)$$

where $\phi_j = (2j\pi)/N$ with $j = 1, \cdots, K$, and $K = 20$;

5. If $i \neq N$ goto 2.

To quantify the amount of dispersion, consider the frequency $\omega = 2\pi/\lambda = 1$ and mesh spacings $h = \lambda/10$ and $h = \lambda/20$. The results obtained are displayed in Figure 12. For both mesh spacings, it can be observed that the dispersion associated with the modified edge finite element is much smaller for all angles of propagation than that associated with the standard edge finite element stencil. The usefulness of this approach remains limited due to the restriction to meshes composed only of square elements. However, numerical computations of wave propagation and electromagnetic scattering examples [68] clearly demonstrate the advantages of the approach over a standard low order finite element scheme. As an example, we show in Figure 13 results obtained when a plane wave with wavenumbers $\xi_x = \xi_y = 5$ is propagated across the unit square domain. Meshes with uniform spacings $h = 1/10, 1/12, 1/14, 1/16, 1/18, 1/20$ are considered and the results obtained for the standard and modified edge finite element stencil are compared. We observe that the dispersion is dramatically reduced when the modified edge finite element stencil is employed, so that on spacings as coarse as $h = 1/10$, which represent approximately 8 points per wavelength, the wave is well represented. Using the standard edge finite element stencil, one observes that the dispersion is large even when a mesh with spacing $h = 1/20$ is used. Incidentally,

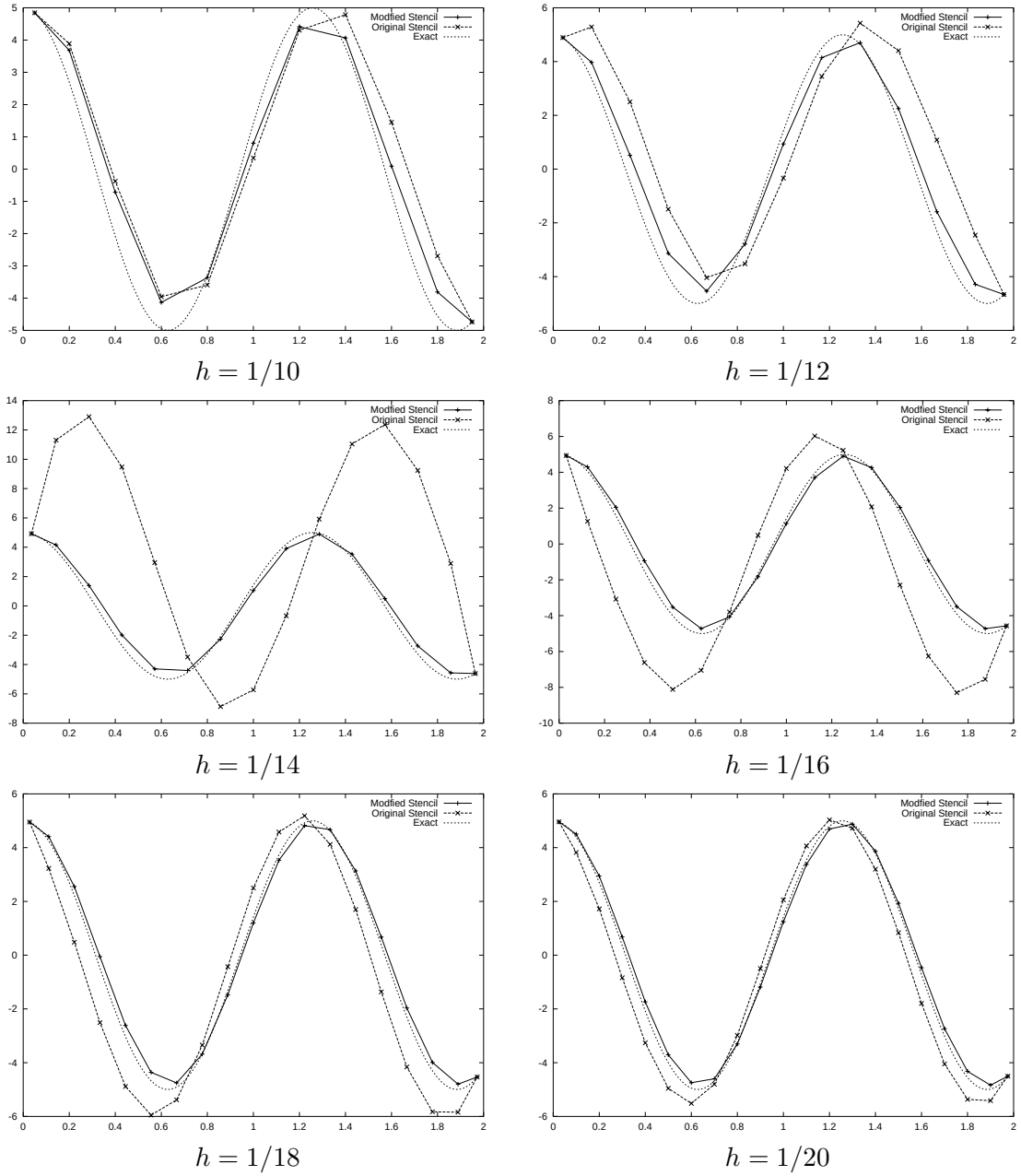

Figure 13. Comparison of the dispersive behaviour of the modified and standard edge finite element stencils for the propagation of a wave with wavenumbers $k_x = k_y = 5$ on a sequence of meshes with different spacings

this represents a spacing with approximately 18 points per wavelength. We also observe that, in the range $h = 1/10$ to $h = 1/20$, the standard edge finite element stencil is in the pre–asymmtopic region where we observe both increases and decreases in the error as the spacing is refined.

5.2 Two–Dimensional Triangular Edge Elements

Investigations of dispersion in low order order triangular elements have been carried out by Monk and Parrott [93, 94]. For a uniform mesh of right angled triangles, they obtained the result

$$\omega^2 h^2 - \left(\xi_1^2 h^2 + \xi_2^2 h^2 - \frac{\xi_1^4 h^4}{36} - \frac{\xi_1^3 \xi_2 h^4}{18} + \frac{\xi_1^2 \xi_2^2 h^4}{9} - \frac{\xi_1 \xi_2^3 h^4}{18} - \frac{\xi_2^4 h^4}{36} + \right.$$
$$\left. + \text{higher order terms} \right) = 0 \tag{104}$$

in the lowest order case, when the element has sides of length 1, 1 and $\sqrt{2}$. They were unable to produce a corresponding closed form for the dispersion relationship for a uniform mesh of equilateral triangles.

5.3 Extension to Three–Dimensions

Investigations by Cohen and Monk [40] demonstrated how discrete dispersion relationships can be obtained for mass–lumped hexahedral elements. Order $p = 0$ and $p = 1$ hexahedral elements were analysed and a range of numerical computations were presented, in which the $p = 1$ elements perform better than the $p = 0$ elements.

Ainsworth [5] derives the dispersion relationship for hexahedral elements with arbitrary order p as

$$\omega^2 - \left(\xi_x^2 + \xi_y^2 + \xi_z^2 + \right.$$
$$\left. \frac{h^{2(p+1)}}{2(p+1)+1} \left(\frac{(p+1)!}{(2(p+1))!} \right) \left(\xi_x^{2(p+1)+2} + \xi_y^{2(p+1)+2} + \xi_z^{2(p+1)+2} \right) \right) = O(h^{2(p+1)+2}) \tag{105}$$

In related work, Ainsworth also derives the dispersion relationship for the *hp*–version Galerkin discretisation of the Helmholtz equation [3] and the dispersion relationship for the discontinuous Galerkin approach [4].

By deriving suitable stencils for the $p = 0$ hexahedral element, one could also attempt an approach along the lines of that suggested in Section 5.1.1 for a mesh composed entirely of cuboid elements in three–dimensions. However, as in the two–dimensional approach already described, this restriction to cuboid elements would severely restrict the practical usefulness of the resulting procedure.

For the tetrahedral element, it is no longer possible to obtain closed form expressions for quantifying the dispersion, even if only the lowest order element is considered [90]. Instead, it is possible to perform numerical computations to determine the magnitude of the dispersion in certain cases. For example, cuboid and Somerville type meshes composed of tetrahedra have been investigated [90] and it has been observed that the dispersive behaviour is much better for the Somerville type meshes.

6 APPLICATION TO SCATTERING SIMULATIONS

The electromagnetic wave scattering problem is an interesting practical application which can benefit from the use of *hp*–finite elements [78]. In this section, we shall first summarise the necessary extensions of the theory presented in Section 2 to enable the modelling of the scattering problem. Then, we discuss the choices available for the truncation of the infinite domain which arises in the scattering problem. Following on from this, we shall include a sequence of numerical results which demonstrate the effectiveness of an approach which uses a perfectly matched layer far field boundary condition. We also describe, briefly, an adaptive procedure for improving the resolution of the scattering width. Some interesting further extensions are also discussed.

6.1 Theoretical Considerations

For scattering simulations, it is convenient to split the electric field into incident and scattered fields [79, 78] as

$$\boldsymbol{E} = \boldsymbol{E}^i + \boldsymbol{E}^s \tag{106}$$

where $\boldsymbol{E}^i$ is a known plane wave which satisfies Maxwell's equations in free space and $\boldsymbol{E}^s$ is the scattered field. It follows that

$$\text{curl}\,\left(\mu^{-1}\text{curl}\,\boldsymbol{E}^s\right) - \omega^2\epsilon\boldsymbol{E}^s = \omega^2(\epsilon - \boldsymbol{I})\boldsymbol{E}^i - \text{curl}\left\{\left(\mu^{-1} - \boldsymbol{I}\right)\text{curl}\,\boldsymbol{E}^i\right\} \tag{107}$$

where $\boldsymbol{I}$ is the identity tensor. In the absence of dielectric materials, the source term on the right hand side of this equation vanishes. For present purposes, the scatterer is assumed to be either a perfect electrical conductor (PEC) or a perfect magnetic conductor (PMC), possibly coated with a dielectric layer. In the case of a PEC, the boundary condition

$$\boldsymbol{n} \times \boldsymbol{E}^s = -\boldsymbol{n} \times \boldsymbol{E}^i \tag{108}$$

is applied on the boundary of the scatterer, Γ_{PEC} whilst, in the case of a PMC, the condition

$$\boldsymbol{n} \times \text{curl}\,\boldsymbol{E}^s = -\boldsymbol{n} \times \text{curl}\,\boldsymbol{E}^i \tag{109}$$

is imposed on Γ_{PMC}. At a dielectric interface, between materials a and b, the jump conditions

$$\boldsymbol{n} \times (\boldsymbol{E}^{sa} - \boldsymbol{E}^{sb}) = \boldsymbol{0} \tag{110}$$

$$\boldsymbol{n} \times \left(\mu_a^{-1}\text{curl}\,\boldsymbol{E}^{sa} - \mu_b^{-1}\text{curl}\,\boldsymbol{E}^{sb}\right) = -\boldsymbol{n} \times \left(\mu_a^{-1} - \mu_b^{-1}\right)\text{curl}\,\boldsymbol{E}^i \tag{111}$$

should be fulfilled

In addition, as the scattering problem is generally posed in an open domain, these conditions must be supplemented with a suitable radiation condition. The relevant condition here is that the scattered electric field should satisfy the Silver–Müller radiation condition

$$\lim_{r\to\infty} (\boldsymbol{r} \times \text{curl}\boldsymbol{E}^s - \mathrm{i}\omega\boldsymbol{E}^s) = 0 \tag{112}$$

In numerical simulations, this condition must be suitably approximated and, in the following section, we discuss a number of possible alternative approaches.

Multiplying equation (107) by a suitable vector weighting function, and integrating over the domain using integrating by parts, leads to the weak variational statement of the scattering problem: find $\boldsymbol{E}^s \in X_D$ such that

$$(\mu^{-1}\text{curl}\,\boldsymbol{E}^s, \text{curl}\,\boldsymbol{W})_\Omega - \omega^2(\epsilon\boldsymbol{E}^s, \boldsymbol{W})_\Omega = \ell(\boldsymbol{W}) \qquad \forall \boldsymbol{W} \in X_0 \tag{113}$$

The spaces employed are defined as

$$X_D = \{\boldsymbol{v} \in \boldsymbol{H}(\text{curl}), \boldsymbol{n} \times \boldsymbol{v} = -\boldsymbol{n} \wedge \boldsymbol{E}^i \text{on}\ \Gamma_{PEC}\} \tag{114}$$

$$X_0 = \{\boldsymbol{v} \in \boldsymbol{H}(\text{curl}), \boldsymbol{n} \times \boldsymbol{v} = \boldsymbol{0}\ \text{on}\ \Gamma_{PEC}\} \tag{115}$$

while

$$\ell(\boldsymbol{W}) = \int_{\Gamma_{PMC}} \boldsymbol{n} \wedge \mathrm{curl}\boldsymbol{E}^i \cdot \overline{\boldsymbol{W}} \mathrm{d}\Gamma \\ -((\mu^{-1} - \boldsymbol{I})\boldsymbol{E}^i, \boldsymbol{W})_{\Omega_d} + \omega^2((\epsilon - \boldsymbol{I})\boldsymbol{E}^i, \boldsymbol{W})_{\Omega_d} \tag{116}$$

is a linear form. The end goal is to approximate the scattering width, or radar cross section per unit length, distribution which in the two–dimensional case is given by

$$\chi(\phi) = \lim_{r\to\infty} 2\pi r \frac{|H_z^s|^2}{|H_z^i|^2} \tag{117}$$

for plane incident waves of the form

$$\boldsymbol{E}^i = \begin{pmatrix} -\sin\theta \\ \cos\theta \end{pmatrix} \exp\{\mathrm{i}\omega(x\cos\theta + y\sin\theta)\} \tag{118}$$

with specified incidence direction θ. Note that in this case $|H_z^i| = |\mathrm{curl}\,\boldsymbol{E}^i| = 1$

6.2 Alternative Far Field Boundary Conditions

Sufficiently far from the obstacle, the radiation condition requires that the electric field components consist of outgoing waves only. Much attention has been devoted to the problem of developing a suitable approximation, as conditions of this type are always encountered in the simulation of wave propagation problems set on infinite domains. There exist a number of alternatives for satisfying this requirement,including absorbing boundary conditions [22], infinite elements [24, 37], the Dirchlet to Neumann map [56], coupling with boundary elements [64] and the use of a perfectly matched layer (PML) [23]. In this article we do not intend to give an extensive review of all these approaches, as this can be found in many other places, e.g. the book by Cohen [41]. We will assume that the boundary has been truncated using a PML, due to the ease of implementation and previous successes with this approach [79, 83, 78]. For simplicity, we shall consider only two–dimensional domains, though three–dimensional extensions have also been reported [80].

6.3 Scattering Simulations Using a PML

In practical applications, perfectly matched layers are normally assumed to be either rectangular or convex (mainly circular) curvilinear domains. For simplicity, we consider the case of the anisotropic rectangular PML, which just consists of modifications to the material parameters inside the PML region and is, therefore, simple to implement. Corresponding curvilinear PML formulations are also possible [79, 78].

Within the PML layer, modified material parameters are employed to absorb the outgoing scattered wave with minimum reflection. Specifically, we define

$$\mu = d_1 d_2 \qquad \epsilon = \begin{pmatrix} d_2/d_1 & 0 \\ 0 & d_1/d_2 \end{pmatrix} \tag{119}$$

in Ω_{pml} where $d_j = 1 - \mathrm{i}\sigma_j(x_j)/\omega$ [92]. A quadratic profile is used for the grading of σ_j, so that $\sigma_j = \sigma(e_j/t)^2$ where e_j is the distance measured from the PML/free space interface to a point within the PML in a given coordinate direction x_j and t is the PML thickness. Cohen [41] proposes the values $t = 1\lambda$ and $\sigma = 6$. Typically, on the external boundary Γ_{EXT} of the truncated domain, the tangential component of the electric field is set to zero.

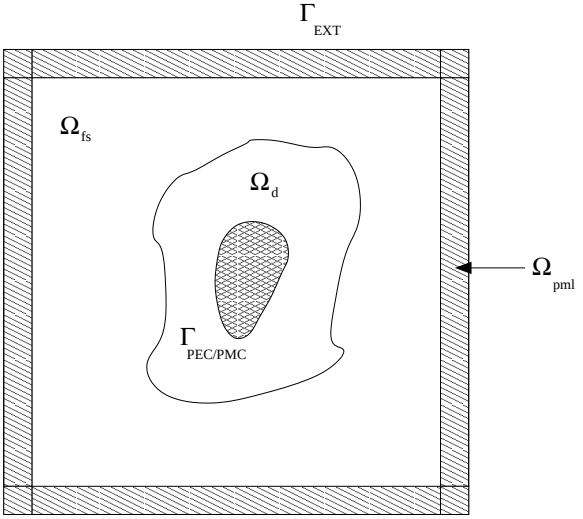

Figure 14. The domain of a scattering problem when truncated using a rectangular PML

As shown in Figure 14, the domain Ω is now made up of Ω_d, the dielectric region with appropriate values for ϵ and μ, the free space region Ω_{fs} with $\mu = \epsilon = \boldsymbol{I}$ and the PML region Ω_{pml} where the material parameters vary according to the equation (119). An approximate weak variational statement for this problem is: find $\boldsymbol{E}_H^s \in \tilde{X}_D^H$ such that

$$(\mu^{-1}\text{curl}\,\boldsymbol{E}_H^s, \text{curl}\,\boldsymbol{W}_H)_\Omega - \omega^2(\epsilon\boldsymbol{E}_H^s, \boldsymbol{W}_H)_\Omega = \ell(\boldsymbol{W}_H) \qquad \forall \boldsymbol{W}_H \in \tilde{X}_0^H \tag{120}$$

The discrete spaces are such that $\tilde{X}_D^H \subset \tilde{X}_D$ and $\tilde{X}_0^H \subset \tilde{X}_0$, and the corresponding continuous spaces containing the PML approximation are defined as

$$\tilde{X}_D = \{\boldsymbol{v} \in \boldsymbol{H}^{(2)}(\text{curl}), \boldsymbol{n} \times \boldsymbol{v} = -\boldsymbol{n} \times \boldsymbol{E}^i \text{ on } \Gamma_{PEC}, \boldsymbol{n} \times \boldsymbol{v} = \boldsymbol{0} \text{ on } \Gamma_{EXT}\} \tag{121}$$

$$\tilde{X}_0 = \{\boldsymbol{v} \in \boldsymbol{H}^{(2)}(\text{curl}), \boldsymbol{n} \times \boldsymbol{v} = \boldsymbol{0} \text{ on } \Gamma_{PEC}, \boldsymbol{n} \times \boldsymbol{v} = \boldsymbol{0} \text{ on } \Gamma_{EXT}\} \tag{122}$$

Note that the source term will only appear in the dielectric, as the PML is modelled as a non–physical extension to the Maxwell problem and, therefore, has no source term. An approximate solution $\boldsymbol{E}_H^s$ is obtained by using an edge element discretisation in this variational statement. We will demonstrate the results which are obtained when the arbitrary order hybrid discretisation given in Section 4 is employed.

Following the finite element solution procedure, the scattering width may be obtained. This is computed, by performing a near to far field transformation, as

$$\chi_H(\phi) = \frac{\omega}{4}\left|\int_{\Gamma_c} \boldsymbol{n} \times \boldsymbol{E}_H^s \cdot \boldsymbol{V} + \boldsymbol{n} \times \text{curl}\,\boldsymbol{E}_H^s \cdot \boldsymbol{Y}\,\text{d}\Gamma'\right|^2 \tag{123}$$

where Γ_c is a collection surface, which is chosen to completely surround the scatterer. The value of the scattering width, measured in decibels, is given by $10\log(\chi(\phi))$. The vectors $\boldsymbol{V}$ and $\boldsymbol{Y}$ are functions of the viewing angle ϕ and are defined as

$$\boldsymbol{V} = \begin{pmatrix} 0 \\ 0 \\ -1 \end{pmatrix} \exp\{\text{i}\omega(x'\cos\phi + y'\sin\phi)\} \tag{124}$$

$$\boldsymbol{Y} = \frac{1}{\mathrm{i}\omega} \begin{pmatrix} \sin\phi \\ -\cos\phi \\ 0 \end{pmatrix} \exp\left\{\mathrm{i}\omega(x'\cos\phi + y'\sin\phi)\right\} \tag{125}$$

It is important that the flux term $\boldsymbol{n}\times\mathrm{curl}\,\boldsymbol{E}_H^s$ is calculated carefully, otherwise accuracy may be lost in the computation of the scattering width. To this end, we employ the technique proposed by Monk [95, 91], who suggests using the variational statement to approximate the flux term. In this case, it is convenient to rewrite the scattering width as [78, 83]

$$\chi_H(\phi) = \frac{\omega}{4}\mathcal{L}^o(\boldsymbol{E}_H;\phi)\overline{\mathcal{L}^o(\boldsymbol{E}_H;\phi)} \tag{126}$$

where the functional $\mathcal{L}^o(\boldsymbol{E}_H;\phi)$ is defined as

$$\mathcal{L}^o(\boldsymbol{E}_H;\phi) = \int_{\Gamma_c} \boldsymbol{n}\times\boldsymbol{E}_H\cdot\boldsymbol{V}\,\mathrm{d}\Gamma + \sum\int_k \left(\omega^2\boldsymbol{E}_H\cdot\boldsymbol{Y}_H - \mathrm{curl}\,\boldsymbol{E}_H\cdot\mathrm{curl}\,\boldsymbol{Y}_H\right)\mathrm{d}\Omega' \tag{127}$$

Here, the summation extends over all elements $k\in\Omega$ such that $\partial k\cup\Gamma_c\neq\emptyset$ and $\boldsymbol{Y}_H$ is the $\boldsymbol{H}^{(2)}(\mathrm{curl})$ interpolant of $\boldsymbol{Y}$. When the results of numerical simulations are presented it is the quantity

$$RCS = 10\log_{10}\chi_H \tag{128}$$

that will be plotted. In this way, the scattering width is expressed in decibels and provides a meaningful description of the far field scattering from the object.

6.4 Numerical Experiments

We present a selection of numerical experiments that demonstrate the capabilities of the basic scheme.

The scattering of a plane wave by circular cylinder of electrical length 2λ is a simple example for which an exact analytical solution is available to check the accuracy of the computed results. We consider a sequence of 4 hybrid meshes, with different numbers of quadrilateral and triangular elements. The first mesh is composed of 320 quadrilaterals, the second mesh has 640 triangles, the third mesh has 160 triangles and 240 quadrilaterals and the fourth mesh has 320 triangles and 160 quadrilaterals. Figure 15 depicts the four meshes.

The cylinder is considered to be either a PEC or a PMC. In each case, the polynomial order is increased on the different meshes until converged solutions are obtained. Here, convergence was regarded as being achieved when the differences in the scattering width output in successive computations became sufficiently small. Further details of the problem set up and the PML can be found in [78]. In all cases, convergence was obtained with order $p = 4$ elements. The scattering width distributions obtained for the PEC case are compared in Figure 16.

It can be observed that, on this scale, the scattering width distributions computed on all four meshes are indistinguishable from the exact. This implies that meshes comprising of quadrilateral or triangles or hybrid combinations are equally successful at predicting the correct scattering width distribution for this problem. In addition, we note that, for hybrid meshes, the location of the interface between the triangular and quadrilateral elements does not effect the quality of the solution. The corresponding comparison for the PMC problem is shown in Figure 17 and, again, the agreement obtained on this scale, between the converged numerical solution on each of the meshes and the exact distribution, is excellent.

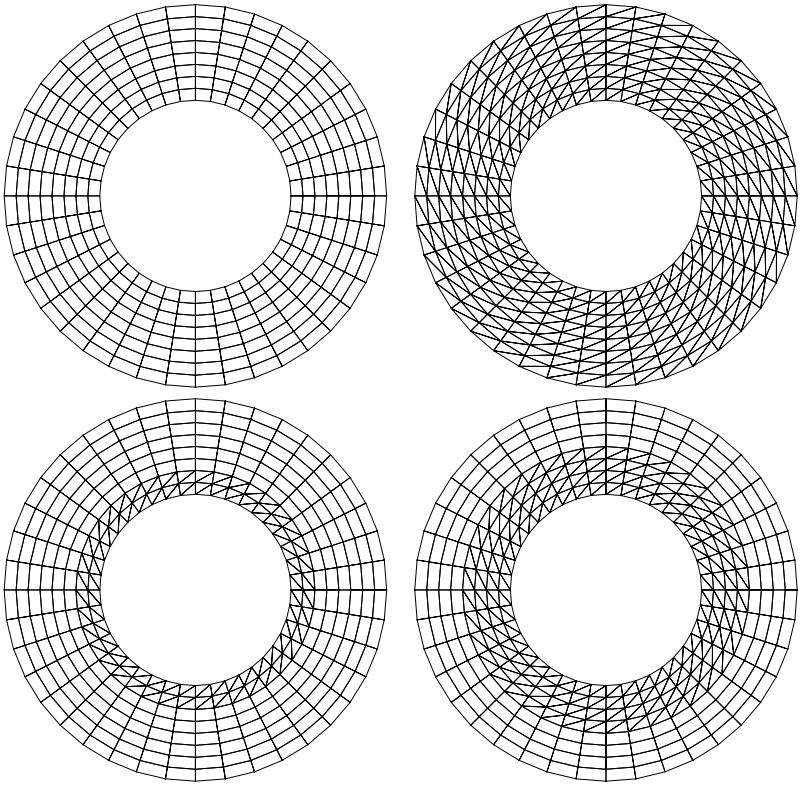

Figure 15. Simulation of scattering of a plane wave by a circular cylinder of electrical length 2λ showing 4 hybrid meshes with 320,0,240,160 quadrilaterals and 0,640,160,320 triangles, respectively

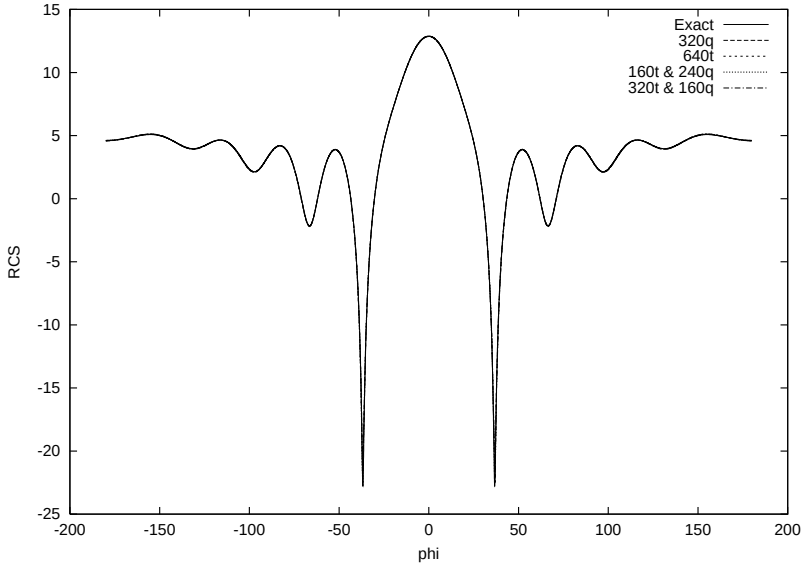

Figure 16. Scattering of a plane wave by a PEC circular cylinder of electrical length 2λ: comparison between the exact distribution and the results obtained with a PML far field boundary condition

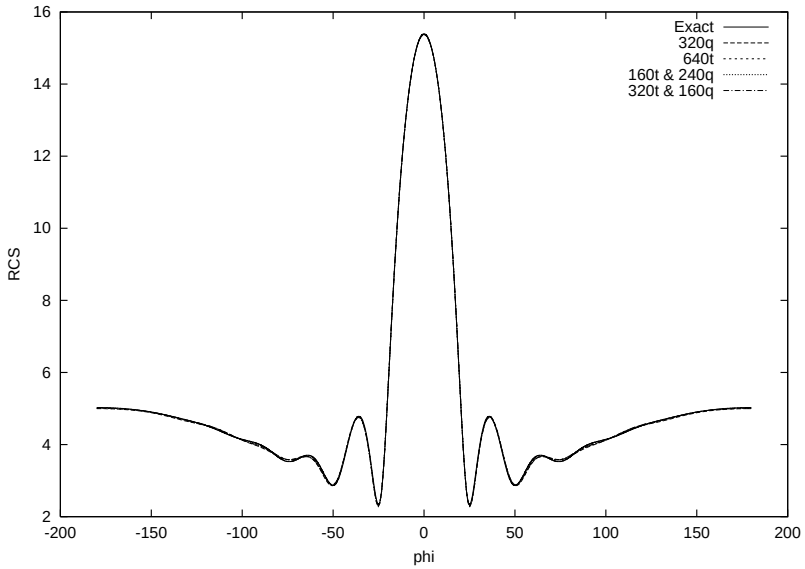

Figure 17. Scattering of a plane wave by a PMC circular cylinder of electrical length 2λ: comparison between the exact distribution and the results obtained with a PML far field boundary condition

For the next numerical example, we consider the case of a conducting cylinder with a dielectric coating. The diameter of the cylinder is chosen to be 15λ and the thickness of the coating 1.875λ. The dielectric is defined in terms of the constants

$$\epsilon_d = 2.56 \qquad \mu_d = 1 \tag{129}$$

To represent the computational domain, a structured hybrid mesh of 800 triangles and 600 quadrilaterals is generated, as shown in Figure 18. The mesh is the form of a circular annulus with inner radius 7.5λ and outer radius 16.875λ. Here, the triangles occupy the region $7.5\lambda \leq r \leq 11.25\lambda$ and the quadrilaterals occupy the region $11.25\lambda \leq r \leq 16.875\lambda$. The dielectric coating is discretised by triangular elements, the free space is discretised by combination of quadrilaterals and triangular elements. The PML layer occupies the region $16.125\lambda \leq r \leq 16.875\lambda$ of the quadrilateral elements.

The scattering width distribution, for a PEC cylinder when $p = 7$ elements are employed uniformly over the mesh, is presented in Figure 19. Here, it can be observed that, on this scale, the scattering width distribution produced by the finite element solution is indistinguishable from the exact. The corresponding scattering width distribution for the scattering of a wave by a PMC cylinder is given in Figure 20. Once again the agreement observed between the finite element solution and the exact solution is excellent.

As an illustration of the predictive capability of the method, consider scattering by a PEC semi–open cavity. For this example, no analytical solution is available. Geometrically, the perfectly conducting semi–open cavity consists of two parallel walls which are connected at their right hand end. This produces a cavity in the shape of a letter U rotated through 90 degrees. The thickness of the walls is denoted by d and the outer dimensions are given by $b + d$ in the x direction and $c + 2d$ in the y direction. The implication is that the inner cavity has dimensions b and c. We consider the particular cavity which is defined by $d = 0.4\lambda = 0.2$, $b = 8\lambda = 4$ and $c = 2\lambda = 1$. An advancing front procedure [106] is employed to generate an unstructured mesh of triangles. A structured mesh of quadrilaterals is then attached to the outer surface of the triangulated region and is terminated at the desired

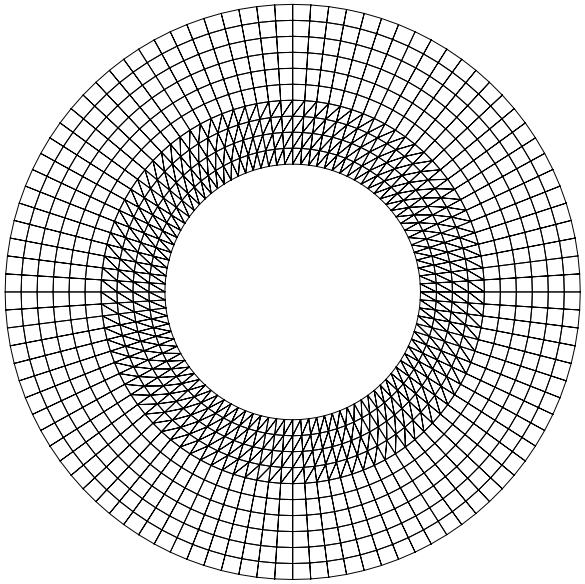

Figure 18. Scattering by a coated circular cylinder of electrical length 15λ: a structured hybrid mesh consisting of 800 triangles and 600 quadrilaterals

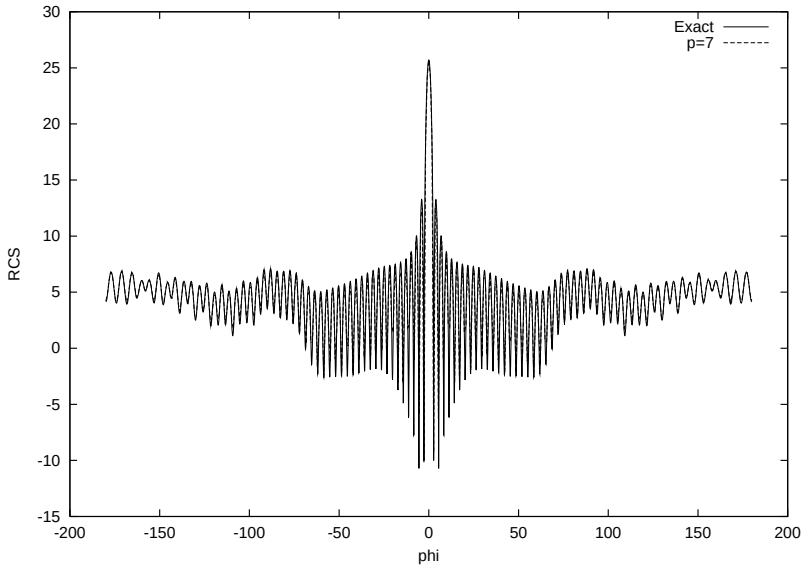

Figure 19. Scattering of a wave by a coated PEC circular cylinder of electrical length 15λ: comparison between the exact distribution and the results obtained from a PML boundary condition

distance from the scatterer. The PML lies within this structured mesh region. The mesh is shown in Figure 21. The order is increased uniformly across the mesh until a converged solution is reached, with $p = 8$ elements. The contour plots are shown in Figure 22 and the RCS distribution in Figure 23.

Further numerical examples can be found in [78, 79].

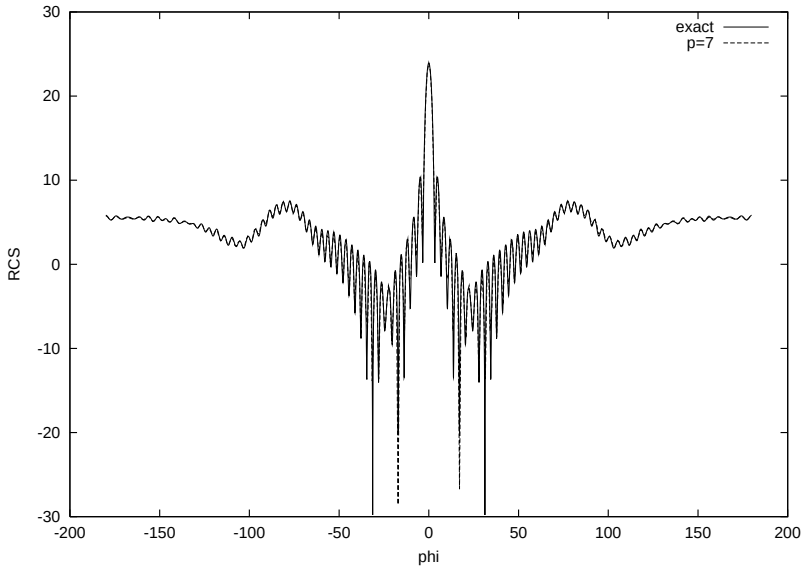

Figure 20. Scattering of a wave by a coated PMC circular cylinder of electrical length 15λ: comparison between the exact distribution and the results obtained from a PML boundary condition

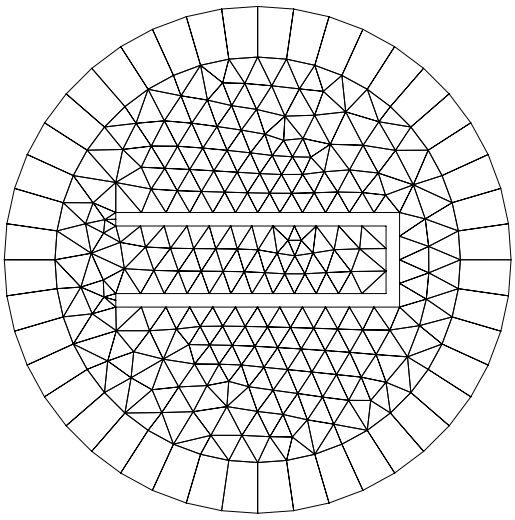

Figure 21. Scattering by semi–open cavity: a hybrid mesh consisting of 407 triangles and 44 quadrilaterals

6.5 Error Estimation and Adaptivity

The topic of error estimation and adaptivity is a huge area of research and we do not attempt to give a comprehensive overview. A full discussion of this topic can be found in the monograph of Ainsworth and Oden [11]. Error estimation and adaptivity for electromagnetic scattering problems is not easily accomplished. One of the main difficulties which arise is that the use of standard local error indicators, which suggest where to refine a discretisation, may not necessarily reduce the error in a scattering computation. This is due to the dispersion effects mentioned in Section 5. But, provided the effects of dispersion are

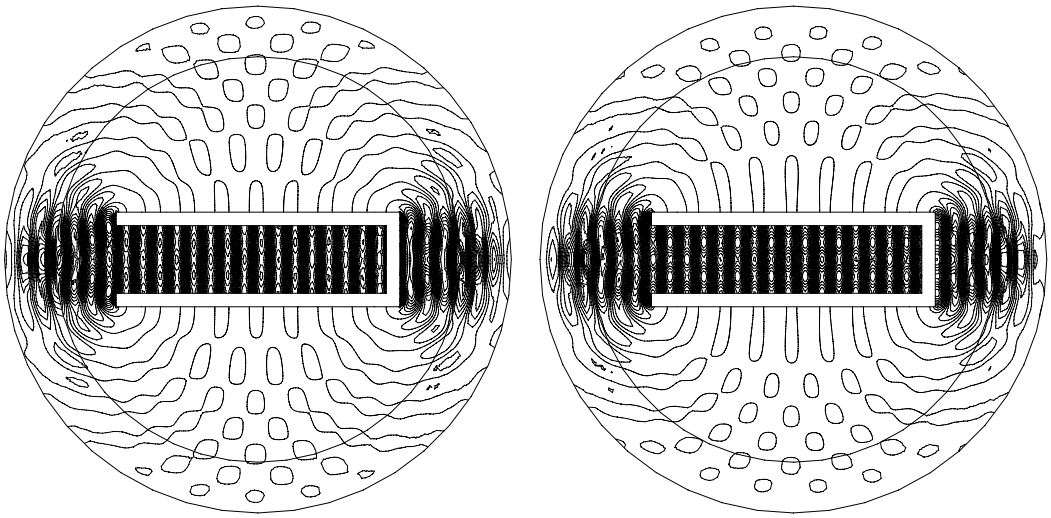

Figure 22. Scattering of a plane wave by a PEC semi–open cavity: contours of (a) $Re(H_z^s)$ and (b) $Im(H_z^s)$

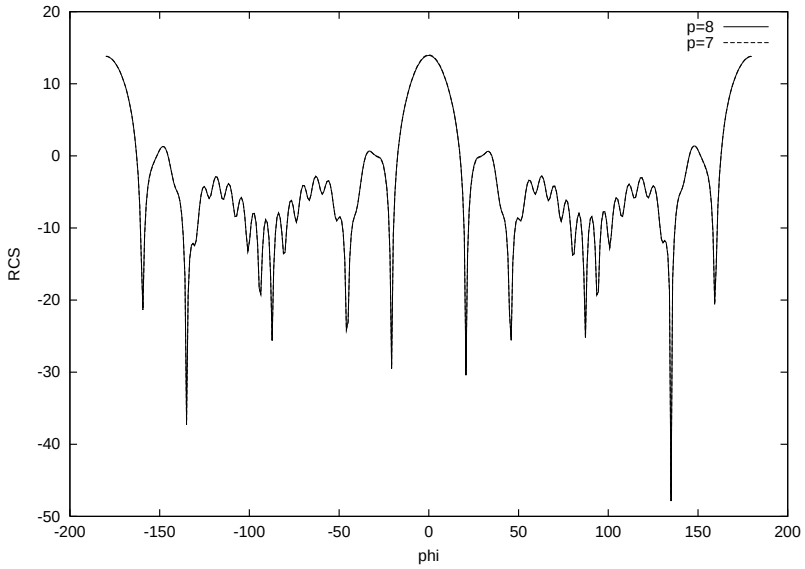

Figure 23. Scattering of a plane wave by a PEC semi–open cavity: convergence of the numerical solution for an incident wave propagated along the x axis

overcome, outputs computed from solutions obtained on discretisations with a sufficiently high p, and small enough mesh spacing h, will be indistinguishable from the exact. However, such solutions can be expensive to compute. It is, therefore, important to be able to evaluate strict upper and lower bounds for specified outputs, such as the scattering width $\chi(\boldsymbol{E}_h^s, \phi)$ on a fine discretisation, in the form

$$\chi^-(\boldsymbol{E}_H^s, \phi) \leq \chi(\boldsymbol{E}_h^s, \phi) \leq \chi^+(\boldsymbol{E}_H^s, \phi) \tag{130}$$

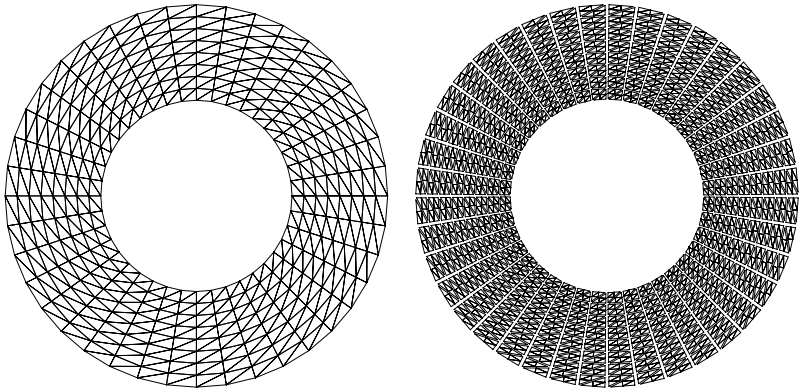

Figure 24. Illustration of (*a*) a typical working mesh and (*b*) a typical broken truth mesh used for the error estimation process in *h*–refinement mode

A method of achieving this has been presented [78, 83] and is an extension of the procedure first proposed by the group of Patera and Peraire [103, 88, 105, 111, 104]. It involves the selection of a truth discretisation, constructed as a refinement of the working discretisation used in the normal finite element analysis. The truth discretisation is selected to be much finer and the error estimation is based on the ansatz that on this discretisation the solution is indistinguishable from the true solution. A typical working and broken truth discretisation for the scattering problem is shown in Figure 24. The error estimation procedure requires the solution of a local problem inside each working mesh element. These computations are trivially parallel. In previous work, only the lowest order H^1 conforming triangular elements had been employed, whereas the extension to electromagnetic scattering simulations uses Ainsworth and Coyle's arbitrary order $\boldsymbol{H}^{(2)}(\mathrm{curl})$ conforming elements. The implementation on higher order elements was made possible using the edge fluxes, proposed by Demkowicz [48], which balance the solution between the broken elements.

The selected output is the value of the scattering width at a selected viewing angle and an adaptive procedure was subsequently derived based on adjoint calculations using the linearised functional $\mathcal{L}^o(\boldsymbol{E}_H;\phi)\overline{\mathcal{L}^o(\boldsymbol{w};\phi)} + \overline{\mathcal{L}^o(\boldsymbol{E}_H;\phi)}\mathcal{L}^o(\boldsymbol{w};\phi)$. To ensure that the initial adaptive steps lead to reductions in the error, the initial discretisation is generated in such a way that the dispersion can already be ensured to be at an acceptable level. This was accomplished using the dispersion relationship of Ainsworth and Coyle that was presented in Section 5.

As an example, consider the scattering of a plane wave by a PMC 16λ cavity. The geometry of this cavity consists of a circular cylindrical PEC wall of zero thickness, with an aperture of 20 degrees. For this case, Figure 25 shows the convergence of the relative bound gap. The truth discretisation for this problem is selected as a mesh with the same spacing as the working discretisation but with order $p = 14$ elements. When an adaptive p strategy is initiated on a coarse discretisation, the convergence behaviour is very erratic and is characterised by wild increases and decreases in the size of the bound gap. After 15 adaptive steps, no convergence is obtained and this adaptive strategy is stopped. When uniform increments in p are adopted, the solution convergence is uniform throughout. Following an adaptive p strategy, which uses the dispersion relationship to obtain an initial distribution of $p = 10$ elements, we observe that the solutions produced require less unknowns than the uniform p strategy. Therefore, for large electrical lengths, it is essential that the dispersion

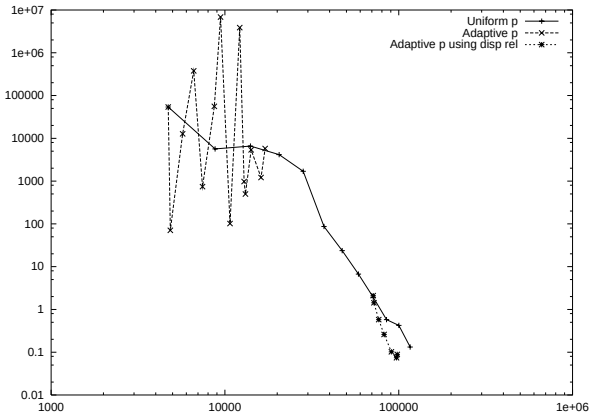

Figure 25. Scattering of a plane wave by a PMC cylindrical cavity of electrical length 16λ: the convergence of the relative bound gap $(\chi^+ - \chi^-)/\chi_h$ with number of unknowns for $\phi = 0$ when uniform and adaptive p–refinement strategies are employed

relationship is used to create a meaningful starting point for the adaptive procedure. To complete the 16λ example we show the contours of $Re(E_z^s)$ and $Im(E_z^s)$ and plot the distribution of the RCS in Figure 26. Further numerical examples can be found in [78, 83]. An extension of this approach which provides bounds for the complete range of viewing angles was presented in [82].

Rachowicz and Zdunek [108] have recently presented three different approaches to the problem of error estimation for electromagnetic scattering problems in three–dimensions. The approaches include implicit and explicit error estimation procedures and a goal orientated error estimator, along similar lines to the method described above. Their numerical examples demonstrate the performance of the implicit and goal orientated error estimator for scattering by a PEC sphere and a cube.

6.6 Interesting Extensions to the Scattering Problem

6.6.1 Reduced order model

The analysis of the basic scattering problem may be extended through the use of an adjoint enhanced reduced order model [84], which allows the rapid computation of scattering width distribution for new incident wave directions. This is important when one imagines the engineer who wishes to investigate a certain design, under the influence of different conditions, in a short amount of time. This procedure may be separated in to two parts. In the first off–line stage, data is computed and stored. This involves

1. Selection of a parameter space of incident directions $\{\theta_i, i = 1, \cdots, N_\theta\}$;

2. Computation of primal scattering solutions $\boldsymbol{E}_H^s(\theta_i)$ for each θ_i of the parameter space of incident directions;

3. Selection of a parameter space of viewing angles $\{\phi_i, i = 1, \cdots, N_\phi\}$;

4. Computation of adjoint solutions $\boldsymbol{\Psi}_H(\phi_i)$ for each ϕ_i of the parameter space of viewing angles.

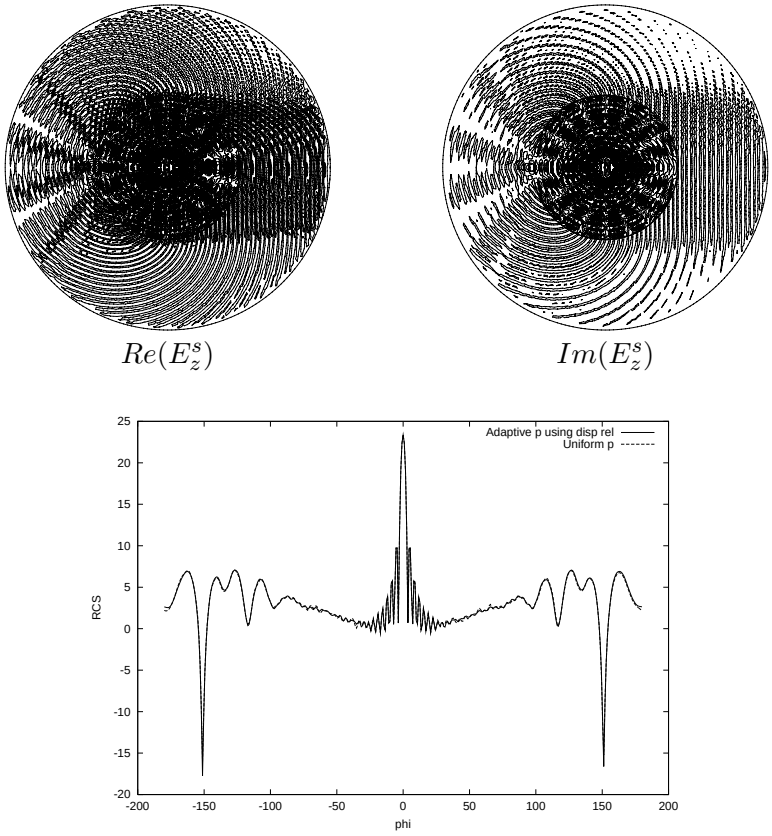

Figure 26. Scattering of a plane wave by a PMC cylindrical cavity of electrical length 16λ: contours of $Re(E_z^s)$ and $Im(E_z^s)$ and the computed distribution of RCS for the converged solution

The right hand side used for the adjoint problem in the case of the reduced order model is $\mathcal{L}^o(\boldsymbol{w}_H;\phi)$, and not the linearised functional that was used previously in the error–bounding procedure [78, 83]. This is a better choice for the reduced order model as the inter–dependence of the primal solution $\boldsymbol{E}_H^s$ that occurs for the linearised functional is eliminated. We define

$$W_{N_\theta} = \text{span}\{\boldsymbol{E}_H^s(\theta_i); i = 1, \cdots N_\theta\} \qquad W_{N_\phi} = \text{span}\{\boldsymbol{\Psi}_H(\phi_i); i = 1, \cdots N_\phi\} \quad (131)$$

The second on–line stage uses the stored data and requires

1. Selection of a new incident direction θ;
2. Computation of an approximate solution $\tilde{\boldsymbol{E}}_H^s \in W_{N_\theta}$, using the solutions in W_{N_θ} as basis;
3. Computation of an approximate adjoint solution $\tilde{\boldsymbol{\Psi}}_H \in W_{N_\phi}$, using the solutions in W_{N_ϕ} as basis;
4. Calculation of an adjoint enhanced output for the scattering width;
5. Computation of error bounds.

Error certainty bounds ensure that the computed reduced order model approximations are indeed accurate. The bounds can be computed at little extra computational cost. As a numerical example, consider the scattering of a plane wave by a PMC cylinder of electrical length 2λ. Solutions in an off–line stage are precomputed at a specified set of incident wave directions, together with a set of related adjoint problems. Then, in the on–line stage, for a given new incident wave direction, the scattering width is rapidly predicted, together with associated certainty bounds. The results obtained for incident wave directions $\theta = 0$ and $\theta = 10$ degrees are shown in Figure 27. In this figure, we observe that when the incident wave direction is one of the set of incident wave directions for the original primal problem, the certainty bounds vanish, as expected ($\theta = 0$). For the case $\theta = 10$ degrees, which represents a wave direction which is not one of the primal problems, we observe that certainty bounds are obtained which only vanish at viewing angles corresponding to adjoint solutions of the dual problem. Note that the adjoint enhanced reduced order model produces an accurate representation of the output and has the advantage of added certainty provided by the bounds.

6.6.2 Modified finite element stencil

As an alternative to the arbitrary order $\boldsymbol{H}(\text{curl})$ conforming scheme, an approach based on the modified finite element stencil proposed in Section 5 could be employed. Using this approach, the wave may be represented with less points compared to the standard stencil. However, the modified stencil lacks the versatility of the arbitrary order scheme, as it is limited to very simple rectangular geometries and it is unclear how well singularities are represented. Some initial computations in this direction have already been presented [68].

6.6.3 Plane wave basis

Another interesting development involves the use of special plane wave $\boldsymbol{H}(\text{curl})$ conforming elements. Success has previously been obtained by the group of Bettess and his co–workers [77, 76, 25] in the development of H^1 conforming basis functions, incorporating plane wave direction expansion functions for the solution of scattering problems based on the Helmholtz Equation. Initial extensions to the solution of Maxwell's Equations appear promising [81]. In this work, the new approximation is obtained by multiplying the lowest order edge basis functions by plane wave expansions so that, in the case of quadrilateral elements, the new approximation is given by

$$\boldsymbol{E}_H = \sum_{i=1}^{4} \sum_{m=1}^{M} \boldsymbol{\phi}_0^i \exp\left\{\mathrm{i}\omega(x\cos\theta_m + y\sin\theta_m)\right\} \tag{132}$$

where M is the number of directions of plane waves. Using this approximations means that we assume that, on each edge, the tangential component of the electric field can be expressed as a linear combination of M plane waves. Generally, the directions of the plane waves are assumed to be equally spaced so that $\theta_m = 2\pi m/M$. As an illustration of the capabilities of the approach, we show a numerical example consisting of scattering by an L–shape domain. The problem we consider has the analytical solution

$$\boldsymbol{E} = \begin{pmatrix} \frac{\partial f}{\partial y} \\ -\frac{\partial f}{\partial x} \end{pmatrix} \qquad f = J_\alpha(\omega r)\cos(\alpha\theta) \tag{133}$$

where (r, θ) are the polar cylindrical coordinates and J_α is the Besel function. We assume that $\alpha = 0$, so the solution is smooth. We fix a mesh of 3 quadrilateral elements and increase the number of plane wave directions M and observe the convergence behaviour for

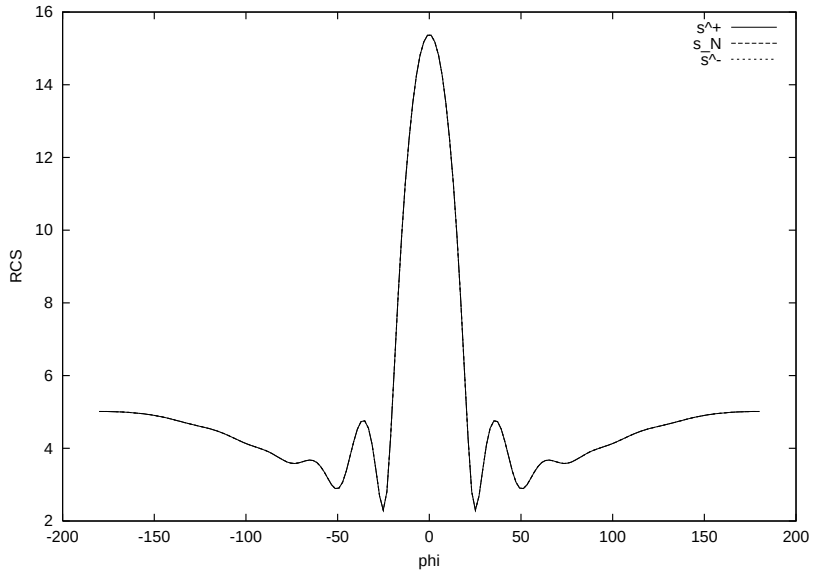

$\theta = 0$

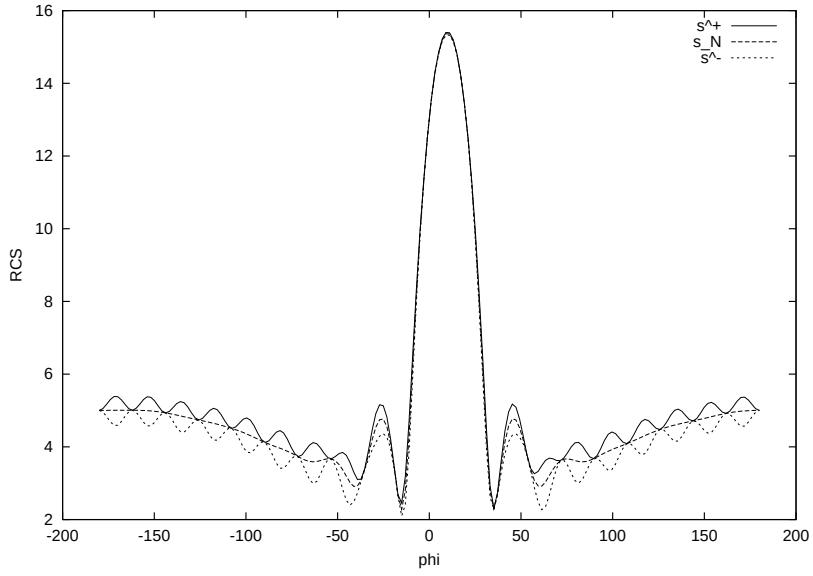

$\theta = 10$

Figure 27. Scattering of a plane TE wave by a PMC cylinder of electrical length 2λ showing the upper and lower certainty bounds and the predicted scattering width distributions for the reduced–order model at different angles, θ

frequencies $\omega = 5, 10$ and 20. The results of this investigation are shown in Figure 28. We observe that, once the number of plane directions becomes sufficiently large, the error in the $\boldsymbol{H}(\text{curl})$ norm becomes small. The contours of the computed solutions are shown in Figure 29.

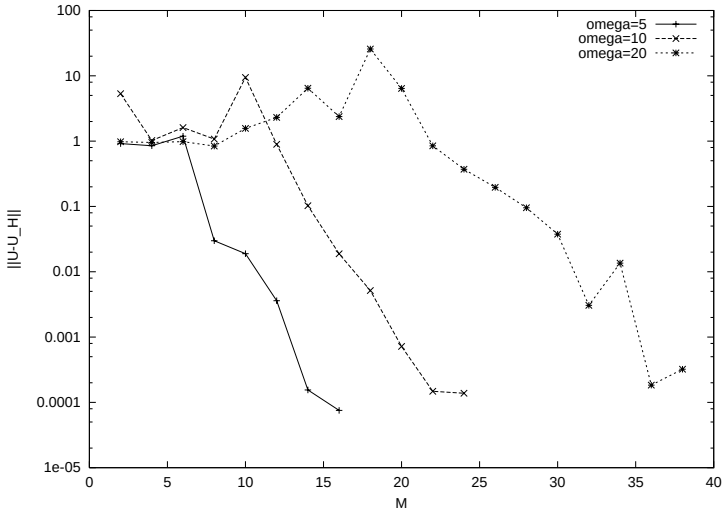

Figure 28. Scattering in an L–shaped domain for $\alpha = 0$ and varying ω discretised by quadrilateral plane wave basis elements, showing the convergence of $\|\boldsymbol{E} - \boldsymbol{E}_H\|_{\boldsymbol{H}(\mathrm{curl})}$ with increasing number of plane wave directions M

7 APPLICATIONS TO EIGENVALUE CALCULATION

In this section, we consider the solution of Maxwell bounded cavity problems by the hierarchical edge element discretisation presented in Section 4. The solution of the Maxwell cavity problem involves the computation of the nonzero resonant frequencies $\omega^2 \setminus \{0\}$, and the associated electric field $\boldsymbol{E}$, of the problem

$$\begin{aligned} \mathrm{curl}\,\mu^{-1}\mathrm{curl}\boldsymbol{E} - \omega^2\epsilon\boldsymbol{E} &= \boldsymbol{0} \qquad \text{in } \Omega & (134)\\ \boldsymbol{n}\wedge\boldsymbol{E} &= \boldsymbol{0} \qquad \text{on } \partial\Omega & (135)\end{aligned}$$

There is often much debate in the literature about whether or not it is also necessary to specify the divergence condition $\mathrm{div}\,\boldsymbol{E} = 0$ in addition to the above equations. This is, indeed, associated with the requirement that we consider only non–zero frequencies. Theoretically, one should always include a Lagrange multiplier, as proposed by Kikuchi [74] and discussed in Section 2. This would result in the variational problem: find $\boldsymbol{E} \in \boldsymbol{H}_0(\mathrm{curl})$, $p \in H^1_0$ and $\omega^2 \in \mathbb{R}$ such that

$$\begin{aligned} (\mu^{-1}\mathrm{curl}\,\boldsymbol{E}, \mathrm{curl}\,\boldsymbol{W})_\Omega - \omega^2(\epsilon(\boldsymbol{E}+\nabla p), \boldsymbol{W})_\Omega &= 0 \qquad \forall \boldsymbol{W} \in \boldsymbol{H}_0(\mathrm{curl}) & (136)\\ -\omega^2(\epsilon\boldsymbol{E}, \nabla q)_\Omega &= 0 \qquad \forall q \in H^1_0(\Omega) & (137)\end{aligned}$$

However, for some time within the engineering community this problem was thought to be adequately resolved by solving the problem: find $\boldsymbol{E} \in \boldsymbol{H}_0(\mathrm{curl})$ and $\omega^2 \in \mathbb{R}$ such that

$$(\mu^{-1}\mathrm{curl}\,\boldsymbol{E}, \mathrm{curl}\,\boldsymbol{W})_\Omega - \omega^2(\epsilon\boldsymbol{E}, \boldsymbol{W})_\Omega = 0 \qquad \forall \boldsymbol{W} \in \boldsymbol{H}_0(\mathrm{curl}) \tag{138}$$

and employing a discretisation consisting of the lowest order edge, or Whitney [128], elements, as they are divergence–free [39, 32]. For example, Chatterjee *et al.* [39] present results for computing the eigenmodes of three–dimensional cavities, filled with free space and dielectric materials, using the lowest order tetrahedral basis functions. The higher order basis functions, however, are not divergence–free and, more recently, it has become clear

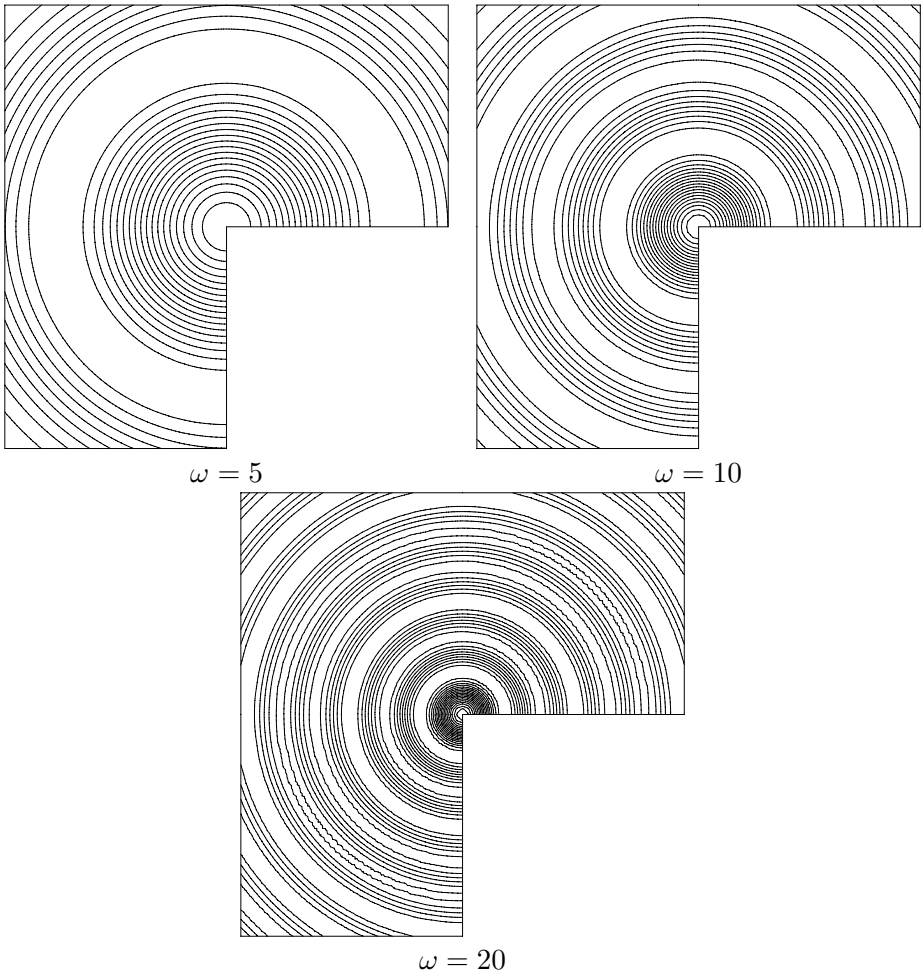

Figure 29. Scattering in an L–shaped domain for $\alpha = 0$ and varying ω discretised by quadrilateral plane wave basis edge elements, showing the contours of the computed field $\operatorname{curl} \boldsymbol{E}_H$

that enforcing this property in the weak formulation, as well as employing a set of basis functions that are $\boldsymbol{H}(\mathrm{curl})$–conforming, leads to a method that is not plagued by unwanted solutions [122]. Boffi *et al.* [28] provides a detailed discussion of these issues. In fact, it has been argued [74] that the Lagrange multiplier should also be included when the lowest order basis functions are employed. An alternative method is utilised in Wang, Monk and Szabo [122], who present results using higher order hexahedral edge elements for a rectangular cavity problem. In this case, a penalty term is used to enforce the divergence–free condition. They obtain results which clearly demonstrate the advantages of using higher order approximations for computing eigenvalues when the corresponding eigenfunction is known to be smooth.

Subsequently, however, it has become apparent that the divergence condition is not explicitly required and, instead, one should simply consider the non–frequencies ($\omega^2 \in \mathbb{R} \setminus \{0\}$). Such a variational statement is: find $\boldsymbol{E} \in \boldsymbol{H}_0(\mathrm{curl})$ and $\omega^2 \in \mathbb{R} \setminus \{0\}$ such that

$$(\mu^{-1}\operatorname{curl} \boldsymbol{E}, \operatorname{curl} \boldsymbol{W})_\Omega - \omega^2(\epsilon \boldsymbol{E}, \boldsymbol{W})_\Omega = 0 \qquad \forall \boldsymbol{W} \in \boldsymbol{H}_0(\mathrm{curl}) \tag{139}$$

and this is the starting point for the two–dimensional examples presented here. The three–dimensional example that we shall present uses an alternative argument, where a Lagrange multiplier is used to enforce the zero divergence condition, and in this case the variational statement presented in equations (136) and (137) is used.

In particular, we use a quadrilateral discretisation for the two–dimensional problems and a tetrahedral discretisation for the three–dimension problems. An alternative variational statement is used for the three–dimensional problems because of the existence of zero on the diagonals of the stiffness matrix resulting from the discretisation of the curl − curl term with the tetrahedral elements. For the quadrilateral elements, no zero entries appear on the diagonal and hence the simpler variational statement can be applied.

In both cases, the discrete solutions obtained should posses the following properties, if the resultant schemes are to be regarded as being convergent:

1. *Approximation Capability (Consistency):* the error in the approximate discrete solutions $\boldsymbol{E}_H$ and p_H must tend to zero in the appropriate norms, as the mesh spacing decreases $h \to 0$ and the order of approximation increases $p \to \infty$.

2. *Babuska–Brezzi Condition:* the gradients of the test functions for the Lagrange multiplier space should be contained in the discrete subspace of $\boldsymbol{H}_0(\text{curl})$, i.e. $\nabla q_H \in X_0^H$ [119].

3. *Discrete Compactness Property:* this implies that exactly m discrete eigenvalues should converge to the squared resonant frequencies ω^2 if ω^2 is of multiplicity m.

We note that many recent developments have emerged on the proof of the discrete compactness property (see [50, 28, 26, 27] and the references therein). However, a proof of this theorem for general *hp*–approximations does not appear to be currently available for the three–dimensional case. We shall not dwell on these conditions, as our aim is to provide numerical evidence which supports the claim that the approach described here leads to a convergent scheme.

A convenient set of two– and three–dimensional benchmark examples has been proposed by Dauge [46]. We use a selection of these examples to provide numerical evidence of the effectiveness of the *hp* approach. In fact, if a proof of discrete compactness was known for *hp*–version finite elements, then this together with the work of Ainsworth and Pinchedez [12] would suggest that the convergence of the eigenvalues would be exponential with respect to the number of degrees of freedom N for the correct combination of h– and p–refinements as

$$\frac{|\omega^2 - \lambda|}{\omega^2} \propto C \exp(-\beta N^{\alpha}) \tag{140}$$

where α depends on the dimension of the problem and the types of singularities present. It is evidence of these exponential rates of convergence that we wish to demonstrate in the following sections.

7.1 Numerical Examples in 2D

As a first illustration of the success of the *hp* approach for solving this problem, we consider the computation of the eigenvalues for the $(-1,-1) \times (1,1)$ L shape domain with PEC boundaries. A sequence of 4 geometric meshes are constructed with refinement towards the reentrant corner. Meshes of this form are known to localise the effects of the singularity which occurs at the corner. For the generation of these meshes, a grading factor of 0.25 was used and the meshes are shown in Figure 30. On each mesh, the polynomial order was uniformly increased from $p = 0$ to $p = 5$ in increments of 1. For each discretisation, the first

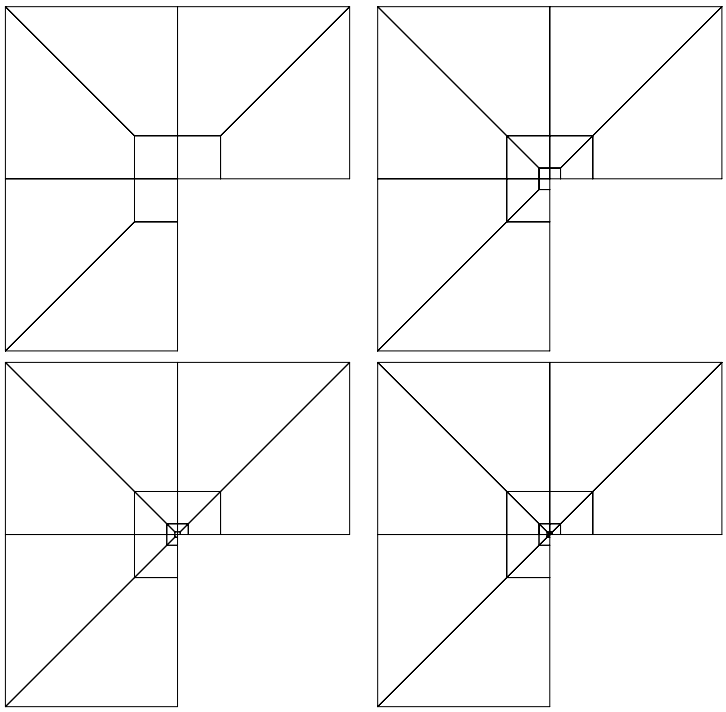

Figure 30. Eigenvalue calculations on the $(-1,-1)\times(1,1)$ L-shape domain, showing, a sequence of four graded meshes

three eigenvalues were computed and the errors in the computed eigenvalues determined using the available benchmark values

$$\omega_1^2 = 1.47562182408 \qquad \omega_2^2 = 3.53403136678 \qquad \omega_3^2 = 9.86960440109$$

correct to the number of figures quoted. The results obtained are shown in Figure 31. In each case, we observe that a family of convergence curves is obtained for each eigenvalue. The convergence behaviour on each mesh, with increasing p, shows a similar behaviour. Notably, in the case of the third eigenvalue, we observe that the family of convergence curves cross each other, indicating that in this case performing p–refinement alone is not the best refinement strategy. To determine if exponential convergence has in fact been obtained for the eigenvalues, we plot the error envelope for the eigenvalues, against the number of degrees of freedom raised to the power of one third, in Figure 32. The error envelope for the first two eigenvalues consists of p–refinement on mesh 1, while the error envelope for the third eigenvalue consists of a combination of h– and p–refinements. After a short pre–asymtopic region, we observe that in all cases, the curves are approximately straight line plots indicating that exponential convergence of the eigenvalues is being obtained.

As a second example, we consider the transmission type problem of a $(-1,-1)\times(1,1)$ square, with a chequerboard type pattern of varying material coefficients and PEC boundaries. The configuration is described in Figure 33. For this problem, we construct a sequence of 4 meshes which are graded towards the midpoint of the domain, as it is known that this point is associated with singular eigenfunctions. The meshes are shown in Figure 34 and the grading factor in this case is 0.16. As in the previous example, the polynomial order of the elements is uniformly increased from $p = 0$ to $p = 5$ and the error in the first three

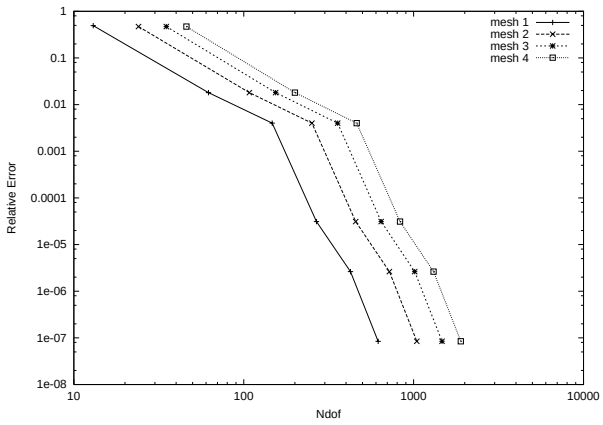

λ_1

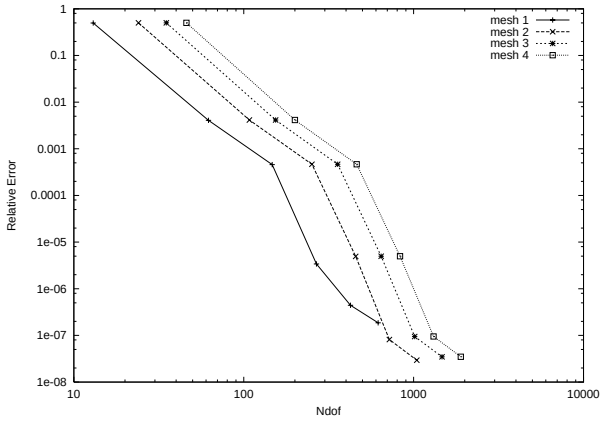

λ_2

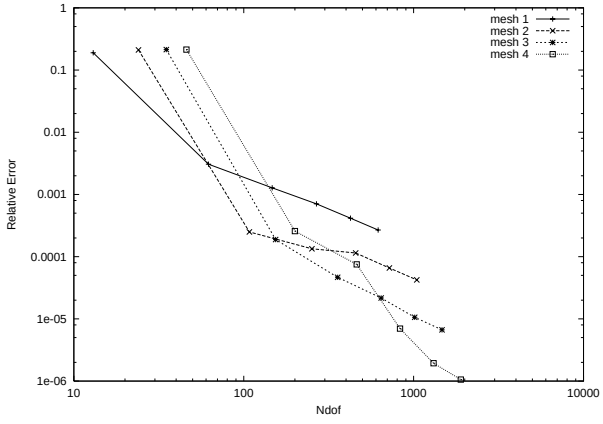

λ_3

Figure 31. Convergence of λ_1, λ_2 and λ_3 with increasing p-refinement on the sequence of 4 graded meshes for the PEC L shape problem

eigenvalues is determined, by using the benchmark values

$$\omega_1^2 = 3.317548763415 \qquad \omega_2^2 = 3.366324157260 \qquad \omega_3^2 = 6.186389562488$$

correct to the number of figures quoted. The results of the computations are presented in

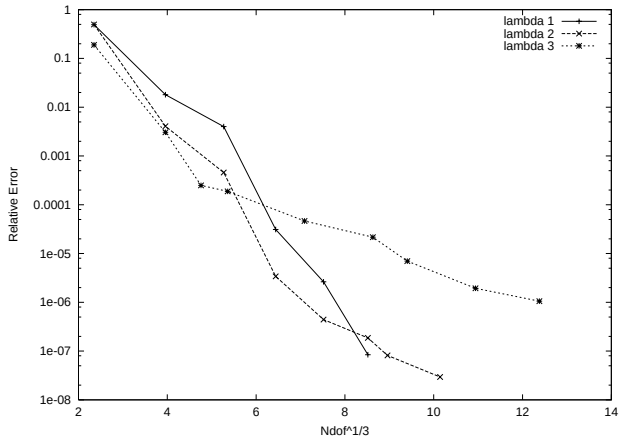

Figure 32. Convergence of the error envelopes for λ_1, λ_2 and λ_3 against $\text{Ndof}^{1/3}$ for the PEC L shape problem

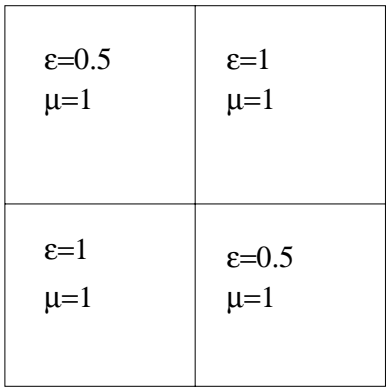

Figure 33. Chequer board pattern of varying material coefficient used in the transmission type problem

Figure 35. For each eigenvalue, we observe that a family of convergence curves is obtained, each of which exhibit a similar convergence behaviour. We note that the family of convergence curves cross each other for the second eigenfunction for this problem. To determine if exponential convergence has been obtained, we again plot the error envelope for each eigenvalue against the number of degrees of freedom raised to the power of one third in Figure 36. The error envelope for the first and third eigenvalues consists of p–refinements on the first mesh alone, while the error envelope for the second eigenvalue consists of combinations of h– and p–refinements. We observe that, after a short pre–asymptotic region, the curves are straight line plots indicating that exponential convergence is obtained.

From these examples, it is apparent that the *hp*–finite element technique is highly effective for computing the eigenvalues of Maxwell cavity problems and that the theoretically predicted exponential rates of convergence are also observed in practice. Further two–dimensional numerical examples, which consider cases where the boundaries of the domain are curved, can be found in [6].

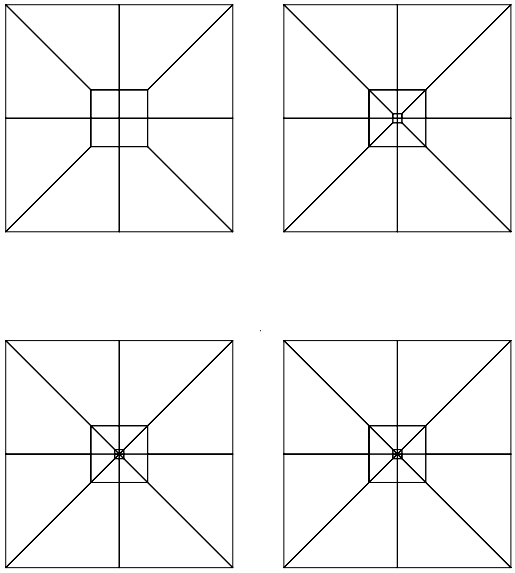

Figure 34. Eigenvalue calculations on a $(-1,-1)\times(1,1)$ square domain with regions of different material properties showing, a sequence of four graded meshes

7.2 Numerical Examples in 3D

The solution of 3D eigenvalue problems is, computationally, much more expensive than those in two–dimensions. However, using an *hp*–finite element approach still offers considerable advantages over an approach using only low order elements. These advantages include the possibility of exponential convergence of the eigenvalues and large reductions in the number of degrees of freedom required to solve a given problem. In this section, we shall present a numerical example which demonstrate these advantages.

The example considered is taken from [10]. In this work, a discretisation which has a uniform order of approximation throughout the domain is employed. This discretisation is used on a geometrically refined partition to compute the Maxwell eigenvalues for the L-shaped domain shown in Figure 37. The first four benchmark eigenvalues are given approximately by

$$\omega_1^2 = 9.63972384472 \qquad \omega_3^2 = 13.4036357679$$
$$\omega_2^2 = 11.3452262252 \qquad \omega_4^2 = 15.1972519265$$

correct to the number of figures quoted. To assess the accuracy of the procedure, calculations were undertaken on a sequence of different meshes with uniform polynomial order p. In all cases, a sequence of unstructured meshes with increasing h–refinement towards "Edge A", as identified in Figure 37, were used. The meshes were generated using a Delaunay mesh generation procedure [125] and the sequence of meshes employed is illustrated in Figure 38. Figure 39 shows the variation of the relative error of the first eigenvalue with the number of degrees of freedom (Ndof), when uniform orders of approximation are employed on each of the four meshes. The corresponding accuracy of the fourth eigenvalue is shown in Figure 40. In both cases, computations on the first mesh consist of uniform polynomial orders $p = 0,1,2,3,4,5$, computations on the second mesh consist of uniform polynomial orders $p = 0,1,2,3,4$ and computations on the third and fourth meshes consist of uniform polynomial orders $p = 0,1,2,3$. Higher polynomial orders were not undertaken on the denser meshes because of the high memory requirements of the Harwell library eigenvalue

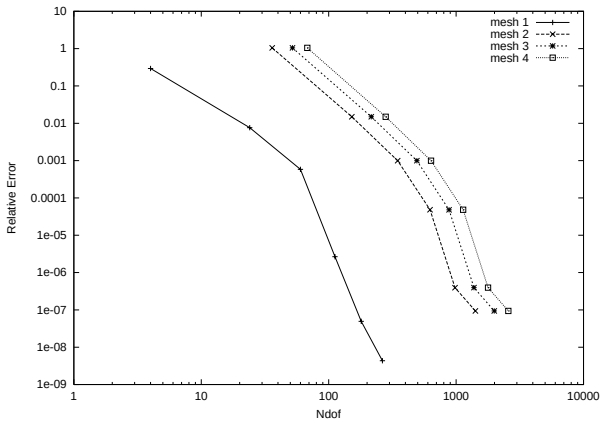

λ_1

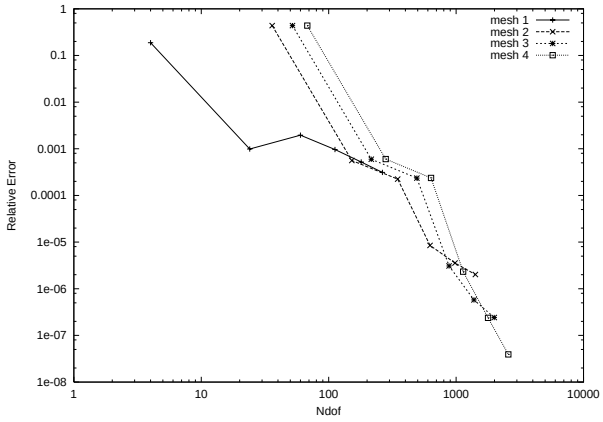

λ_2

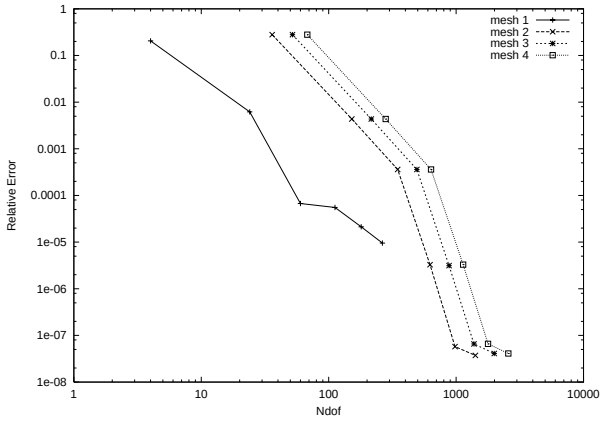

λ_3

Figure 35. Convergence of λ_1, λ_2 and λ_3 with increasing p-refinement on the sequence of 4 graded meshes for the transmission problem

solver that was used to produce the solution. To quantify the convergence behaviour, the logarithm of the relative error envelope against the number of degrees of freedom to the power of one fifth is plotted. The relative error envelope is obtained by determining

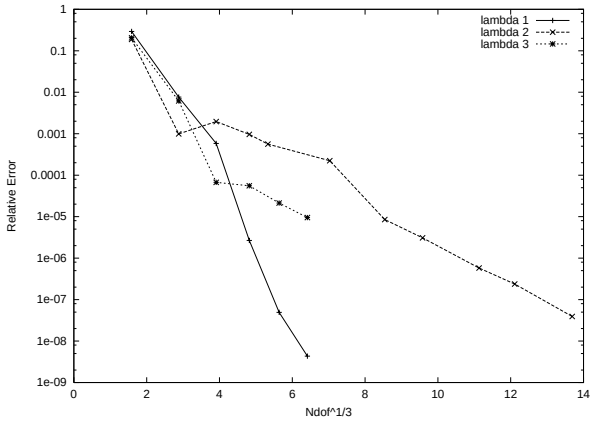

Figure 36. Convergence of the error envelopes for λ_1, λ_2 and λ_3 against $\text{Ndof}^{1/3}$ for the transmission problem

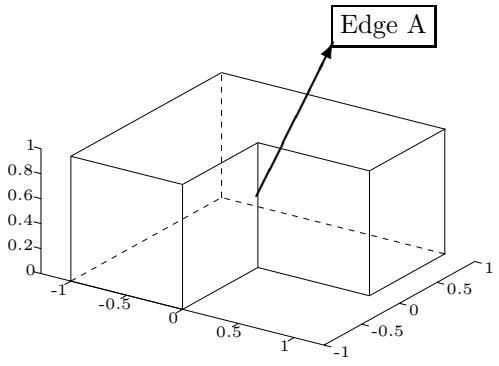

Figure 37. The thick L-shape domain used in the computations of the Maxwell eigenvalues

the lowest relative error computed for a given number of degrees of freedom. In this way, the relative error envelope may consist of both h– and p–refinements. The power of one fifth follows from theoretical results for the H^1 conforming approximations in three dimensions [18]. For the Maxwell eigenvalues it was conjectured that the convergence will also be exponential with rate $\exp\{-c(\text{Ndof})^{1/5}\}$, where c is a constant. In this case, a straight line plot indicates exponential convergence. Figure 41 shows the variation of the relative error envelope with $(\text{Ndof})^{1/5}$ for the first and fourth eigenvalues. In the case of the first eigenvalue, the relative error envelope involves both h– and p–refinements. For the fourth eigenvalue, the relative error envelope contains only p–refinement. We observe that the curve for the first eigenvalue is a straight line, apart from the initial step, indicating that exponential convergence has been obtained. The curve for the fourth eigenvalue is also a straight line indicating that exponential convergence has again been obtained. We note that the gradient of the curve for the fourth eigenvalue is steeper than that obtained for the first eigenvalue, indicating that the value of c is larger for the fourth eigenvalue.

Further numerical examples which demonstrate the existence of exponential convergence for both straight and curved sided domains in three–dimensions can be found in [44].

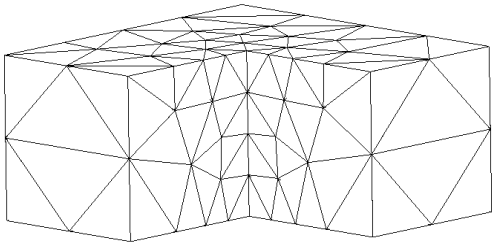

251 elements

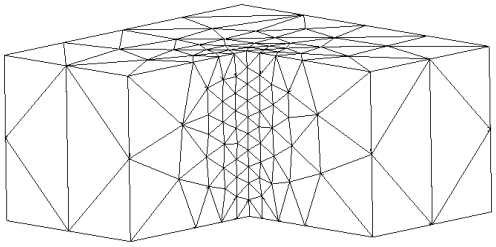

686 elements

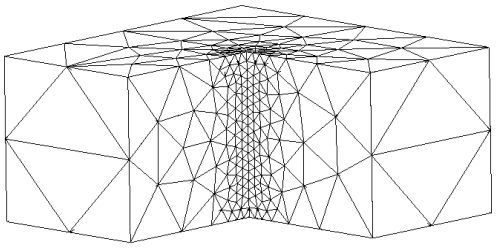

1365 elements

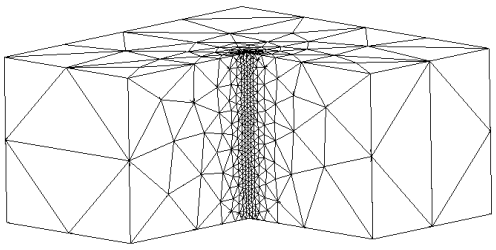

2075 elements

Figure 38. The sequence of meshes employed for determining the Maxwell eigenvalues of the thick L–shaped domain

7.3 Extension to Axisymmetric Problems

For a certain class of three–dimensional problems, one can exploit the rotationally symmetric nature of the geometry and use a Fourier decomposition of the field to simplify

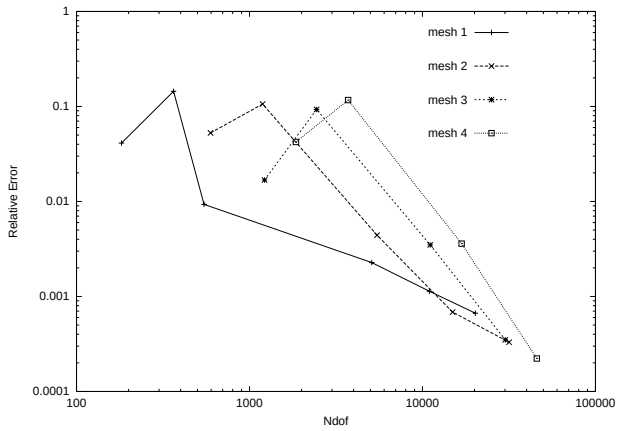

Figure 39. Convergence of λ_1 with increasing uniform polynomial order p on the sequence meshes $1-4$

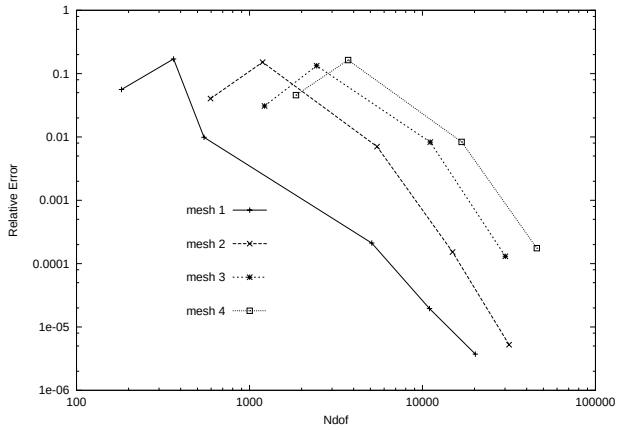

Figure 40. Convergence of λ_4 with increasing uniform polynomial order p on the sequence meshes $1-4$

the problem [75]. This enables the dimension of the problem to be reduced from three to two. The new computational domain for this problem is shown in Figure 42. For these two–dimensional problems, three components of the electric field (E_r, E_θ, E_z) in cylindrical coordinates should be computed and hence a special discretisation consisting of both $\boldsymbol{H}^{(2)}(\text{curl})$ and H^1 conforming elements is required. Difficulties arise in providing appropriate boundary conditions on the rotational axis of symmetry Γ_0. However, a novel non–conforming approach which omits the rotational axis from the computational domain allows the straightforward use of *hp* quadrilateral and triangular basis functions for this problem has already been presented [67]. In this work numerical examples have also been given.

8 NON-CONFORMING APPROACHES

$\boldsymbol{H}(\text{curl})$ conforming approaches are not the only type of finite element approximations that can be applied to solve Maxwell's equations. A certain amount of attention has also

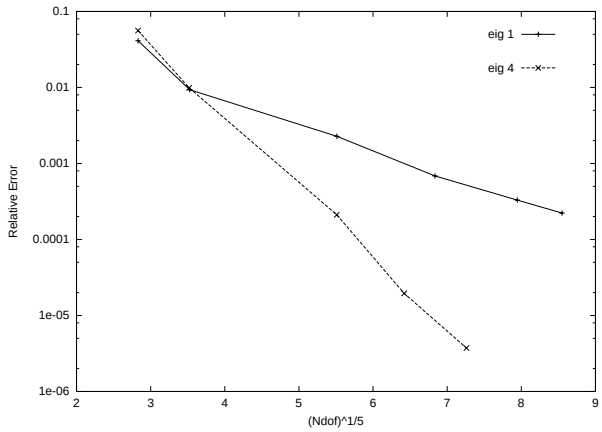

Figure 41. The relative error envelopes for λ_1 and λ_4 plotted with $(\text{Ndof})^{1/5}$

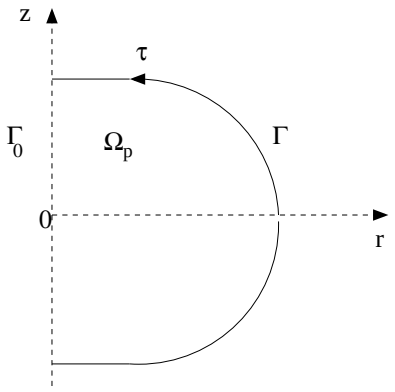

Figure 42. The domain Ω_p with boundary $\partial\Omega_p = \Gamma \cup \Gamma_0$ and tangent vector $\boldsymbol{\tau}$ which is obtained when a cylindrical coordinate system is adopted

been given to so called non–conforming approaches, in which the finite element basis does not conform to solution space of the problem. Accurate solutions can still be obtained, provided that suitable modifications to the boundary conditions are made and the effects of singularities are correctly handled. Typically non–conforming approaches are described with a particular electromagnetic application in mind and we consider here a selection of recent developments.

Lynch and Paulsen [87, 86] describe a non–conforming approach that is based on nodal elements and the addition of a penalty term for the solution of the vector wave equation in the frequency domain. They apply their approach to the solution of a problem consisting of two cylinders with dissimilar material driven by a uniform field applied at the boundary. For this test case, they show that their approach does not produce spurious modes. However, it remains unclear as to what happens when the approach is applied to problems with sharp corners, where strong singularities can occur. In a sequence of papers, Morgan and Hassan *et al.* [98, 99, 97] discuss an approach using the lowest order nodal H^1 conforming elements for the solution of electromagnetic scattering problems. In two dimensions, they formulate

the problem in the conservation form

$$\frac{\partial \boldsymbol{U}}{\partial t} + \frac{\partial \boldsymbol{F}_j}{\partial x_j} = \boldsymbol{0} \qquad j = 1, 2 \tag{141}$$

where the summation convention has been employed,

$$\boldsymbol{U} = \begin{pmatrix} \epsilon \boldsymbol{E} \\ \mu \boldsymbol{H} \end{pmatrix} \tag{142}$$

and the flux vectors are defined according to

$$\boldsymbol{F}_1 = \begin{pmatrix} 0 \\ H_z \\ -H_y \\ 0 - E_z \\ E_y \end{pmatrix} \qquad \boldsymbol{F}_2 = \begin{pmatrix} -H_z \\ 0 \\ H_x \\ E_z \\ 0 \\ -E_x \end{pmatrix} \tag{143}$$

By writing the time dependent Maxwell equations in this way they are able to apply many algorithms previously designed for computational fluid dynamics to the electromagnetics problem. Scatterers with sharp corners are handled effectively through the use of characteristic boundary conditions. In [96] a parallel version of their algorithm is proposed.

Recently, there has been substantial interest in the application of the discontinuous Galerkin method to problems in electromagnetics. This method represents a variant of the standard finite element scheme as only local element size systems are required to be inverted. Warburton and Hesthaven [62, 63, 123] propose a method of this type which involves high order H^1 conforming basis functions for the solution of large scale electromagnetic scattering problems in two and three–dimensions. In more recent work, Hesthaven and Warburton [61] have extended the approach to the solution of eigenvalue problems. Special modifications allow the successful computation of two and three dimensional eigenvalue problems, although there remains a trade–off between suppressing spurious modes and conditioning. Frequency domain discontinuous Galerkin methods have also been developed for Maxwell's equations. These essentially fall into two categories: local discontinuous Galerkin methods and interior penalty methods. Of particular interest is the application of the interior penalty methods to the high frequency case of the time harmonic Maxwell equations [69].

Costabel and Dauge [42] proposed the weighted regularisation approach for the solution of Maxwell equations. This involves using a p-version H^1 conforming basis and using special weights in regions of the domain associated with singularities, such as edges and corners. The weight used differs according to the type of singularity. Accurate simulations for straight sided eigenvalue problems and later curved sided eigenvalue problems [43] were obtained. Recently this approach has been employed for some large scale three–dimensional eigenvalue problems and the results of these experiments are described by Frauenfelder [55].

9 AREAS OF FURTHER RESEARCH

The area of computational electromagnetics includes many different applications and not just the scattering and eigenvalue computations that have been reported on here. The application of the these to other areas, such as eddy current problems, EMC problems or lightning strike can now be attempted. Another challenging area for research is the development of methods for the solution of the linear equation system which arises in

the scattering simulations. For two–dimensional problems, the indefinite linear system for frequency domain algorithms can be easily solved using a direct solver, such as the one found in LAPACK. But, there is no efficient method for the corresponding three dimensional scattering computations and this is a shortcoming that must be addressed. Experiments with a BICGSTAB algorithm with hierarchical $\boldsymbol{H}(\mathrm{curl})$ conforming tetrahedral elements in [80] yielded unsatisfactory results. Multigrid algorithms have been developed for the lowest order $\boldsymbol{H}(\mathrm{curl})$ conforming elements but for the non–indefinite case [65, 17, 59]. Work on the development of preconditioners based on domain decomposition is also promising, see [117] and references therein. However, this again is limited to the non–indefinite case. The provision of an efficient solver for the indefinite case still requires research.

The selection of a suitable efficient eigenvalue solver for *hp*–approximation has not been addressed in the literature. For low order approximations, different eigenvalue solution algorithms have been compared in the literature [2, 16]. We reported on *hp* adaptivity for scattering problems in two dimensions, but for three dimensional problems considerable research remains to be undertaken. Indeed, this is also true for the eigenvalue problems. Although we have seen that with the correct selection of h– and p–refinements, the theoretical predicted exponential rates of convergence can indeed be obtained, it remains to derive a suitable error estimator to automatically adapt the discretisation.

Moreover in this work, we have restricted ourselves chiefly to frequency domain computations. Of course, time domain computations are also an important area of research in computational electromagnetism. The application of the *hp*–version $\boldsymbol{H}(\mathrm{curl})$ conforming finite element methods to time domain computational electromagnetics remains in its infancy and only some simple two–dimensional scattering examples have been presented [80].

ACKNOWLEDGEMENTS

The authors would also like to thank Professor M. Ainsworth, Dr. J. Coyle, Professor O. Hassan, Professor Hiptmair, Professor J. Peraire and Professor N.P. Weatherill for their contribution to the work presented in this paper. The authors wish to thank EPSRC for the financial support that was received through the grants GR/M59112 and GR/R53005, which partly supported this work.

REFERENCES

1 I.A. Abramowitz and M. Stegun (1964). *Handbook of Mathematical Functions with Formulas, Graph and Mathematical Tables*. National Bureau of Standards, Washington D.C. .

2 S. Adam, P. Arbenz and R. Geus (1997). Eigenvalue solvers for electromagnetic fields in cavities. *Technical Report*, Institute of Scientific Computing ETH Zürich.

3 M. Ainsworth (2004). Discrete dispersion relation for hp-version finite element approximation at high wave number. *SIAM Journal on Numerical Analysis*, **42** (**2**), 553–575.

4 M. Ainsworth (2004). Dispersive and dissipative behaviour of high order discontinuous Galerkin finite element methods. *Journal of Computational Physics*, **198** (**1**), 106–130.

5 M. Ainsworth (2004). Dispersive properties of high order Nédélec/edge element approximation of the time-harmonic Maxwell equations. *Philosphical Transactions of the Royal Society Series A*, **362**, 471–493.

6 M. Ainsworth and J. Coyle (2003). Computation of Maxwell eigenvalues on curvilinear domains using *hp* Nédélec elements. *Numerical Mathematics and Advanced Applications*, Springer-Verlag.

7 M. Ainsworth and J. Coyle (2001). Hierarchic *hp*-edge element families for Maxwell's equations on hybrid quadrilaterial/triangular meshes. *Computer Methods in Applied Mechanics and Engineering*, **190**, 6709–6733.

8 M. Ainsworth and J. Coyle (2003). Conditioning of hierarchic *p*–version Nédélec elements on meshes of curvilinear quadrilaterals and hexahedra. *SIAM Journal on Numerical Analysis*, **41**, 731–750.

9 M. Ainsworth and J. Coyle (2003). Hierarchic finite element bases on unstructured tetrahedral meshes. *International Journal for Numerical Methods in Engineering*, **58**, 2103–2130.

10 M. Ainsworth, J. Coyle, P.D. Ledger and K. Morgan (2003). Computation of Maxwell eigenvalues using higher order edge elements in three–dimensions. *IEEE Transactions on Magnetics*, 2149–2153.

11 M. Ainsworth and J.T. Oden (2000). *A Posteriori Error Estimation in Finite Element Analysis*. John Wiley & Sons.

12 M. Ainsworth and K. Pinchedez (2003). *hp*–Approximation theory for BDRM/RT finite elements and applications. *SIAM Journal on Numerical Analysis*, **40**, 2047–2068.

13 M. Ainsworth and B. Senior (1997). Aspects of an adaptive *hp*–finite element method: Adaptive strategy, conforming approximation and efficient solvers. *Computer Methods in Applied Mechanics and Engineeing*, **150**, 65–87.

14 L.S. Anderson and J.L Volakis (1997). A novel class of hierarchical higher order tangential vector finite elements for electromagnetics. In *Proceedings of IEEE Antennas and Propagation Society International Symposuim*, 648–651.

15 L.S. Anderson and J.L Volakis (1998). Hierarchical tangential vector finite elements for tetrahedra. *IEEE Microwave and Guided Wave Letters*, **8**, 127–129.

16 P. Arbenz and R. Geus (1999). A comparison of solvers for large eigenvalue problems occuring in the design of resonant cavities. *Numerical Linear Algebra with Applications*, **6**, 3–16.

17 D.N. Arnold, R.S. Falk and R. Winther (2000). Multigrid in $\boldsymbol{H}(\mathrm{div})$ and $\boldsymbol{H}(\mathrm{curl})$. *Numerische Mathematik*, **85**, 197–217.

18 I. Babuska and B.Q. Guo (1996). Approximation properties of the *h-p* version of the finite element method. *Computer Methods in Applied Mechanics and Engineering*, **133**, 319–346.

19 I.M. Babuska, F. Ihlenburg, E.T. Paik and S.A. Sauter (1995). A generalised finite element method for solving the Helmholtz equation in two dimensions with minimal pollution. *Computer Methods in Applied Mechanics and Engineering*, **128**, 325–359.

20 I.M. Babuska and S.A. Sauter (2000). Is the pollution effect of the FEM avoidable for the Helmholtz equation considering high wave numbers? *SIAM Review*, **42**, 451–484.

21 M.L. Barton and Z.J. Cendes (1987). New vector finite elements for three–dimensional magnetic field computation. *Journal of Applied Physics*, **61**, 3919–3921.

22 A. Bayliss and E. Turkel (1980). Radiation boundary conditions for wave–like equations. *Communications in Pure and Applied Mathematics*, **33**, 707–725.

23 J-P Berenger (1994). A perfectly matched layer for the absorption of electromagnetic waves. *Journal of Computational Physics*, **114**, 185–200.

24 P. Bettess (1992). *Infinite Elements*. Penshaw Press, Sunderland.

25 P. Bettess, J. Shirron, O. Laghrouche, B. Perseux, R. Sugimoto and J. Trevelyan (2003). A numerical integration scheme for special finite elements for the Helmhotz equation. *International Journal for Numerical Methods in Engineering*, **56** (**4**), 531–552.

26 D. Boffi (2001). A note on the discrete compactness property and the De Rahm complex. *Applied Mathematics. Letters*, **14**, 33–38.

27 D. Boffi, L. Demkowicz and M. Costabel (2003). Discrete compactness for p and hp 2D edge finite elements. *Mathematical Models and Methods in Applied Sciences*, **13**, 1673–1687.

28 D. Boffi, P. Fernandes, L. Gastaldi and I. Perugia (1999). Computational models of electromagnetic resonators: analysis of edge element approximation. *SIAM Journal of Numerical Analysis*, **36**, 1264–1290.

29 A. Bossavit (1988). A rationale for edge elements in 3-D field computations. *IEEE Transactions on Magnetics*, **24**, 74–79.

30 A. Bossavit (1988). Whitney forms: a class of finite elements for three-dimensional computations in electromagnetism. *IEE Proceedings on Science, Measurement and Technology*, **135**, 493–500.

31 A. Bossavit (1998). *Computational Electromagnetisim, Variational Formulations Complementary, Edge Elements*. Academic Press.

32 A. Bossavit (1990). Solving Maxwell equations in a closed cavity and the question of spurious modes. *IEEE Transactions on Magnetics*, **26**, 702–705.

33 A. Bossavit and I. Mayergoyz (1989). Edge elements for scattering problems. *IEEE Transactions on Magnetics*, **25**, 2817–2821.

34 A. Bossavit and J-C. Vérité (1982). A mixed FEM-BEM method to solve 3-D eddy current problems. *IEEE Transactions on Magnetics*, **18**, 431–435.

35 A. Bossavit and J-C. Vérité (1983). The "TRIFOU" code: solving the 3D eddy current problem using H as a state vairable. *IEEE Transactions on Magnetics*, **19**, 2465–2470.

36 S. Caorsi, P. Fernandes and M. Raffetto (1997). Do covariant projection elements really satisify the inclusion condition? *IEEE Transactions on Microwave Theory and Techniques*, **45**, 1643–1644.

37 W. Cecot, L. Demkowicz, and W. Rachowicz (2000). A two dimensional infinite element for Maxwell's equations. *Computer Methods in Applied Mechanics and Engineering*, **188**, 625–643.

38 Z.J. Cendes (1991). Vector finite elements for electromagnetic field computation. *IEEE Transactions on Magnetics*, **27**, 3953–3966.

39 A. Chaterjee, J.M. Jin and J.L. Volakis (1992). Computation of cavity resonances using edge–based finite elements. *IEEE Transactions on Microwave Theory and Techniques*, **40**, 2106–2108.

40 G. Cohen and P. Monk (1998). Gauss point mass lumping schemes for Maxwell's equations. *Numerical Methods in Partial Differential Equations*, **14**, 63–68.

41 G.C. Cohen (2002). *Higher Order Numerical Methods for Transient Wave Equations*. Springer.

42 M. Costabel and M. Dauge (2002). Weighted regularization of Maxwell equations in polyhedra domains. *Numerische Mathematik*, **93**, 239–278.

43 M. Costabel, D. Martin and G. Vial (2001). Weighted regularization of Maxwell equations-computations in curvilinear polygons. *Numerical Mathematics and Advanced Applications - ENUMATH 2001*, In F. Brezzi, A. Buffa, S. Corsaro and A. Murli (Eds.), 273–280.

44 J. Coyle and P.D. Ledger (2005). Evidence of exponential convergence in the computation of Maxwell eigenvalues. *Computer Methods in Applied Mechanics and Engineering*, **194**, 587–604.

45 C.W. Crowley, P.P. Silvester and H. Hurwitz (1988). Covariant projection elements for 3D vector field problems. *IEEE Transactions on Magnetics*, **24**, 397–400.

46 M. Dauge. http://perso.univ-rennes1.fr/monique.dauge/benchmax.html.

47 L. Demkowciz and W. Rachowicz (2000). A 2D *hp*–adaptive finite element package for electromagnetics. *Computer Methods in Applied Mechanics and Engineering*, **187**, 307–337.

48 L. Demkowicz (1998). A posteriori error analysis for steady state Maxwell's equations. In *New Advances in Adaptive Computational Methods in Mechanics*, P. Ladaveze and J.T. Oden (Eds.), Elsevier.

49 L. Demkowicz (2003). *hp* Adaptive Finite Elements for Time Harmonic Maxwell's equations. In *Topics in Computational Wave Propagation, Lecture Notes in Computational Science and Engineering*, 163–199, Springer-Verlag.

50 L. Demkowicz, P. Monk, Ch. Schwab and L. Vardapetyan (2000). Maxwell eigenvalues and discrete compactness in two dimensions. *Computers & Mathematics with Applications*, **40**, 589–605.

51 L. Demkowicz, P. Monk, L. Vardapetyan and W. Rachowicz (2000). De Rham diagram for *hp* finite element spaces. *Computers & Mathematics with Applications*, *39*, 29–38.

52 L. Demkowicz and J.T. Oden (1994). Recent progress on application of *hp* adaptive BE/FE methods to elastic scattering. *International Journal for Numerical Methods in Engineering*, **37**, 2893–2910.

53 L. Demkowicz and L. Vardapetyan (1998). Modeling of electromagnetic absorption/scattering problems using *hp* adaptive finite elements. *Computer Methods in Applied Mechanics and Engineering*, **152**, 103–124.

54 A. Deraemaeker, I. Babuska and P. Bouillard (1999). Dispersion and pollution of the FEM solution for the Helmholtz equation in one, two and three dimensions. *International Journal for Numerical Methods in Engineering*, **46**, 471–499.

55 P. Frauenfeler (2004). *Design and Implementation of hp-FEM for Deterministic and Stochastic PDEs*. PhD thesis, Seminar for Applied Mathematics, ETH Zürich Switzerland.

56 D. Givoli (1992). *Numerical Methods for Problems in Infinite Domains*, Studies in Applied Mechanics, Vol. 33, Elsevier Scientific Publishing, Amsterdam.

57 V. Gradinaru and R. Hiptmair (1999). Whitney elements on pyramids. *Electronic Transactions on Numerical Analysis*, **8**, 154–168.

58 R.D. Graglia, D.W. Wilton and A.F. Peterson (1997). Higher order interpolary vector bases for computational electromagnetics. *IEEE Transactions on Antennas and Propagation*, **45**.

59 G. Haase, M. Kuhn and U. Langer (2001). Parallel multigrid 3D Maxwell solvers. *Parallel Computing*, **27**, 761–775.

60 M. Hano (1984). Finite element analysis of dielectric loaded waveguides. *IEEE Transactions on Microwave Theory and Techniques*, **32**, 1275–1279.

61 J.S. Hesthaven and T. Warburton (2003). High order nodal discontinous Galerkin methods for the Maxwell eigenvalue problem. *Technical Report 2003-11*, Scientific Computing Report Series, Department of Applied Mathematics, Brown Univeristy.

62 S. Hesthaven and T. Warburton (2001). High-order/spectral methods on unstructured grids. 1. time-domain solution of Maxwell's equations. *Journal of Computational Physics*, **181**, 186–221.

63 S. Hesthaven and T. Warburton (2004). High-order accurate methods for time-domain electromagnetics. *Computer Modelling in Engineering and the Science*, **5**, 395–408.

64 R. Hiptmair (2003). Coupling of finite elements and boundary elements in electromagnetic scattering. *SIAM Journal of Nuermical Analysis*, **41**, 919–944.

65 R. Hiptmair (1998). Multigrid method for Maxwell's equations. *SIAM Journal of Numerical Analysis*, **36**, 204–225.

66 R. Hiptmair (2002). Finite Elements in Computational Electromagnetisim. *Acta-Numerica*, **11**, 237–339.

67 R. Hiptmair and P.D. Ledger (2005). Computation of resonant modes for axisymmetric Maxwell cavities using *hp*–version edge finite elements. *International Journal for Numerical Methods in Engineering*, **62**, 1652–1676.

68 R. Hiptmair and P.D. Ledger (2003). A quadrilaterial edge element with minimum dispersion. *Technical Report 17*, Semainr for Applied Mathematics ETH Zürich.

69 P. Houston, I. Perugia, A. Schneebeli and D. Schotzau (2004). Interior penalty method for the indefinite time-harmonic Maxwell equations. *Technical Report 2004/01*, Technical Report Mathematics and Computer Science University of Leicester.

70 J. Jin (1993). *The Finite Element Method in Electromagnetics*. John Wiley and Sons.

71 A. Kameari (1990). Transient 3D eddy current using edge elements. *IEEE Transactions on Magnetics*, **26**, 446–468.

72 A. Kameari (1999). Symmetric second order edge elements for triangles and tetrahedra. *IEEE Transactions on Magnetics*, **35**, 1394–1397.

73 G.E.M. Karniadakis and S.J. Sherwin (1999). *Spectral hp–Element Methods for CFD*. Oxford University Press.

74 F. Kikuchi (1987). Mixed and penalty formulations for finite element analysis of an eigenvalue problem in electromagnetisim. *Computer Methods in Applied Mechanics and Engineering*, **64**, 509–521.

75 P. Lacoste (2000). Solution of Maxwell equations in axisymmetric geometry by Fourier series decomposition and by use of a $\boldsymbol{H}(\mathrm{rot})$ conforming element. *Numerische Mathematik*, **84**, 577–609.

76 O. Laghrouche and P. Bettess (2000). Short wave modelling using special finite elements. *Journal of Computational Acoustics*, **8**, 189–210.

77 O. Laghrouche, P.Bettess and R.J. Astley (2002). Modelling of short wave diffraction problems using approximating system of plane waves. *International Journal for Numerical Methods in Engineering*, **54**, 1501–1533.

78 P.D. Ledger (2002). *An hp-Adaptive Finite Element Proceedure for Electromagnetic Scattering Problems*. PhD thesis, Department of Civil Engineering, University of Wales, Swansea.

79 P.D. Ledger, Morgan K, O. Hassan and N.P. Weatherill (2002). Arbitrary order edge elements for electromagnetic scattering simulations using hybrid meshes and a PML. *International Journal for Numerical Methods in Engineering*, **55**, 339–358.

80 P.D. Ledger, K. Morgan and O. Hassan (2005). Frequency and time domain electromagnetic scattering simulations employing higher order edge elements. *Computer Methods in Applied Mechanics and Engineering*, **194**, 105–125.

81 P.D. Ledger, K. Morgan, O. Hassan and N.P. Weatherill (2003). Plane wave $\boldsymbol{H}(\mathrm{curl})$ conforming finite elements for Maxwell's equations. *Computational Mechanics*, **31**, 272–383.

82 P.D. Ledger, K. Morgan, J. Peraire, O. Hassan and N.P. Weatherill (2003). The development of an *hp* adaptive finite element proceedure for electromagnetic scattering problems. *Finite Element in Analysis and Design*, **39**, 751–764.

83 P.D. Ledger, J. Peraire, K. Morgan, O. Hassan and N.P. Weatherill (2003). Efficient highly accurate *hp*-adaptive finite element computations of the scattering width output of Maxwell's equations. *International Journal for Numerical Methods in Fluids*, **43**, 953–978.

84 P.D. Ledger, J. Peraire, K. Morgan, O. Hassan and N.P. Weatherill (2004). Parameterised electromagnetic scattering solutions for a range of incident wave angles. *Computer Methods in Applied Mechanics and Engineering*, **193**, 3587–3605.

85 J-F. Lee, D-K. Sun and Z.J. Cendes (1991). Full-wave analysis of dielectric waveguides using tangential vector finite elements. *IEEE Transactions on Microwave Theory and Techniques*, **39**, 1262–1271.

86 D.R. Lynch and K.D. Paulsen (1991). Elimination of vector parasites in finite element solutions. *IEEE Transactions on Microwave Theory and Techniques*, **39**, 395–404.

87 D.R. Lynch and K.D. Paulsen (1991). Origin of vector parasites in numerical Maxwell solutions. *IEEE Transactions on Microwave Theory and Techniques*, **39**, 383–394.

88 Y. Maday, J. Peraire and A.T. Patera (1999). A general formulation for a–posteriori bounds for output functionals of partial differential equations: application to the eigenvalue problem. *Comptes Rendus des Seances de l' Academie des Sciences*, **328**, 823–828.

89 R. Miniowitz and J.P. Webb (1991). Covariant-projection quadrilaterial elements for the analysis of waveguides with sharp edges. *IEEE Transactions on Microwave Theory and Techniques*, **39**, 501–505.

90 P. Monk and K. Parrott (2001). Phase accuracy comparisons and improved far–field estimates for 3-D edge elements on tetrahedral meshes. *Journal of Computational Physics*, **170**, 614–641.

91 P. Monk (1995). The near to far field transformation. *COMPEL The International Journal for Computation and Mathematics in Electrical and Electronic Engineering*, **14**, 41–56.

92 P. Monk (2003). *Finite Element Methods for Maxwell's Equations*. Oxford Science Publications.

93 P. Monk and K. Parrott (1994). A dispersion analysis of finite element methods for Maxwell's equations. *SIAM Journal of Scientific Computing*, **15**, 916–937.

94 P. Monk, K. Parrott and P.J. Wesson (1993). A dispersion analysis of finite element methods on triangular grids for Maxwell's equations. In J.R. Whiteman (Ed.), *The Mathematics of Finite Elements and Applications*, 315–321.

95 P. Monk and E. Suli (1998). The adaptive computation of far field patterns by a posteriori error estimation of linear functionals. *SIAM Journal of Numerical Analysis*, **36**, 251–274.

96 K. Morgan, P.J. Brookes, O. Hassan and N.P. Weatherill (1998). Parallel processing for the simulation of problems involving scattering of electromagnetic waves. *Computer Methods in Applied Mechanics and Engineeing*, **152**, 157–174.

97 K. Morgan, O. Hassan, N.E. Pegg and N.P. Weatherill (2000). The simulation of electromganetic scattering in piecewise homogeneous media using unstructured grids. *Computational Mechanics*, **25**, 438–447.

98 K. Morgan, O. Hassan and J. Peraire (1994). An unsturctured grid algorithm for the solution of Maxwell's equations in the time domain. *International Journal for Numerical Methods in Fluids*, **19**, 849–863.

99 K. Morgan, O. Hassan and J. Peraire (1996). A time domain unstructured grid approach to the simulation of electromagnetic scattering in piecewise homogeneous media. *Computer Methods in Applied Mechanics and Engineering*, **134**, 17–36.

100 G. Mur and A.T. de Hoop (1985). A finite element method for computing three–dimensional electromagnetic fields in homogeneous media. *IEEE Transactions on Magnetics*, **21**, 2188–2191.

101 J.C. Nédélec (1980). Mixed finite elements in $\mathbb{R}^3$. *Numerische Mathematik*, **35**, 315–341.

102 J.C. Nédélec (1986). A new family of mixed finite elements in $\mathbb{R}^3$. *Numerische Mathematik*, **50**, 57–81.

103 M. Paraschivoiu, J. Peraire and A.T. Patera (1997). A–posteriori finite element bounds for linear functional outputs of elliptic partial differential equations. *Computer Methods in Applied Mechanics and Engineering*, **150**, 289–312.

104 J. Peraire and A.T. Patera (1998). Bounds for linear functional outputs of coercive partial differtial equations: local indicators and refinement. In *New Advances in Adaptive Computational Methods in Mechanics*, P. Ladeveze and J.T. Oden (Eds.), Elsevier.

105 J. Peraire and A.T. Patera (1999). Asymptotic a–posteriori finite elment bounds for the outputs of noncoercive problems: the Helmholtz and Burgers equations. *Computer Methods in Applied Mechanics and Engineering*, **171**, 77–86.

106 J. Peraire, M. Vahdati, K. Morgan and O.C.Zienkiewicz (1987). Adaptive re–meshing for compressible flow computations. *Journal of Computational Physics*, **72**, 449–366.

107 W. Rachowicz and L. Demkowicz (2002). A three–dimensional *hp*-adaptive finite element package for electromagnetics. *International Journal for Numerical Methods in Engineering*, **53**, 147–180.

108 W. Rachowicz and A. Zdunek (2005). An *hp*-adaptive finite element method for scattering problems in computational electromagnetics. *International Journal for Numerical Methods in Engineering*, **62**, 1226–1249.

109 A.J. Ruiz–Genoveés, L.E. Garcia-Castillo, M. Salazar-Palma and T.K. Sarkar (2001). Third–order Nédélec tetrahedral finite element. In *ECCOMAS Computational Fluid Dynamics Conference*, Swansea. Published electronically in the CD accompanying the conference.

110 M. Salazar-Palma, T.K. Sarkar, L.-E. Garcia-Castillo, T. Roy and Antonije Djordjevic (1998). *Iterative and Self Adaptive Finite Elements in Electromagnetic Modeling*. Artech House.

111 J. Sarrate, J. Peraire and A.T. Patera (1999). A–posteriori error bounds for nonlinear outputs of the Helmholtz equation. *International Journal for Numerical Methods in Fluids*, **31**, 17–36.

112 P.P. Silvester and R.L. Ferrari (1996). *Finite Elements for Electrical Engineers*. Cambridge University Press.

113 P. Solin, K. Segeth and I. Dolezel (2004). *Higher–Order Finite Element Methods*. Chapman and Hall.

114 J.A. Stratton (1941). *Electromagnetic Theory*. McGraw–Hill.

115 A. H. Stroud and D. Secrest (1966). *Gaussian Quadrature Formulas*. Prentice Hall, Englewood Cliffs.

116 B. Szabó and I. Babuska (1991). *Finite Element Analysis*. John Wiley and Sons, New York.

117 A. Toselli and X. Vasseur (2004). Dual–primal FETI alogorithms for edge element approximations: Two–dimensional h and p finite elements on shape regular meshes. *Technical Report 01*, Seminar for Applied Mathematics, ETH Zürich.

118 J.S. van Welij (1985). Calculation of eddy currents in terms of h on hexahedra. *IEEE Transactions on Magnetics*, **21**, 2239–2241.

119 L. Vardapetyan and L. Demkowicz (1999). *hp* adaptive finite elements in electromagnetics. *Computer Methods in Applied Mechanics and Engineering*, **169**, 331–344.

120 J.L. Volakis, A. Chatterjee and L.C. Kempel (1998). *Finite Element Method for Electromagnetics, Antennas, Microwave Circuits and Scattering Applications*. IEEE/OUP Series of Electromagnetic Wave Theory.

121 J.S. Wang and N. Ida (1993). Curvilinear and higher order edge finite elements in electromagnetic field computation. *IEEE Transactions on Magnetics*, **29**, 1491–1494.

122 Y. Wang, P. Monk and B. Szabo (1996). Computing cavity modes using the p version of the finite element method. *IEE Transactions on Magnetics*, **32**, 1934–1940.

123 T. Warburton (2000). Application of the discontinous Galerkin method to Maxwell's equations using unsturctured polymorphic *hp* finite elements. In B. Cockburn, G.E. Karniadakis and Chi-Wang Shu (Eds.), *Discontinuous Galerkin Methods: Theory, Computation and Applications*, 451–458, Springer.

124 G.S. Warren and W.R. Scott (1994). An investigation of the numerical dispersion in the vector finite element method using quadrilateral elements. *IEEE Transactions on Antennas and Propagation*, **42**, 1502–1508.

125 N.P. Weatherill and O. Hassan (1994). Efficient three–dimensional Delaunay triangulation with automatic point creation and imposed boundary conditions. *International Journal for Numerical Methods in Engineering*, **37**, 2005–2039.

126 J.P. Webb (1999). Hierarchical vector basis functions of arbitrary order for triangular and tetrahedral finite elements. *IEEE Transactions on Antennas and Propagation*, **47**, 1244–1253.

127 J.P. Webb and B. Forghani (1993). Heirachical scalar and vector tetrahedra. *IEEE Transactions on Magnetics*, **29**, 1495–1498.

128 H. Whitney (1957). *Geometric Integration Theory*. Princeton University Press.

129 O.C. Zienkiewicz (1977). *The Finite Element Method*. McGraw-Hill, New York, 3rd edition.

Please address your comments or questions on this paper to:
International Center for Numerical Methods in Engineering
Edificio C-1, Campus Norte UPC
Grand Capitán s/n
08034 Barcelona, Spain
Phone: 34-93-4016035; Fax: 34-93-4016517
E-mail: onate@cimne.upc.es